Optimizing and Applying Graphene as a Saturable Absorber For Generating Ultrashort Pulses

by

Jonah Maxwell Miller

A thesis submitted to the

faculty of the

University of Colorado in partial fulfillment

of the requirements for the award of

departmental honors in the

Department of Physics

2011

This thesis entitled:
Optimizing and Applying Graphene as a Saturable Absorber For Generating Ultrashort Pulses
written by Jonah Maxwell Miller
has been approved for the Department of Physics

Thomas Schibli

John Cumalat

Jeanne Clelland

Date

The final copy of this thesis has been examined by the signatories, and we find that both the content and the form meet acceptable presentation standards of scholarly work in the above mentioned discipline.

Miller, Jonah Maxwell (BA Physics)

Optimizing and Applying Graphene as a Saturable Absorber For Generating Ultrashort Pulses

Thesis directed by Professor Thomas Schibli

Over the last decade, a variety of exciting applications have been found for lasers that generate ultrashort pulses of light with durations of just a few femtoseconds, known as femtosecond lasers (fs-lasers) [1]. People now routinely measure optical frequencies [2, 3], atomic and molecular spectra, lengths, distances [4], and displacements [5] with fs-lasers, and new applications are constantly being discovered. Pulses of such short duration can be achieved from passively mode-locked lasers—that is, lasers in which the longitudinal electromagnetic waves in the laser cavity, or "modes," are locked into phase with each other [6, 7, 8, 9]. To lock the phase of the modes, a saturable absorber—a device which absorbs some percentage of low-intensity light, but which allows high-intensity light to pass through with reduced absorption—is used [6, 7, 8, 9].

To produce short pulse-width, high repetition-rate (many pulses per second) lasers, a saturable absorber that becomes opaque quickly after being "saturated" by light and that saturates very easily is needed [6]. In this work, the potential for single atomic-layer graphene—a honeycomb lattice of carbon atoms only one atom thick, which has already proven itself to be an extraordinary material [10, 11, 12, 13, 14, 15, 16, 17]—as a saturable absorber is explored, and a method for producing high-quality graphene saturable absorbers is developed. This high-quality graphene's nonlinear (saturable) absorption was probed optically by differential transmission and pump-probe measurements and the possibility of tuning graphene's optical properties by chemical doping is explored by Raman spectroscopy and compared to doping concentration and measurements made in differential transmission and spectrophotometry. It is concluded that while graphene could be a highly desirable saturable absorber, it is currently limited by its relatively high saturation fluence compared to its damage threshold. The possibility of a graphene-based high-speed electro-optic modulator is also briefly discussed. This work is a step in the development of graphene as a saturable absorber comparable to but substantially cheaper than semiconductor saturable absorber mirrors (SESAMs), and towards the development of graphene-based optical and electro-optical devices for lasers.

To Alexandra Fresch

Without your emotional support throughout my college career, or your presence as a role model, I might never have pursued an honors thesis.

Acknowledgements

I would like to thank the Principal Investigator, Professor Thomas Schibli, for his patience, guidance and support throughout this project.

I owe a great deal also to Professor Schibli's student, Chien-Chung Lee, with whom I have worked very closely. He has shared with me a great deal of his knowledge of optics, lasers, and semiconductor physics. He guided me through the construction of the differential transmission setup and helped me first learn my way around an optics lab, performed all of the pump-probe measurements on graphene, built the ultra-low pressure CVD furnace we use to grow our samples, doped the graphene I measured in Raman, measured its Fermi Level by spectrophotometer, and measured its nonlinear absorption by the differential transmission setup we built together.

I would also like to thank the other members of Professor Schibli's group, both past and present, for their support and for many helpful discussions, including: Brian Benton, David Miller, Wanyan Xie, Seiya Suzuki, Linna Cooley, and Jeffrey Hart.

I would also like to express profound gratitude towards Doctor Kaoru Minoshima, AIST/NMIJ Tsukuba, Japan, who provided the Schibli group with an Er:Yb:glass gain medium, and from the University of Colorado at Boulder: Professor Markus Raschke for lending me the use of his micro-Raman setup, Professor John Cumalat for the diamond sample, and Samuel Berweger and Doctor Joanna Atkin for lending me their expertise in Raman spectroscopy.

This research was supported in part by the NNIN at the Colorado Nanofabrication Laboratory, The National Science Foundation under Grant No. ECS-0335765, and the Innovative Seed Grant Program and the Undergraduate Research Opportunities Fund (UROP) at the University of Colorado at Boulder.

Finally, I would like to thank my parents and my grandparents, whose continued love, encouragement, support, and belief in my abilities have made it possible for me to go from a very mediocre student to an honors student, and who have always encouraged me to ask as many questions about the world as possible.

Thank you, everyone; this project would not have been possible without you.

Contents

Chapter

Figures

Figure

Chapter 1

Introduction

1.1 Motivation

1.1.1 Mode-Locked Lasers: Their Potential and Their Challenges

Lasers which produce ultrashort pulses of light, on the order of a few femtoseconds (1 fs = 10^{-15} s), have become an essential part of modern scientific research [1]. Optical frequencies [2, 3], atomic and molecular spectra, lengths, distances [4], and displacements [5] are nowadays routinely measured with femtosecond lasers, or fs-lasers. People now use fs-lasers as light sources to achieve in-vivo 3D imaging of the human retina, epidermis, and blood vessels [18]. Optical frequency combs produced by fs-lasers are used to help probe and manipulate the quantum state of gaseous atoms and molecules [19], and in all forms of condensed matter [20]. In astrophysics, fs lasers are used to calibrate spectrometers to unprecedented accuracy, allowing for measurements of the Doppler shifts of stellar objects with error approximately 1 cm/s [21, 22, 23]. In high-energy physics, ultrashort lasers might soon be commonly used for timing synchronization in large-scale accelerators [24] and will likely play an important role in generating ultra-bright, coherent X-ray pulses in free-electron laser facilities—which might bring several generations' worth of improvements to precision spectroscopy at very high energies.

As will be discussed below, femtosecond duration pulses are most often obtained from lasers passively mode-locked by saturable absorbers [6, 7, 8, 9]. The most common type of saturable absorber, called a Saturable Absorber Mirror (SESAM), offers a variety of design parameters to produce pulses of varying width (in the time domain) and pulse repetition-rate, but is grown on a crystalline substrate from which it

cannot be removed, limiting design flexibility. Furthermore, how narrow one can make a pulse is limited by the carrier relaxation time of the absorber. Worse, high repetition-rate lasers often slowly damage SESAMS and severely shorten their working lifetime [25]. These three factors limit the capabilities of SESAMs, hence the search for other absorbers. Although, as will be discussed throughout this work, graphene may be substantially less resilient than modern SESAMs, investigating it is a step in the search for new, higher-quality saturable absorbers.

Mode-locked lasers are also plagued by instabilities known as "Q-switching instabilities." Q-switching is another method of producing ultrafast high-energy pulses in a laser that uses saturable absorbers. As the name would imply, Q-switching is a process where the quality factor of the cavity (energy stored in the cavity divided by energy loss per round trip) rapidly switches between high values and low values. The result is that the cavity stores light and energy while the Q factor is high before rapidly dissipating it as a pulse of durations ranging from picoseconds to nanoseconds when the Q factor is low [6]. However, the pulses produced by Q-switching are much less stable or consistent and the output of the laser is often noisy. Furthermore, Q-switched lasers operate with pulse widths of a few picoseconds (ps)[6, 26]—too long for many applications. When a laser is mode-locked by a saturable absorber, it is possible for the laser to begin Q-switching as well, and this is usually undesirable [6]. As will be discussed much later, a possible application of graphene in mode-locked lasers is as a component in an active feedback loop to suppress Q-switching instabilities.

1.1.2 Graphene: The Wonder Material

Although graphene—single atomic-layer graphite—was first postulated in 1947 [27] and poor quality graphene was produced in 1962 [28], a method to produce high-quality graphene was only developed extremely recently by Konstantin Novoselov and Andre Geim [29], who won the Nobel Prize as a result [30]. Because graphene is essentially two-dimensional (it is impossible for a real condensed matter material to get any thinner than a single atomic layer), people considered it thermodynamically unstable and thus a mere theoretical construct until its discovery. However, since that discovery, graphene has displayed a stunning number of fascinating and useful properties.

It has been shown to display the quantum Hall effect at room temperature [14] and the fractional quantum Hall effect [15], a tremendously high electrical conductivity [11, 31], a universal linear optical absorption of 2.3% through all (low-energy) frequencies of light [32], and a breaking strength two hundred times stronger than steel [33]. It has already been used as a super-sensitive gas detector [13], an impermeable membrane [17], a transparent electrode for touch screens [11], as a replacement for silicon in high speed integrated electronics [12], and possibly as a critical component in many more applications. Most relevantly here, it has been demonstrated to be a saturable absorber [34, 35, 36, 37, 38, 39, 40, 41].

As a saturable absorber, graphene looks very appealing at first glance. At low intensities, it absorbs 2.3% of incident light, independent of frequency, and at very high intensities it only absorbs about 1% of incident light. Initially reported values for saturation fluence[1] (or intensity[2] depending on the model—this will be discussed in more detail later), were comparable to SESAMs. These factors ensure that it has a low enough loss to be feasibly used in a high-repetition-rate laser, and its high conductivity ensures a short optical response time [35, 31].

1.1.3 Graphene and Mode-Locked Lasers

The goal of this work is to explore the possibilities of applying graphene in fs-lasers—primarily as a more flexible and faster alternative to SESAMs that might overcome some of their limitations and secondarily as a component in an electro-optic modulator, which is a device for suppressing Q-switching instabilities through active feedback. Graphene is more flexible than SESAMs because a SESAM must have a crystaline substrate and faster because the interband relaxation time for electrons in the material is much shorter. Interband relaxation is described in chapter 2. At this time, a prototype electro-optic modulator has been constructed through the hard work of Chien-Chung Lee, Wanyan Xie, and Seiya Suzuki. The author was not a part of its development. However, the investigations of graphene's potential as a saturable absorber herein are related to its potential as a component in the modulator.

[1] Fluence is energy per unit area. Saturation fluence is thus the energy per area on an absorber when the absorption is e^{-1} its initial value.

[2] Intensity is power per unit area, where power is energy per unit time.

1.2 Overview

First, the necessary background information—the physics of mode-locking, saturable absorbers, and graphene—will be covered. Next, the characterization of pristine (unmodified except for transfer to an optically acceptable substrate) graphene as a saturable absorber by differential transmission and pump-probe techniques will be described. Then, using the experimental techniques developed in the previous section, the optimization of growth of graphene by chemical vapor deposition and subsequent wet transfer will be discussed. After covering pristine graphene, the tuning of graphene's linear absorption by chemical doping and its characterization by differential transmission, spectrophotometry, and Raman spectroscopy will be discussed, the author's major contribution being in Raman spectroscopy. Finally, this work will conclude with a summary of results and a brief discussion of the next steps: both those that have been taken and those still waiting for brave minds.

Chapter 2

General Background

2.1 The Mechanics of Mode-Locking in Brief

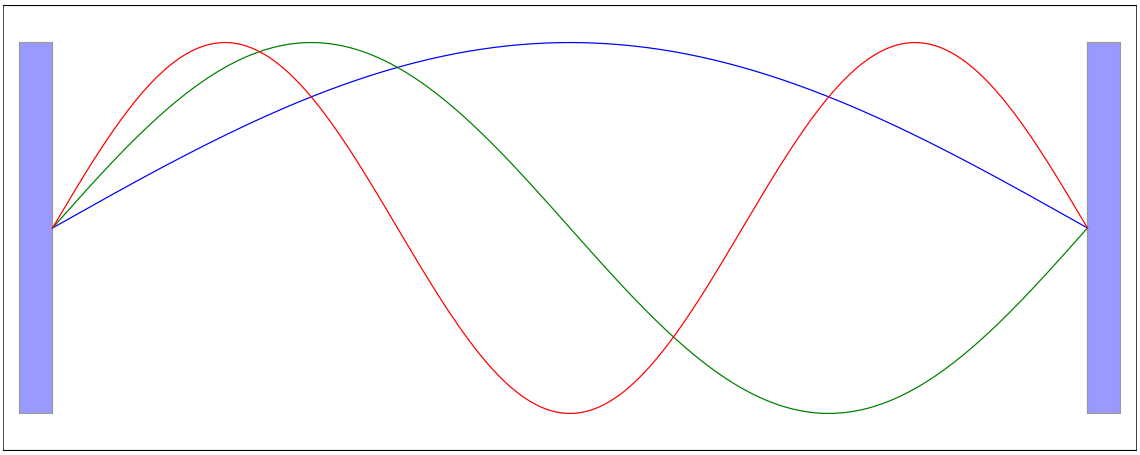

Figure 2.1: The 3 lowest-energy electromagnetic standing waves, or modes, allowed in a simple laser cavity. Usually these modes oscillate at random phases to each other, interfere and average out across the laser cavity. However, when the relative phase between the modes is set just right, they can constructively interfere to form intense pulses and destructively interfere everywhere else. x-axis is position, y-axis is real part of the electric field.

Stable ultrafast optical pulses are obtained from mode-locked lasers—that is, lasers in which the longitudinal standing electromagnetic waves in the laser cavity, or "modes," are locked into phase with each other by passive means [6, 7, 8, 9]. As shown in figure 2.1, an optical cavity, which in its simplest form is a pair of parallel mirrors facing each other, allows only a half-integer number of wavelengths in a standing wave inside it. The number of wavelengths in a specific wave is known as the "wave number," or "mode number." Which allowed modes actually exist in a cavity depends on the gain crystal of the laser, which amplifies

the light. All waves allowed by the gain crystal and the cavity length can exist in a cavity at once and, without mode-locking, their relative phases oscillate such that they interfere with each other and average out to a constant intensity. However, when a laser is mode-locked, this phase is fixed such that the modes all constructively interfere with each other at regular intervals, producing extremely short high-intensity pulses, and destructively interfere with each other to "cancel out" at all other times [6, 7, 8, 9].

A laser can be mode-locked by placing a material inside the laser cavity that absorbs a (proportionally) large percentage of light at low intensities, but allows higher intensity light to pass through with reduced absorption; such a material is called a saturable absorber. When a laser is not mode-locked, the intensity of the light that bounces around the cavity fluctuates semi-randomly due to the constructive and destructive interference between allowed modes. A saturable absorber placed in the cavity will attenuate the higher intensity fluctuations to a lesser degree than the lower intensity ones. After many such attenuations, the low intensity fluctuations are absorbed away entirely and a pulse train forms. Even then, the saturable absorber improves the pulses.

As shown in figure 2.2, the low-intensity leading and trailing parts of each pulse are attenuated more strongly than its high-intensity pulse center. This makes the newly formed pulses shorter and shorter over several iterations until a pulse-width of just a few femtoseconds is attained. The width of this pulse then depends on the gain bandwidth of the gain material and on the response time of the saturable absorber. The more frequencies that the gain material produces in a laser (i.e., the more modes generated inside the laser cavity), the narrower a pulse can be. Similarly, as a general trend, the faster a saturable absorber can respond to light, the shorter the pulse can be [6, 7, 8, 9].

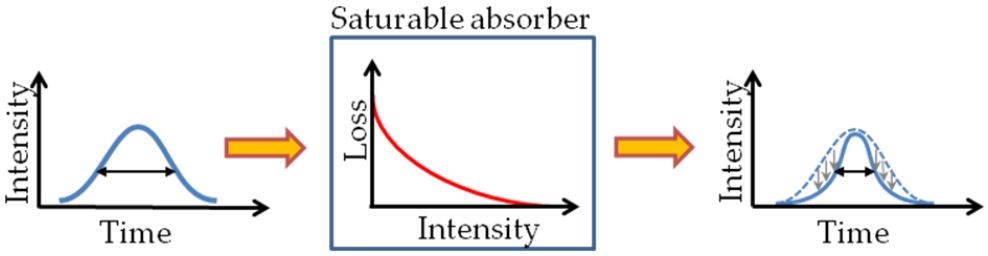

Figure 2.2: When passing through a saturable absorber, the low-intensity "wings" of a pulse experience higher loss than the intense pulse center. This causes the duration of the pulse to shrink. Taken from [37].

There are three broad classes of saturable absorber: active saturable absorbers, Kerr lens saturable absorbers, and semiconductor saturable absorbers. Active saturable absorbers control the total loss in a laser cavity by optoelectronics. For an active saturable absorber, the loss increase or decrease is often effected in one of three ways: by an acousto-optic modulator (AOM)—a device which takes advantage of the pressure-dependence of the index of refraction of certain materials—which defocuses the undesired low-intensity light so that it escapes the laser cavity, by an electro-optic modulator (EOM)—a device with an optical absorption dependent on an applied voltage—or, in the case of solid-state lasers, by controlling the energy of the pump laser which feeds power into the laser cavity. Because active saturable absorbers are limited by electronic response time, they produce the widest pulses [6]. However, for fast saturable absorbers, active electronic feedback can stabilize a laser mode-locked by another saturable absorber without affecting pulse formation.

Kerr lens saturable absorbers take advantage of the optical Kerr effect, which is the second-order term in a Taylor expansion of a given material's index of refraction in terms of intensity:

$$n = n_0 + n_{Kerr} I, \tag{2.1}$$

where n is the index of refraction of the material, n_0 is the linear term of the index of refraction (usually considered the index of refraction), n_{Kerr} is the first order term of the index of refraction, and I is the intensity of light shining on the material. For Kerr-lens mode-locked lasers, an aperture of some sort is placed in the cavity. Then, by taking advantage of the Kerr effect, a high-intensity pulse center can be allowed to self-focus through the Kerr lens material so that it passes through the center of the aperture with minimal loss, while the low-intensity pulse "wings" are blocked because they do not strongly interact with n_{Kerr}. Because the optical Kerr effect responds to light near instantaneously, Kerr-lens model-locked lasers produce the shortest pulses of any mode-locked laser. However, because Kerr-lens mode-locking requires careful alignment of the cavity so that the self-focusing gives high-intensity light more gain, Kerr-lens mode-locked lasers are very sensitive to environmental fluctuations and can become unstable over time [6].

Semiconductor saturable absorbers, which will be the focus (no pun intended) here, are materials with significant second order and higher terms in their Taylor expansion of absorption in terms of incident

intensity:

$$\begin{aligned} A(I) &= A_0 + A_1 I + A_2 I^2 + ... \\ &= A_0 + \sum_{i=1}^{\infty} A_i I^i, \end{aligned} \tag{2.2}$$

where A_0, A_1, etc. are the absorption coefficients and I is incident intensity. For reasons discussed below, A_1, A_2, A_3, etc. (referred to as A_i from now on) are negative and A_0 is positive. Because A_i is often extremely small, the higher order terms only appear at high intensities. For this reason, saturable absorption in semiconductors is also referred to as nonlinear absorption, while A_0 is referred to as linear absorption. As will be discussed later, assuming a continuous beam of light and weak saturable absorption, this Taylor series can sometimes be approximated as

$$A(I) = \frac{A_0}{1 + \frac{I}{I_0}}, \tag{2.3}$$

where I_0 is a scale of how quickly saturable absorption becomes important. It is usually an extremely large value. The above form of saturable absorption is only valid when it is reasonable to speak about intensity with regards to a saturable absorber. In the case of extremely short optical pulses, a saturable absorber will only see the average over the energy of the entire pulse and it makes more sense to describe saturable absorption as the Taylor series of absorption in terms of the fluence of the pulse. The Taylor series is analogous:

$$\begin{aligned} A(F) &= A_0 + A_1 F + A_2 F^2 + ... \\ &= A_0 + \sum_{i=1}^{\infty} A_i F^i, \end{aligned} \tag{2.4}$$

where A_0 is the linear absorption coefficient and the A_is are the analogous coefficients to make the absorption of a material scale correctly with fluence.

How quickly a semiconductor saturable absorber responds to light is related to the electronic transport properties of the material. For this reason, the pulse width produced by a laser mode-locked by a semiconductor saturable absorber depends strongly on the semiconductor material chosen. The pulse width is often narrower by several orders of magnitude than that produced by an active saturable absorber but wider than that produced by a Kerr-lens saturable absorber. Semiconductor saturable absorbers also quench

Q-switching instabilities, but they do so less strongly and reliably than systems with active feedback [6].

2.2 The Physics of Semiconductor Saturable Absorbers

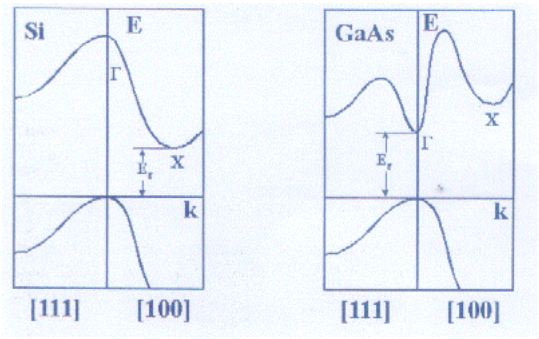

Figure 2.3: The band structure of two common bulk semicondoctors: (left) silicon and (right) gallium arsenide. x-axis is wave vector, $k = p/\hbar$. y-axis is energy. Image reproduced from [42].

2.2.1 Band Structure

To understand how nonlinear absorption works in a semiconductor saturable absorber, one must first understand a little bit about semiconductor physics. Quantum mechanics tells us that electrons in a material are restricted to discreet energies and momenta, called states [43, 44]. In real systems, there are usually so many allowed states, with so small a difference between them, that one can approximate them as continuous manifolds[1] of allowed energy and momentum, or bands [45]. We usually plot bands as the energy of allowed states as a function of momentum, $E(\bar{P})$. Figure 2.3 shows a two-dimensional plot of the band structure of some common semiconductors. In theory, every material has infinitely many bands that can overlap, touch at one point, or be separated by a "bandgap" (also referred to as a "band gap"), a range of energy where there are no allowed states.[2] However, most of these bands exist at such high energies that any electron in them would escape the material entirely. As such, usually only the two lowest-energy bands are relevant. The lowest energy band is called the "valence band," and the second lowest, the "conduction band." The space which these bands live in is called the first "Brillouin zone," which is the set of momenta corresponding

[1] A manifold is the generalization of a curve, surface, or volume. It is a continuous set of points in an arbitrary number of dimensions.

[2] In a bulk crystal, one can think of the bandgap as the set of energies and momenta at which the electrons are sensitive to the crystalline structure of the material and destructively interfere.

to the primitive unit cell for a crystal in real space by a Fourier transform. The momentum associated with the origin of the Brillouin zone is called "Γ," and the point on the manifold associated with Γ is called the "gamma point" [45]. We will call the point with the highest-energy in the valence band the "K point" and the momentum associated with it K. We will call the energy associated with the K point the "Dirac point." Although Γ and K are standard notation, the Dirac point may not be.

As the names of the bands imply, the band structure of a material is closely related to its conductivity. Electrons are fermions, so the Pauli exclusion principle allows only one electron per state, or per point on the manifold of a band [43, 44]. As one adds electrons to a material, the energy of the highest energy electron (called the "Fermi level" or "Fermi energy," denoted ϵ_f) becomes higher and higher. Assuming the bands don't overlap, then if the Fermi level of a material is at the K point, then there are no empty states for an electron to move into without a large increase in energy compared to the energy of an individual electron to overcome the bandgap. This means that in position space as well as in momentum space,[3] there is no place for an electron to move to if it is perturbed, and current cannot flow, even if one applies a voltage. A material like this is said to be an "insulator," or in an "insulating phase" [45].

If the Fermi level is somewhere in the conduction band, then there are many places for the higher-energy electrons to go if perturbed, and thus a current of electrons flows if one applies a voltage. A material in this state is said to be in an "electron conducting phase." If the Fermi level is below the K point, somewhere in the valence band, then a perturbed electron has fewer places to go than if the Fermi level were in the conduction band. However, the electrons in the material can shuffle around to fill a "hole" in the "electron sea." This opens up a hole elsewhere, and a current of holes (i.e., the absences of electrons) flows if one applies a voltage. These holes carry a positive charge because the absence of an electron means that the positive charge from the nuclei of the atoms in the material is visible at the point of the hole. A material in this state is said to be in a "hole conducting phase." The further the Fermi level is from the K point, the higher the conduction of the material is, since there are more electrons or holes to conduct [45].[4]

Figure 2.4 shows the various ways a material with a bandgap can insulate or conduct by using traffic

[3] Position and momentum wavefunctions are related by a Fourier transform, or Plancherel's Theorem: $f(x) = \frac{1}{\sqrt{2\pi}} \int_{-\infty}^{\infty} F(k) e^{ikx} dk \Leftrightarrow \frac{1}{\sqrt{2\pi}} \int_{-\infty}^{\infty} f(x) e^{-ikx} dx$ [43, 44]

[4] Remember that the Fermi level cannot be in the bandgap, since there are no states for the highest-energy electron to inhabit in this region.

on a highway as an analogy. If the material is in an insulating phase, then the Fermi level is at the K point and all the electrons are stuck in their own states, since there are no states available to move into. This is like a traffic jam; no car can go anywhere because there is no space. If the material is in an electron-conducting phase, then the Fermi level is in the conduction band, and the electrons in the conduction band have many open states to move into if perturbed slightly. This is equivalent to an empty highway. If the material is in a hole-conducting state, then the Fermi level is below the K point, somewhere in the valence band. Electrons don't have much mobility because they're still mostly crowded. However, the empty states, or holes, can travel through a material as electrons shuffle to fill the gap under an applied field. This is like a busy highway, where there are gaps between blocks of traffic. The cars may be moving relatively slowly, but the gap between the cars can travel quickly in the opposite direction.

It is worth noting that this is not the only way, or even the most common way, a material can be a conductor. If the valence and conduction bands of a material overlap, there are always many open states for electrons to move into, and the material is a conductor. If the bandgap of a material is relatively small, then a minor change in the Fermi level of the material can cause it to change from conducting to insulating phase and vice-versa. Such a material is called a semiconductor. If the bandgap of a material is extremely large, then it is often impossible for the Fermi level to pass the bandgap and go from the valence band to the conduction band. Assuming no charge-carrying electrons are removed, then, the material is stuck in the insulating phase. Such a material is an insulator [45].

2.2.2 The Interaction Between Light and Matter

Although saturable absorption is a complicated process, it can be completely described by the behavior of a simple two-level system. Once the two-level system has been studied, it can serve as an analogy to the band structure of a material, and the individual material's nonlinear properties become apparent. Consider a system of two energy-levels (call them E_0 and E_1) separated by a distance ΔE. Each level has infinitely many states in it, so that infinitely many electrons may inhabit either energy level. It is irrelevant what types of states these are, but for simplicity they will be said to be momentum states in a single direction. An electron in such a state has momentum $\bar{p}$ (not to be confused with power, $P(t)$). So there are two bands,

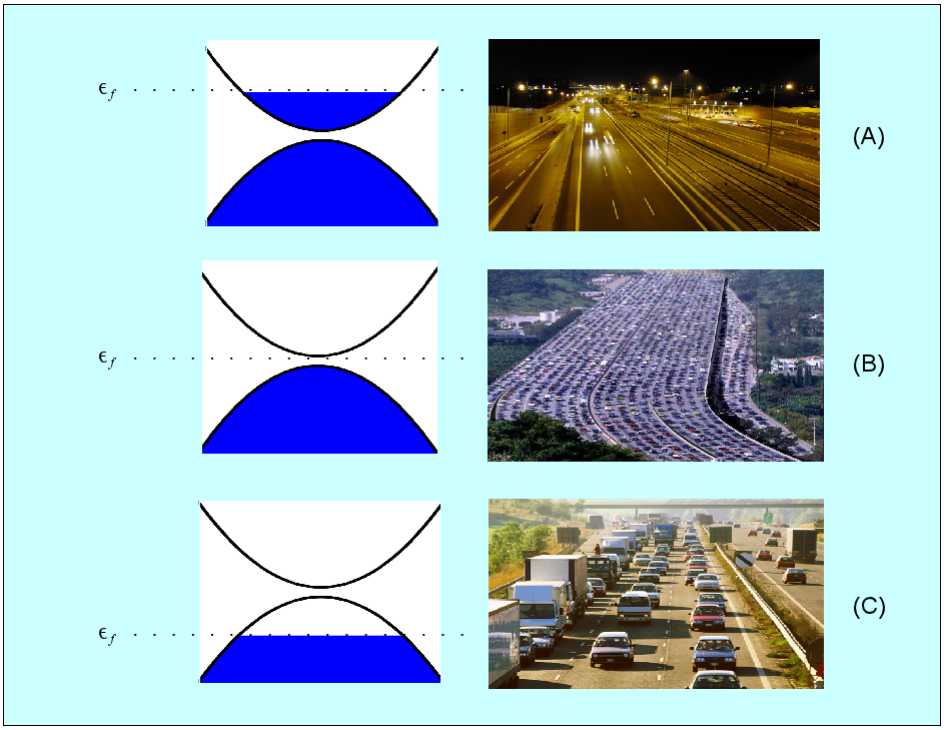

Figure 2.4: The different "conduction phases" of a semiconductor material are analogous to traffic on a road. (A) If the Fermi level is above the K point, somewhere in the conduction band, then there are many states for electrons to occupy and they can flow smoothly, just as traffic flows smoothly on an empty road. (B) If the Fermi level is at the K point, all of the states in the valence band are full and there is no room for motion, just as in a traffic jam. (C) If the Fermi level is below the K point, then there are just a few empty states for electrons to move into, and these empty states (or "holes") can travel through the material carrying positive charge in the opposite direction of the electron flow, just as a gap in traffic can move backwards through a line of cars on a busy road. Road images from [46, 47, 48] respectively (top to bottom).

each at a single energy—the valence band at E_0 and the conduction band at E_1, with a bandgap of ΔE—and with wave-vectors extending from $k = -\infty$ to $k = \infty$. The wave-vector is defined as

$$\bar{k} \equiv \frac{\bar{P}}{\hbar} \tag{2.5}$$

and it will be used here to clean things up notationally a little bit. The function $P(t)$ will be used to refer to instantaneous optical power. Note that in this simple example K is not well defined. All states in the valence band are at the same energy level, so the idea of a K point has no meaning.

Let the system start in the conduction phase,[5] with $\epsilon_f = E_0$. If a photon with energy[6] ΔE hits

[5] The system doesn't really have insulating and conducting phases because it has infinitely many states for its electrons to inhabit and thus electron flow is unlimited. However the terminology is useful.

[6] The energy of a photon is related to its wavelength by Planck's constant (h): $E = \frac{hc}{\lambda}$, where c is the speed of light.

the material containing this system, the photon can be absorbed with some probability, called B_{12}. If the photon is absorbed, its energy is transferred to one of the electrons in its ground state (with energy E_0 and wave-vector k_0), and the electron is excited into the conduction band (also called the electron's excited state). The electron also gains the momentum of the absorbed photon. However, since the momentum of an electron is substantially greater than the momentum of a photon (at least at the relevant energies), it can be assumed that the electron's change in momentum is zero. So, after the photon has been absorbed, one electron has moved from its position in the valence band to an analogous position in the conduction band. It now has energy $E_1 = E_0 + \Delta E$ and the same wave-vector, k_0. As one would expect, this process is called absorption. If the energy of an incident photon matches the energy difference between the two bands (the energy of the band gap), absorption has a probability of occurring whenever an electron is in the valence band. However it becomes substantially more likely as the number of electrons in the valence band increases. To first order, if the energy of an incident photon does not match that of the bandgap, absorption cannot occur.

Now consider the reverse situation, where the system is completely in the conducting phase. In this case, the system starts with all of its electrons in the conduction band. Note that this is a completely unphysical situation. There are usually many more electrons in the valence band than can fit in the conduction band. It is also a thermodynamically unstable state, and it does not last in nature. All electrons eventually return to the ground state through processes such as fluorescence, electron-electron scattering, and electron-phonon, i.e., electron-lattice, scattering. However, in this hypothetical two-level system, there is infinite space.

If a photon with energy ΔE hits the material now, rather than transferring its energy and momentum to an electron, it has some probability of triggering a shift in an electron from the conduction band into the valence band (again with a negligible change in momentum). If the electron does shift, it emits a second photon with the exact same energy and momentum as the original photon. (The energy of the emitted photon must be the same as that of the incident photon, because there is only one allowed transition for the electron to make, and it has energy ΔE. That the momentum of the emitted photon is the same is a substantially less intuitive result; the only way to see this is to treat a light wave as a time-dependent

perturbation to this two-level system and calculate an approximate solution.) One photon enters the system and two identical photons leave it. This process is called stimulated emission. Stimulated emission has a probability of occurring whenever there is an electron in the conduction band, but it grows substantially more likely as the number of electrons in the conduction band increases.

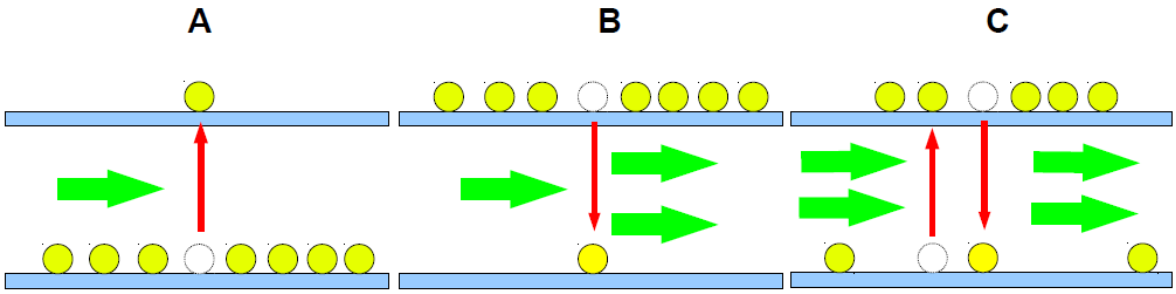

Figure 2.5: (A) Absorption, (B) stimulated emission, and (C) saturable absorption. In absorption, an incident photon (represented by an arrow) excites an electron from the valence band to the conduction band and disappears as it transfers its energy and momentum to the electron. In stimulated emission, an incident photon causes an electron to decay from the conduction band to the valence band, emitting a photon with the same energy and momentum as the stimulating photon; both the original photon and the emitted photon then exit the material. In saturable absorption, a steady state between absorption and stimulated emission is reached.

It is possible to reach a steady state between absorption and stimulated emission, where the number of electrons excited into the conduction band by absorption is equal to the number of electrons that decay into the valence band through stimulated emission (and other processes such as electron-electron and electron-phonon[7] scattering). This steady-state between absorption and stimulated emission is referred as "saturable absorption," and it is the source of the higher order terms of the absorption in terms of intensity referred to in equations 2.2, 2.3 and 2.4. Figure 2.5 shows a graphical representation of absorption, stimulated emission, and saturable absorption in this simple two-level system.

When the steady state for a system occurs depends on certain inherent traits of the system: the time it takes the electrons in the conduction band to decay into the valence band without stimulated emission—or better yet, the time it takes for the probability of stimulated emission to decrease to zero—called the relaxation time of the absorber, τ_A, and the amount of energy (i.e., the number of photons) required to excite

[7] A phonon is the quantization of lattice vibrations in a material—a quantized sound wave— and electron-phonon scattering can be thought of as electrons hitting the vibrating crystal lattice.

enough electrons into the conduction band such that the probability of absorption is $1/e$ that of a saturable absorber in the insulating phase, called the saturation energy, $E_{sat,A}$. In a simple two-level system, these traits are arbitrary. In a physical semiconductor system, they are determined by the band structure.

2.2.3 The Dynamics of Saturable Absorption

To treat the saturable absorption in the time domain, some more assumptions must be made. The following treatment of the time-dependent behavior of a saturable absorber comes from Ursula Keller [6], who nicely summarizes saturable absorbers and their role in mode-locking. Keller's treatment is specifically for SESAMs, and she thus treats saturable absorbers only in the context of mirrors, which have a transmission coefficient of $T = 0$. This treatment is slightly modified to be more general. These absorbers have nonzero transmission and absorption coefficients, and the reflection coefficient is accounted for in the absorption coefficient, since such reflected light is lost. Keller's view can easily be recovered by setting $R = T^2$. Keller calls the electric field as a function of time $A(t)$ and does not give a name to the absorption coefficient. Here $A(t)$ will be defined as the absorption coefficient,

$$A(t) = 1 - T(t), \text{ where } T(t) = I_{out}/I_{in}. \tag{2.6}$$

The transmission of material, $T(t)$ can be redefined as

$$T(t) = e^{-2q(t)}, \tag{2.7}$$

where $q(t)$ is an arbitrary function that will be used to make $T(t)$ come out right, such that $q(0) = q_0$ and $T(0) = e^{-2q_0}$. Intuitively, $q(t)$ is proportional to the number of electrons in the conduction band. Thus, the more electrons there are in the conduction band, the less absorptive the system is. Soon, the instantaneous optical intensity of a pulse $I(t)$ will be discussed. It is important to note that this intuitive idea of $q(t)$ is only correct for a normalized optical pulse:

$$\frac{2}{cn\varepsilon_0}\int I(t)dt = 1,$$

where c is the speed of light, n is the index of refraction of a material, and ε_0 is the vacuum permittivity. This framework was chosen for convenience.

One can then argue that the change in saturable absorption must depend on two components: the rate of decay of electrons from the conduction band to the valence band—or the rate of recovery from the steady-state—and the rate of excitation of electrons from the valence band into the conduction band—or the rate of absorption at the moment, which is the probability of absorption times photon flux. These terms can be combined to construct the following differential equation, called the Rate Equation,

$$\frac{dq(t)}{dt} = -\frac{q(t) - q_0}{\tau_A} - \frac{q(t)P(t)}{E_{sat,A}}, \tag{2.8}$$

where $P(t)$ is the power of some light being shone on the absorber, τ_A is the relaxation time of the absorber, and $E_{sat,A}$ is the energy required to saturate the absorber as discussed in section 2.2.2.[8] The Rate equation is not a derived formula. Rather it is an intuitive guess at what might be a good model of the system: The change q to first order might be some Δq divided by some timescale, and to second order, it might be the probability of absorption—which is proportional to power times some scaling factor: the more photons pass through a material per second, the more likely one will be absorbed.

It is usually assumed that the light is an optical pulse with full width, half maximum (FWHM) duration called τ_p. While it seems very restrictive to assume a pulse, this is actually extremely general, since one can take the limit as $\tau_p \to \infty$ to find the behavior for a continuous beam of light, or construct a pulse shape and only look at part of it to model nearly any continuous $P(t)$.

This differential equation can be solved by integrating factors.

2.2.3.1 The General Solution

Equation 2.8 can be rearranged to take the form

$$q'(t) + \left(\frac{1}{\tau_A} + \frac{P(t)}{E_{sat,A}}\right) q(t) = \frac{q_0}{\tau_A}, \tag{2.9}$$

where $q'(t)$ is Newtonian notation for $\frac{dq(t)}{dt}$. This form more clearly shows that the Rate Equation is a linear first order differential equation (ODE) of the form

$$q'(t) = h(t)q(t) + j(t), \tag{2.10}$$

[8] It is worth noting that this model breaks down at extremely large $q(t)/q_0$, however lasers rarely operate in this regime, so the model is usually quite accurate.

where $h(t)$ and $j(t)$ can be anything in general. In this case,

$$h(t) = \left(\frac{1}{\tau_A} + \frac{P(t)}{E_{sat,A}}\right) \texttt{ and } j(t) = \frac{q_0}{\tau_A}. \tag{2.11}$$

To obtain a solution, equation 2.10 is multiplied by an "integrating factor," $M(t)$:[9]

$$M(t)q'(t) + M(t)h(t)q(t) = M(t)j(t). \tag{2.12}$$

If the integrating factor is constrained such that

$$\frac{d}{dt}M(t) := M(t)h(t), \tag{2.13}$$

then the product rule reveals that

$$\frac{d}{dt}\left[M(t)q(t)\right] = M(t)q'(t) + q(t)M'(t) = M(t)q'(t) + M(t)h(t)q(t). \tag{2.14}$$

But this is the left hand side of equation 2.10. So,

$$\begin{aligned} \frac{d}{dt}\left[M(t)q(t)\right] &= M(t)j(t) \\ \Rightarrow q(t)M(t) &= \int M(t)j(t)dt + c \\ \Rightarrow q(t) &= \frac{1}{M(t)}\left[\int M(t)j(t)dt + c\right]. \end{aligned} \tag{2.15}$$

To find out what $M(t)$ is, recall equation 2.13 and solve by separation of variables:

$$\begin{aligned} \frac{d}{dt}M(t) &= M(t)h(t) \Rightarrow \frac{1}{M(t)}\frac{dM(t)}{dt} = h(t) \\ \Rightarrow \int \frac{1}{M(t)}dM &= \int h(t)dt \Rightarrow \texttt{ln}(M(t)) = \int h(t)dt \\ \Rightarrow M(t) &= e^{\int h(t)dt}. \end{aligned} \tag{2.16}$$

Apply this method to equation 2.9, it becomes clear that

$$\begin{aligned} M(t) &= \exp\left[\int \frac{1}{\tau_A} + \frac{P(t)}{E_{sat,A}}dt\right] = \exp\left[\frac{t}{\tau_A} + \frac{E(t)}{E_{sat,A}}\right] \\ \Rightarrow M(t) &= \exp\left[\frac{t}{\tau_A} + \frac{F(t)}{F_{sat,A}}\right], \end{aligned} \tag{2.17}$$

where the relationship that $E(t) = \int P(t)dt$, where $F(t)$ is the energy of the pulse as a function of time and the relationship that fluence, F is energy divided by area is used. Thus,

$$q(t) = \frac{q_0}{\tau_A}e^{-t/\tau_A}e^{-F(t)/F_{sat,A}}\left[\int_{-\infty}^{t} e^{u/\tau_A}e^{F(u)/F_{sat,A}}du + \tau_A\right]. \tag{2.18}$$

[9] Integrating factors are covered in great depth by Braun [49].

The total intensity transmission coefficient for a single pulse is then

$$T_{pulse} = \frac{I_{pulse,out}}{I_{pulse,in}} = e^{-q_p} \ \texttt{where} \ q_{pulse} = \int_{-\infty}^{\infty} q(t)dt. \tag{2.19}$$

Unfortunately, the integral over the fluence often does not exist in closed form. For instance, for a class of lasers called "Soliton lasers," it is very reasonable to assume a pulse shape of

$$P(t) = \text{sech}^2(t/\tau).$$

If this is assumed, then

$$F(t) = \tau_P \tanh(t/\tau_P),$$

and the integral

$$\int_{-\infty}^{t} e^{-u/\tau_A} \exp\left[-\frac{\tau_P}{F_{sat,A}}\tanh(u/\tau_p)\right] dt$$

has no closed form and must be evaluated numerically. Fortunately, the exact general solution is rarely required because most saturable absorbers fall into one of two approximate regimes. They are are either fast saturable absorbers, or slow saturable absorbers.

2.2.3.2 Slow Saturable Absorbers

If one assumes that the duration of any optical pulse that hits the absorber is much shorter than the relaxation time of the absorber ($\tau_p << \tau_A$), then the term in the rate equation relating to the recovery time of the absorber is negligible, since the other term will be much larger ($P(t) >> E_{sat,A}$). The rate equation then becomes

$$\frac{dq(t)}{dt} \approx -\frac{q(t)P(t)}{E_{sat,A}}. \tag{2.20}$$

This equation is solvable in general (or at least as general as a physicist likes to be) by separation of variables.

$$\begin{aligned}
\frac{dq(t)}{dt} &= -\frac{q(t)P(t)}{E_{sat,A}} \Rightarrow \frac{1}{q(t)}\frac{dq(t)}{dt} = -\frac{P(t)}{E_{sat,A}} \\
\Rightarrow \int_{t=-\infty}^{T} \frac{1}{q(t)}\frac{dq(t)}{dt}dt &= -\frac{1}{E_{sat,A}}\int_{t=0}^{T} P(t)dt \Rightarrow \int_{q(t)=q(0)}^{q(T)} \frac{1}{q(t)}dq = -\frac{1}{E_{sat,A}}\int_{t=0}^{T} P(t)dt \\
\Rightarrow ln(q(t)) - ln(q_0) &= -\frac{1}{E_{sat,A}}\int_{u=0}^{t} P(u)du \\
\Rightarrow q(t) &= q_0 \exp\left[-\frac{1}{E_{sat,A}}\int_{u=0}^{t} P(u)du\right].
\end{aligned} \tag{2.21}$$

Note that the time-dependence of the optical pulse is averaged away. This means that it really only makes sense to talk about the total pulse energy (or fluence as the case may be) for a slow saturable absorber. Talking about time-dependent energy or instantaneous energy flux (intensity) does not make sense here because the saturable absorber doesn't "see" the pulse shape at all; it averages over the entire pulse. One can calculate the saturation fluence of this material, the fluence at which $A(F_{sat}) = e^{-1}A(0)$, by first rewriting the definition of the transmission coefficient and equation 2.7 in terms of fluences (remember fluence is the integral of intensity):

$$\begin{aligned} I_{trans}(t) &= T(t)I_{in} = e^{-2q(t)}I_{in} \\ \Rightarrow T_{tot} &= \frac{\int_{t=0}^{\infty} I_{trans}(t)dt}{\int_{t=0}^{\infty} I_{in}(t)dt} = \frac{F_{trans}}{F_{in}} = 1 - \frac{2}{F_{in}}\int_{t=0}^{\infty} q(t)I_{in}(t)dt, \end{aligned} \tag{2.22}$$

where I_{trans} is the transmitted intensity, I_{in} is the incident intensity, F_{in} is the fluence of the incident pulse, and F_{trans} is the fluence of the transmitted pulse. Of course, it makes no sense to talk about intensity, rather than fluence, for slow saturable absorbers. This can be solved by simply plugging the definition of fluence into the integral to get

$$T_{tot} = 1 - \frac{2}{E_p}\int_{t=0}^{\infty} q(t)P(t)dt, \tag{2.23}$$

where E_p is the energy of a pulse through the saturable absorber.

To simplify things further, the following approximation will be made. Since, physically, most saturable absorbers used in mode-locked lasers have low saturation fluences (or intensities as the case may be), the small angle approximation may be made to the transmission coefficient:

$$T = e^{-2q(t)} \approx 1 - 2q(t). \tag{2.24}$$

and thus the absorption coefficient for a whole pulse is

$$\begin{aligned} q_p(E_p) &= \frac{1}{E_p}\int_{t=0}^{\infty} q(t)P(t)dt \\ &= \frac{1}{E_p}\int_{t=0}^{\infty} q_0 \exp\left[-\frac{1}{E_{sat,A}}\int_{u=0}^{t} P(u)du\right] P(t)dt, \end{aligned} \tag{2.25}$$

where E_p is the energy of the whole pulse. At first glance, it doesn't seem possible to evaluate this integral without knowing a pulse shape. However, with the help of a simple substitution and the fundamental theorem

of calculus, the pulse shape is revealed to be irrelevant. Let

$$v(t) = -\frac{1}{E_{sat,A}} \int_{u=0}^{t} P(u)du$$

then by the fundamental theorem of calculus and the chain rule,

$$dv = -\frac{1}{E_{sat,A}} P(t)dt \Rightarrow dt = -\frac{E_{sat,A}}{P(t)}.$$

Substituting this back into $q_p(E_p)$, one finds that,

$$q_p(E_p) = -\frac{q_0}{E_{sat,A}} \int_{v=v(0)}^{v(\infty)} e^v dv$$

The limits of this integral are

$$\begin{aligned} v(0) &= -\frac{1}{E_{sat,A}} \int_{u=0}^{0} P(u)du = 0 \\ &\text{and} \\ v(\infty) &= -\frac{1}{E_{sat,A}} \int_{u=0}^{\infty} P(u)du = -\frac{E_p}{E_{sat,A}}, \end{aligned}$$

and the integral is thus

$$\begin{aligned} q_p(E_p) &= -\frac{q_0}{E_{sat,A}} \int_{v=0}^{-E_p/E_{sat,A}} e^v dv \\ &= \frac{E_{sat,A}}{E_p} q_0 \left(1 - e^{-E_p/E_{sat,A}}\right). \end{aligned}$$

Then, note that

$$\frac{F_p}{F_{sat,A}} = \frac{E_p}{E_{sat,A}} \times \frac{area}{area} = \frac{E_p}{E_{sat,A}}.$$

Thus,

$$q_p(F_p) = q_0 \frac{F_{sat,A}}{F_p}(1 - e^{-F_p/F_{sat,A}}), \tag{2.26}$$

where F_p is the fluence of a whole pulse. Note that the absorption coefficient of the slow saturable absorber does not depend at all on the pulse shape. This is to be expected, since the absorber is averaging over the entire pulse. The total absorption over a pulse is then

$$A_p(F_p) = 1 - e^{-2q_p(f_p)}, \tag{2.27}$$

and one can fit the behavior of a real slow saturable absorber to equations 2.26 and 2.27 to find its properties.

2.2.3.3 Fast Saturable Absorbers

If the pulse duration is much longer than the relaxation time of the absorber ($\tau_p >> \tau_A$), then it is reasonable to assume that the saturable absorber instantaneously absorbs some percentage of a given incident power. This is equivalent to stating that $\frac{dq(t)}{dt} = 0$ and the rate equation reduces to

$$0 = -\frac{q(t) - q_0}{\tau_A} - \frac{q(t)P(t)}{E_{sat,A}}. \tag{2.28}$$

With the differential component set to zero, q(t) can be solved for algebraically:

$$q(t) = \frac{q_0}{\tau_A \left[\frac{1}{\tau_A} + \frac{P(t)}{E_{sat,A}}\right]}.$$

Recall that

$$\frac{\tau_A}{E_{sat,A}} = \frac{1}{P_{sat,A}} \text{ and } \frac{P(t)}{P_{sat,A}} = \frac{I(t)}{I_{sat,A}} \times \frac{area}{area} = \frac{I(t)}{I_{sat,A}},$$

where $I(t)$ is intensity of the optical pulse as a function of time, and $I_{sat,A}$ is the saturation intensity for the saturable absorber. Then

$$q(t) = \frac{q_0}{1 + \frac{I_A(t)}{I_{sat,A}}}. \tag{2.29}$$

This is where equation 2.3 comes from. Note that, just as equation 2.26 didn't reference intensity, equation 2.29 doesn't reference fluence. Since a fast saturable absorber reacts instantaneously, time-averaged values don't make any sense in this context, and (therefore) neither do total energies. The total transmission coefficient for a single pulse is then

$$T_{tot} = e^{-q_p} \text{ where } q_p = \int_{-\infty}^{\infty} q(t)dt.$$

It is impossible to go any further with the fast saturable absorber without assuming a pulse shape. Schibli et al. found that if one assumes a $P(t) = \text{sech}^2(\omega t)$ pulse shape, then

$$q_p(S) = \frac{q_s}{\sqrt{S(S+1)}} \tanh^{-1}\left(\sqrt{\frac{S}{S+1}}\right) + q_0, \quad \texttt{with } S = \frac{I_{p,peak}}{I_{sat,A}}, \tag{2.30}$$

where q_s is the amplitude of q_p—the total amount of saturable loss of the absorber—and $I_{p,peak}$ is the peak intensity of a pulse [50]. The transmission of the material as a function of a total pulse is then

$$T(S) = e^{-2q_p(S)}, \tag{2.31}$$

and one can fit a real fast saturable absorber to equations 2.30 and 2.31 to solve for its saturation intensity.

2.3 Graphene

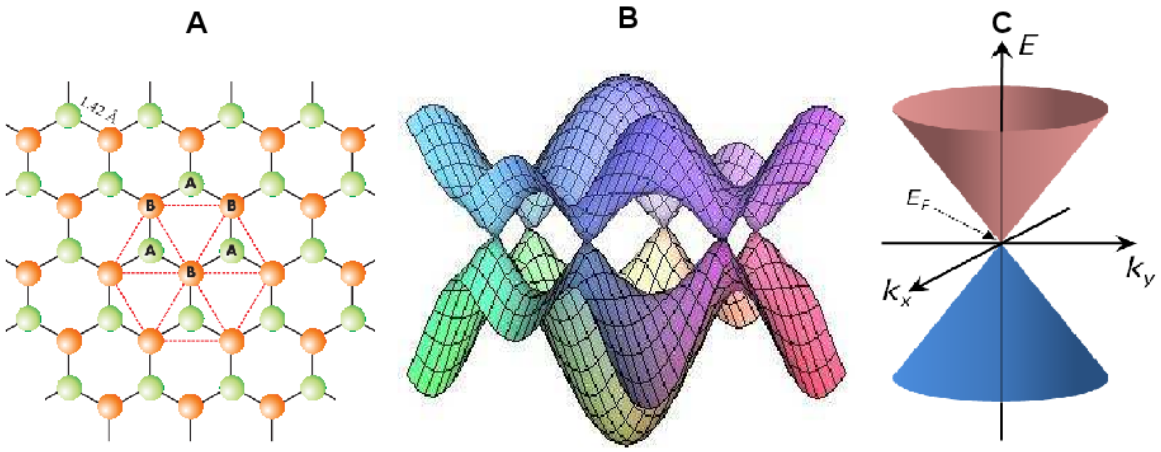

Figure 2.6: (A) Graphene's honeycomb lattice, showing the two sublattices. Green atoms compose one sublattice; orange atoms are compose the other. Taken from [10]. (B) Graphene's band structure around the first Brillouin zone. The energy where the bands meet is called the Dirac point. The 6 points where the bands meet are called the K points, with momenta K^1 through K^6. (C) Graphene's band structure near the Dirac point for Γ^1. The relationship between energy and momentum is linear here, resulting in graphene's 2.3% universal absorption and in the electrons of graphene behaving as mass-less fermions.

2.3.1 Band Structure

Graphene is a two-dimensional crystal of carbon atoms arranged in a honeycomb lattice. There are two sub-lattices, determined by the orientation of the bonds of the constituent carbon atoms. All the bonds in graphene are sp^2-type carbon-carbon bonds. These bonds are the strongest chemical bonds in the universe, and partially account for graphene's tremendous mechanical strength [51]. Figure 2.6(A) shows the two sub-lattices of graphene. Most of graphene's properties that are relevant to its application as a saturable absorber come from its band structure.

The band structure of graphene was first calculated by Phillip Russel Wallace in 1947, as a step towards calculating the band structure of graphite [27]. Wallace found that the valence and conduction bands were defined as energy as a function of wave-vector, $E(\bar{k})$, by the following equations, which were

later re-presented by Neto et al. [52]:

$$E_{\pm} = \pm t\sqrt{3 + f(\bar{k})} - t' f(\bar{k}) \tag{2.32}$$

and

$$f(\bar{k}) = 2\cos\left(\sqrt{3}k_y a\right) + 4\cos\left(\frac{\sqrt{3}}{2}k_y a\right)\cos\left(\frac{3}{2}k_x a\right), \tag{2.33}$$

where k_x and k_y are the x and y components of an electron wave-vector respectively, $a = 1.42$Å is the distance between two carbon atoms in the lattice, $t \approx 2.8$ eV is the energy required for an electron to hop from one atom in the lattice to the next one on a different sub-lattice, and t' is the energy required for an electron to hop from one atom to the next in the same sub-lattice. There is still some uncertainty about the value of t', but it has been measured to be approximately 0.1 eV [52, 53]. In this case, $E(\bar{p})$ is also called "dispersion."

Figure 2.6(B) shows the band structure of graphene in the first Brillouin zone. Unlike most materials, graphene has points where the bands touch, all at the same energy. These are called the "K points" and are indexed 1 through 6, their energy is called the Dirac point, and their momenta are called K^1 through K^6 respectively [52]. That the valence and conduction bands of graphene touch but do not overlap is a very special property, since this means that graphene has no bandgap. For this reason, graphene is called a "zero bandgap semiconductor" [52]. This property means that, no matter the energy of a photon that hits the graphene lattice, it has a probability of being absorbed. There is always an allowed energy transition for a charge-carrying electron in graphene.

If one takes the Taylor expansion of equations 2.32 and 2.33 near one of the K points in terms of a parameter,

$$q_i = \bar{k} - K^i, \tag{2.34}$$

which represents the momentum measured relative to the k point, one finds that the band-structure can be approximated as linear near the Dirac point [27, 52]:

$$E_{\pm} \approx \pm\frac{3ta}{2}|q| \equiv \pm v_F|q|, \tag{2.35}$$

where $v_F \approx 1 \times 10^6 m/s$ is the Fermi velocity—the speed that electrons are traveling through the graphene

[52]. This linear behavior has two important consequences. The first, and the most surprising, is that the Fermi velocity does not depend on the energy or momentum of the electron. In most materials, if one were to make this approximation, the first-order term in the Taylor expansion would be quadratic [45, 52]:

$$\tilde{E}(\bar{p}) = \frac{1}{2m}q^2$$

following the standard energy-momentum relation, $E = p^2/2m$. In this case, the Fermi velocity would depend linearly on momentum and thus

$$\tilde{v}_F = \frac{k}{m} = \sqrt{\frac{2E}{m}},$$

which depends on the energy of the electron [52]. This is significant because it implies that (for energies below approximately 4eV) the electrons in graphene behave as if they were mass-less particles, such as photons, with a fixed speed. This property is a substantial contributing factor to graphene's extremely high conductivity when it is in the conducting phase and one of the primary reasons that graphene exhibits so many interesting behaviors [10, 54]. The other consequence of this linear behavior is graphene's 2.3% linear absorption for photon energies below 4eV [32]. Since the size of the gap between the bands (not the bandgap!) and the density of states[10] scale linearly with momentum, the probability of absorption stays exactly the same for a wide range of photon energies. Figure 2.6(C) shows the band structure of graphene near one of the K points. Near the Dirac point, graphene's bands look like cones, called "Dirac cones," that touch at one point because the energy of charge-carriers scales linearly with the absolute value of momentum.

2.3.2 Ultrafast Properties

Figure 2.7 shows the saturable absorption process in graphene. Graphene starts in the insulating phase. Because electrons are fermions, two electrons can not inhabit the same state. So, if all states in the conduction band at an energy level $+E_{photon}/2$, are full, then electrons in the valence band at $-E_{photon/2}$ can not be excited into the conduction band, where E_{photon} is the energy of an incident photon. Furthermore, because stimulated emission generates a photon of the exact same energy as the stimulating photon, it is only possible when there is an open state for the electron to decay into E_{photon} below its current energy. For

[10] The density of states is a way of accounting for approximating a system as a continuous manifold. It is the number of states per point as a function of energy and momentum.

these reasons, when an incident photon excites an electron from the valence band into the conduction band, that electron loses much of its energy and momentum first to collisions with other electrons—which occur on a femtosecond timescale—and then to collisions with atomic nuclei in the crystal lattice—which occur on a picosecond timescale—without decaying back into the valence band. This makes room for more electrons to be excited into the conduction band and prevents the excited electrons from decaying into the valence band through stimulated emission. Eventually, however, all lower-energy states in the conduction band are full, and stimulated emission becomes a prominent effect. At this point the saturable absorber begins to saturate.

Because of the two timescales for electron relaxation as described above, the relaxation time for graphene as a saturable absorber, τ_A, has two components. One, $\tau_{fast,A}$, can be approximated as though graphene were a fast saturable absorber. This is mostly caused by electrons moving away from the relevant energy level by electron-electron scattering within the conduction band, called "intraband" scattering, or intraband decay [40]. Because graphene's electrons behave as relativistic fermions (see equation 2.35), electron-electron scattering happens very quickly, on the order of 7 fs [40]. The other component, $\tau_{slow,A}$, can be approximated as though graphene were a slow saturable absorber. This is mostly caused by electrons falling into the holes they left behind in the valence band by dropping into the valence by band through the K point [40]. This will present some difficulties when trying to find graphene's properties as a saturable absorber by fitting solutions to the rate equation (equation 2.8), but for simplicity, it is easiest to simply treat graphene as a fast absorber (equations 2.28, 2.30 and 2.31). F. T. Vasko calculated the saturation intensity, saturation fluence, and relaxation time of graphene[40], and his solutions will be used when a theoretical value is needed.

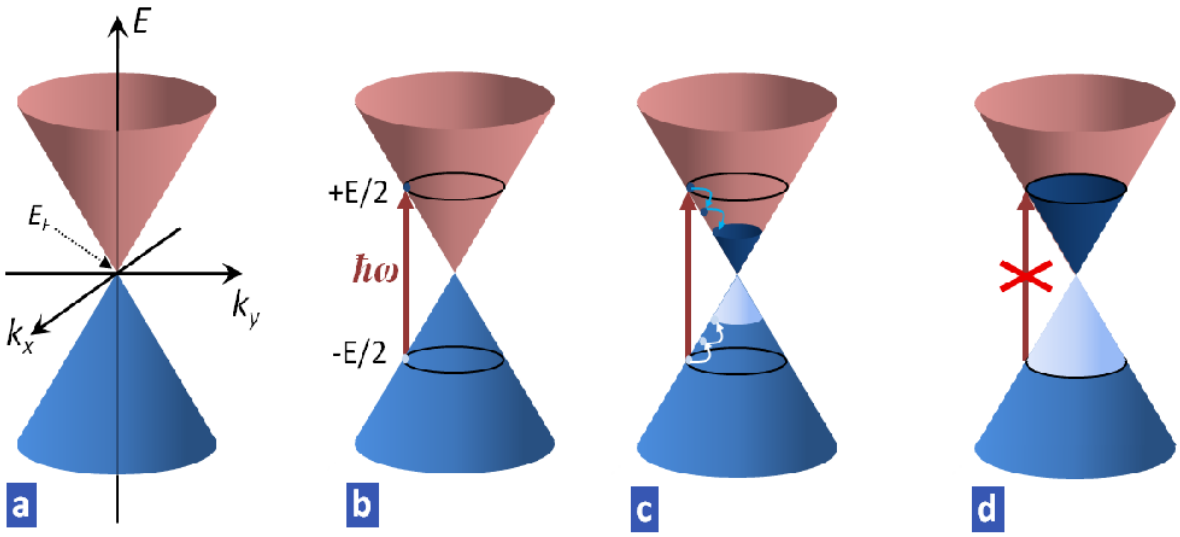

Figure 2.7: The saturable absorption of graphene near the Dirac point. (a) The low-energy band structure of graphene. Blue cone is the valence band. Red cone is the conduction band. (b) a photon with energy $E = \hbar\omega$ excites an electron from the valence band to the conduction band. (c) Electrons excited into the conduction band lose energy and momentum to the crystal lattice and to electron-electron scattering; the holes they left behind behave similarly. This allows new electrons to be excited to this same energy level and contributes to intraband relaxation time of the absorber. (d) At high enough peak intensities and pulse fluences, enough electrons have been excited into the valence band that there are no open states of lower energy in the conduction band. Absorption and stimulated emission reach a steady state and the absorber is saturated.

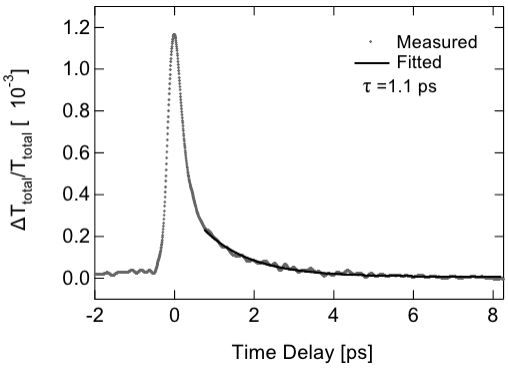

Figure 2.8: The saturable absorption of graphene as a function of time. Y-axis is change in transmission over total transmission. X-axis is time delay. Graphene has two components to its saturable absorption: one fast, the other slow. The time constant for the slow component is approximately 1.1 picoseconds. The fast component is not resolved due to the long duration of the pulses measuring the saturable absorption ($\sim$ 210 fs). Measurements in this figure made by Chien-Chung Lee.

Chapter 3

Methods for Measuring the Saturable Absorption of Graphene

3.1 Experimental Overview

The rate equation (equation 2.8) discussed in chapter 2 depends on three constants which are properties inherent to a saturable absorber: the relaxation time τ_A, the total unsaturated loss q_0, and the energy required to saturate some finite small area of the material, $E_{sat,A}$. The former can be measured by "pump-probe" experiments, also called "time-resolved spectroscopy," where a high-energy "pump" beam saturates the absorber and then, after some time delay, a lower-energy "probe" beam passes through the absorber and its intensity is measured by a photodetector. By varying the time-delay between the two beams, a picture of the time-dependent behavior of the absorber can be developed (see figure 3.7). The latter two properties can be determined by making extremely careful measurements of absorption as a function of peak intensity or pulse fluence, then fitting the resulting curve to a solution to the rate equation, such as equation 2.30. The best way to carry out this measurement is a technique called differential transmission or differential reflectivity. This Chapter will first discuss general considerations for both pump-probe and differential transmission techniques. Then differential transmission will be discussed in detail, as it was the primary diagnostic technique used in this study. Finally, pump-probe spectroscopy will be discussed only briefly, as the author did not participate in any pump-probe measurements.

3.2 General Experimental Considerations

3.2.1 The Laser

While it is theoretically possible to see saturation in a passive saturable absorber by shining a continuous (i.e., unpulsed) beam of light on it, the intensity of the light is usually nowhere near high enough. (Incidentally, a continuous beam of light is also called a "continuous wave," or "CW," and lasers emitting CW light are said to be "CW lasers," or in the "CW regime.") The saturation intensity of a fast saturable absorber is often on the order of gigawatts per square centimeter. For comparison, the Ratcliffe-on-Soar power high-efficiency coal power plant—a plant in the United Kingdom which serves approximately two million homes—has a peak output power of approximately 2 GW [55]. This means that the amount of energy Ratcliff-on-Soar puts out every second would have to be focused into a circle of radius $\sqrt{2}$ cm to achieve the peak intensity required to fully saturate a typical semiconductor saturable absorber. As discussed earlier, saturation intensity is only well-defined when referring to fast saturable absorbers. However, a continuous beam of light looks like a pulse of infinite duration, which is infinitely long compared to the relaxation time of any physical saturable absorber. Thus, all saturable absorbers behave like fast saturable absorbers when stimulated in the CW regime.

To achieve the high intensities required to observe saturable absorption in a fast saturable absorber—and to observe slow saturable absorption at all—it is necessary to generate ultrashort pulses. Recall that in the instantaneous case, intensity is the derivative of the fluence of a pulse with respect to time,

$$I = \frac{d}{dt}F(t). \tag{3.1}$$

Thus, if the same fluence is "squeezed" into a shorter pulse, $\frac{d}{dt}F(t)$ increases, and the intensity rises. The shorter the pulse, the higher the peak intensity. For this reason, passive saturable absorbers are characterized with mode-locked lasers with pulses ranging from approximately 10 femtoseconds for a Ti:sapphire laser to approximately three picoseconds from disk lasers [56].

Since the most directly measurable quantity in an optics lab is the average power of a beam of light, it is useful to be able to relate the average power of a pulsed laser to the pulse fluence and the peak intensity of a pulse. It is assumed that the pulse shape $P(t)$ (with units of watts), duration τ_P (with units of seconds), and

pulse repetition rate f_{rep} (with units of hertz) are already well known in addition to the measured average power, P_{avg}. The energy contained in a single pulse is approximately the energy the laser produces in a second—i.e., the average power–divided by the number of pulses per second. Or, equivalently, the energy in a single pulse is the average power divided by the repetition rate:

$$E_p = \frac{P_{avg}}{f_{rep}} \tag{3.2}$$

The pulse fluence is then the energy in a single pulse divided by the area occupied by the laser beam at the relevant spot, called the "spot size." Assuming a TEM_{00} Gaussian beam (a beam with a single gaussian peak in intensity, and the simplest solution to Maxwell's equations in a laser cavity) with beam radius r measured in meters, the fluence is approximately[1]

$$F_p = \frac{E_p}{\pi r^2} = \frac{P_{avg}}{f_{rep}\pi r^2}. \tag{3.3}$$

To find the peak intensity of the pulse, recall that fluence can be thought of as the integral of intenstity as a function of time, then integrate over the intensity of the pulse as a function of time, set this integral equal to the pulse fluence, and algebraically solve for peak intensity, I_{peak}. Let

$$I(t) = I_{peak} f(t, \tau_P), \tag{3.4}$$

where $f(t, \tau_P)$ is the pulse shape as a function of time and pulse duration. Then,

$$\begin{aligned} F_p &= \int_{t=-\infty}^{\infty} I(t)dt = I_0 \int_{t=-\infty}^{\infty} f(t,\tau_P)dt \ \texttt{and} \ F_p = \frac{P_{avg}}{f_{rep}\pi r^2} \\ \Rightarrow \frac{P_{avg}}{f_{rep}\pi r^2} &= I_0 \int_{t=-\infty}^{\infty} f(t,\tau_P)dt \\ \Rightarrow I_0 &= \frac{P_{avg}}{f_{rep}\pi r^2 \int_{t=-\infty}^{\infty} f(t,\tau_P)dt}. \end{aligned} \tag{3.5}$$

If one assumes a Gaussian pulse shape,

$$f(x, \tau_p) = e^{-t^2/\tau_P^2}, \tag{3.6}$$

then the integral of $f(x, \tau_P)$ is

$$\int_{t=-\infty}^{\infty} f(x, \tau_P)dt = \tau_P\sqrt{\pi},$$

[1] This value is only approximate because a Gaussian peak asymptotically approaches zero at large r. Thus, at any distance from the center of the spot, the power of the beam is non-zero. However, because about 66% percent of the power of the beam is contained in a circle of radius ω around the center of the spot, this equation is a fair approximation.

and thus

$$I_0 = \frac{P_{avg}}{\pi^{3/2} f_{rep} r^2 \tau_P}. \tag{3.7}$$

It is important to note that τ_P in this equation is merely a parameter that helps define equation 3.6. It is not the full width at half maximum[2] (FWHM) parameter, τ_{FWHM}, more likely to be used to characterize a generic pulse. In this case, the FWHM parameter is

$$\tau_{FWHM} = 2\tau_P \sqrt{ln(2)}. \tag{3.8}$$

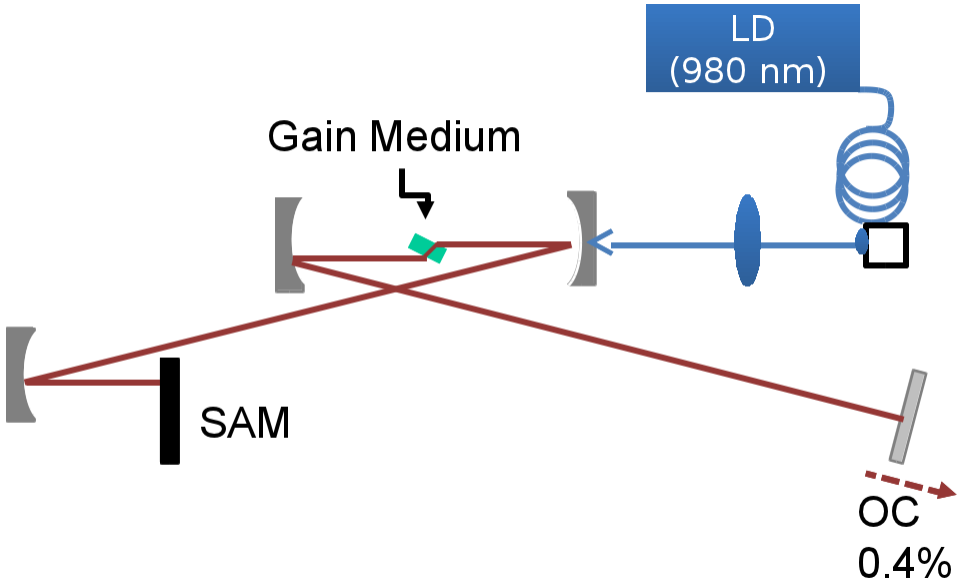

Figure 3.1: The solid state laser used for differential transmission and pump-probe experiments. The laser diode (LD) couples 980 nm light into the cavity and provides the energy for the mode-locked laser. The pump light is then fed into the gain medium, erbium- and ytterbium-doped glass (Er:Yb:glass). Mode-locking is effected by a combination of a saturable absorber mirror (SAM) placed as one end-mirror of the cavity and by Kerr-lens mode-locking from self-focusing in the gain medium. Output light passes through a partially-transparent output coupler (OC) placed as the other cavity end mirror.

Figure 3.1 shows the laser used for the pump-probe and differential transmission experiments. A laser diode (980 nm wavelength) feeds high-energy light into the cavity, which is then focused through a gain medium. The cavity is mode-locked by a combination of a saturable absorber mirror (SAM) used as one end mirror and by Kerr-lens self-focusing through the gain medium. Output light passes through a partially transparent end mirror called an "output coupler," which transmits 0.4% of incident light and reflects the

[2] Full width at half maximum, or FWHM refers to the distance between the two points on a symmetric curve, $f(x)$ such that $f(x) = 1/2$.

rest. The gain crystal is erbium- and Ytterbium-doped glass (Er:Yb:glass) with a 1.9 mm optical path length (QX/Er, Kigre, Inc.). The SAM—which operates as a slow saturable absorber in this laser—is designed for 1550 nm light, has 1% linear absorption, 0.4% non-saturable loss, 0.6 % saturable loss, and a relaxation time, τ_A, of approximately 10 ps (SAM-1550-1-X-10ps, Batope Inc.). The laser produces 1550 nm light of approximately 16 mW average power. The pulses are approximately 200 fs in duration with a repetition rate of approximately 86 MHz.

3.2.2 Lock-in Amplifiers

Most solid state gain mediums have very low gain, so a solid state laser cavity must have extremely low loss. For this reason, most desirable saturable absorbers have low loss, usually between 1% and 5%. This means that one must be able to accurately measure absorbers with a total percent absorption of 1% or less—even about 0.1% is possible. Thus, for a measurement system designed to measure saturable absorbers to be acceptably accurate, it must be able to resolve a change in absorption of 0.1% or better. This makes noise a very serious issue.

Noise is unwanted data that interferes with the interpretation of results in an experiment. In other words, it is information that is unintentionally measured. Noise can come from any number of sources, but it often comes from the internal electronics of the detection equipment. Fortunately, noise is usually random and doesn't look like any sort of result from the experiment. Unfortunately, it can make actual data (known as the signal) very difficult to read. One of the most effective methods of differentiating signal from noise is lock-in detection. A lock-in amplifier is a device that amplifies only signals that are oscillating in-phase at a specific frequency while cutting out all other signals in the input. This means that random noise is, for the most part, discarded.

A mode-locked laser carries its own noise at the output. In order to use a lock-in amplifier with this setup to test saturable absorbers, the signal must be chopped into a specific frequency. The chopping is effected spinning a grated wheel in front of the laser beam, so that the beam is periodically blocked and unblocked at the frequency to which the lock-in amplifier is tuned. This method drastically reduces noise and improves measurement accuracy.

It is important to note, however, that, a digital lock-in amplifier might show some error because of the mode-locked laser's repetition rate—i.e., the frequency over which a laser's output power oscillates between its maximum value and its minimum value. Because of this, when using a digital lock-in amplifier, it is important to filter away the repetition rate from the detector output with a low-pass filter.

3.3 Differential Transmission

3.3.1 The Goals and Theory of Differential Transmission

From a measurement perspective, absorption as a function of peak intensity and absorption as a function of pulse fluence are the same. As discussed in section 3.2.1, the most directly measurable quantity on an optics bench is average power, which averages over many pulses. Assuming that the repetition rate and pulse duration of the laser are known, it is then possible to derive the fluence or peak intensity of a pulse. This means that the intensity and fluence response of a saturable absorber can be measured by the same experiment and that, during measurement, there is no difference between a fast saturable absorber and a slow one.[3] The experimental technique used to measure both peak intensity and pulse fluence response is "differential transmission" or "differential reflectivity."

The idea of differential reflectivity is fairly simple: Shine laser light of a known intensity at a sample saturable absorber and measure how much of the laser light the saturable absorber transmits as a percentage of the laser's known total intensity. By varying the intensity, one can build a picture of the saturable absorber's behavior (figure 3.2 shows this behavior for a slow saturable absorber). This simple idea does, however, present some difficulties.

The greatest difficulty of differential transmission is that of accuracy. While a lock-in amplifier does a good job of filtering out most sources of noise, coherent[4] fluctuations in the laser output can interfere with measurement. If proper care is not taken, it is not clear whether a change in power measured after a sample comes from saturable absorption or from a change in the laser power itself. To remove this uncertainty, some

[3] This is not quite true. Whether a saturable absorber behaves as a fast saturable absorber or as a slow one can depend strongly on the duration of the pulses used to measure the absorber. However, so long as one is careful to note the measurement regime, this is not an impairment to the reproducibility of results.

[4] In this case, "coherent" refers to the fact that the phase of the laser light–and thus the noise–is locked with respect to itself. The way the light interferes with itself (constructively or destructively) does not change with time.

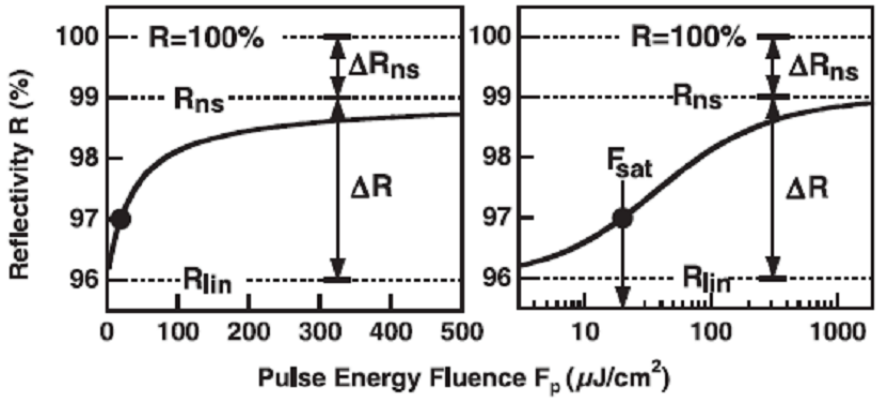

Figure 3.2: The absorption for a semiconductor saturable absorber mirror as a function of pulse fluence for a slow saturable absorber (left: linear scale, right: log scale). $R_{ns} = 1 - e^{-q_0}$ represents the non-saturable loss of the absorber. ΔR_{ns} is the difference between 0% loss and R_{ns}. R_{lin} is the unsaturated, or linear, loss of the absorber. F_{sat} is the saturation fluence, previously called $F_{sat,A}$. The curve for fast saturable absorbers as a function of intensity looks qualitatively very similar. On the log-linear scale, the absorption curve looks like an error function, demonstrating the exponent in the integrating factor in equation 2.17. Plots from [26].

"trick" or technique must be devised. The "differential" in the name "differential transmission" comes from the conceptualization of this trick. The following discussion borrows heavily from Haiml et al. [26] and from Maas et al. [57]. However, neither Haiml et al. nor Maas et al. sufficiently describe the implementation of differential transmission. The discussion of these important details is original and first appeared in a poster by the author [37].

Because the noise from a laser is coherent, it is possible to subtract it away using two photodetectors; one detector measures the intensity of light that passes through a saturable absorber sample, while the other detector measures the coherent noise. The difference between the two detector outputs is taken, resulting in a clean signal [26, 57]. When making a measurement, the laser beam is split in two before reaching the sample. One beam is sent directly into a detector. This is called the "calibration beam," and it goes into detector (A), at the end of the "calibration arm" of the setup. The other beam is sent through the sample before passing into a detector. This is the "sample beam," and it goes into detector (B), at the end of the "sample arm" of the setup.

By by measuring all data simultaneously and subtracting the outputs from the two detectors, the coherent laser noise can be avoided. As figure 3.3 shows, this technique is not limited to time-independent

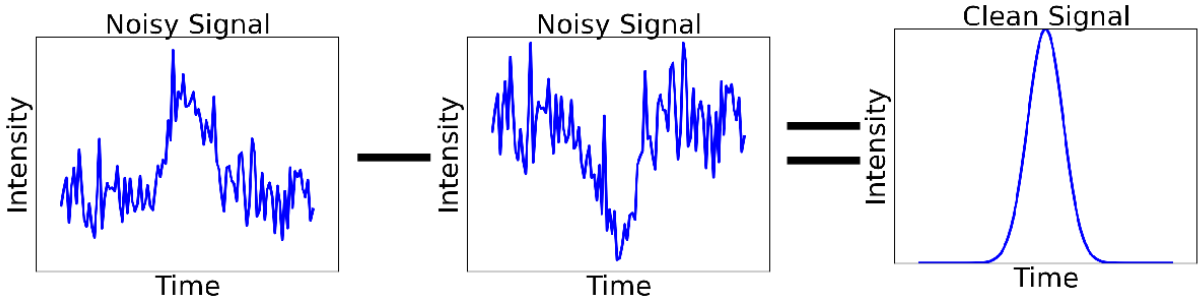

Figure 3.3: The differential measurement technique in its most general form. A time-dependent signal with coherent noise is subtracted from another signal with the *same* coherent noise, but a different signal (the same signal inverted, a null signal, and the same signal but reduced are all acceptable). The resulting difference is a clean signal.

signals. In the case of saturable absorbers, a time-independent output is desired, so the two signals whose difference is taken are the same aside from a constant offset due to absorption by the sample. However, the differentiated signals can be different, so that the resulting output signal is time-dependent.

To extract the transmission through the sample, it is necessary to perform some basic calculations. Let A be the output from photodetector (A) and let B be the output from photodetector (B). Then the transmission through the sample is

$$T = \frac{\text{transmitted intensity}}{\text{incident intensity}} \approx \frac{B}{A}.$$

However, this equation does not take advantage of the use of two detectors. A more useful, mathematically equivalent expression is

$$T \approx 1 - \frac{A - B}{A}. \tag{3.9}$$

While equation 3.9 increases statistical uncertainty slightly by adding a mathematical operation through which error can be propagated,[5] it drastically reduces systematic uncertainty by removing coherent noise—a much larger source of error than statistical uncertainty. Figure 3.4 shows a schematic of the differential transmission setup used to study graphene.

For this differential technique to work properly, one must ensure that the relationship between the outputs from detector A and detector B accurately represents the absorption of the sample and that this

[5] Recall that statistical error depends on the partial derivatives of an equation added in quadrature, which means that a more complex formula can have additional error that does not cancel out compared to a less complex formula for the same quantity [58].

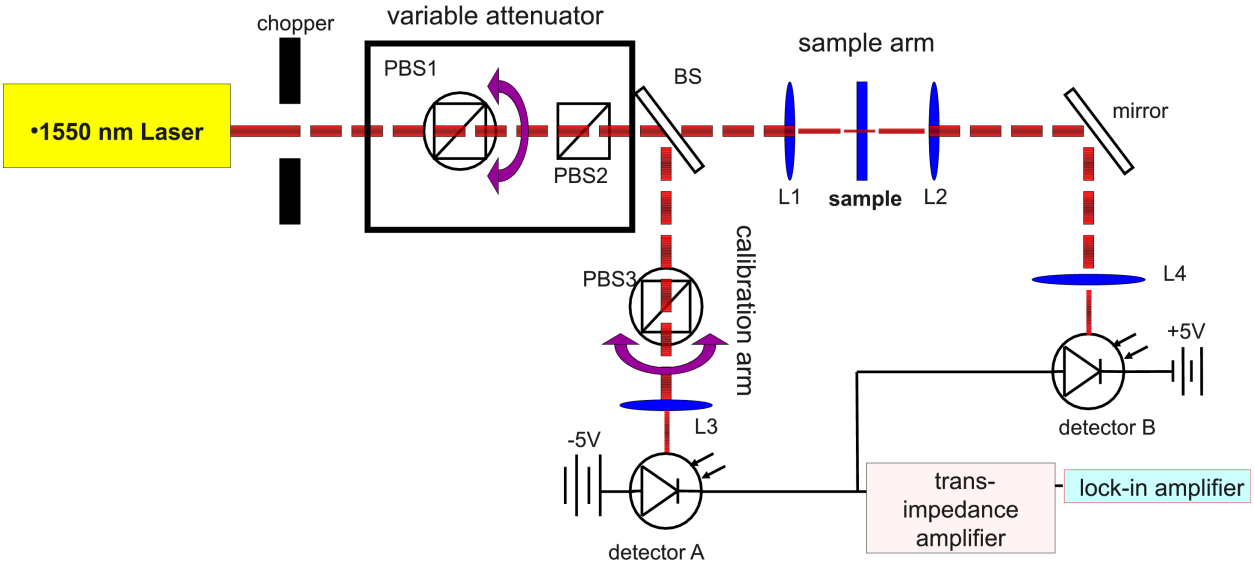

Figure 3.4: The differential transmission setup used to study graphene. PBS1 and PBS2: two polarization beam splitter cubes, used as a power attenuator. BS: beam splitter, a laser output coupler is used to reduce nonlinearity. Detector A and detector B: identical photodiodes for balanced detection. L1 and L2: focusing and recolumnating lenses respectively. Sample: graphene on a transparent substrate, usually a microscope slide. PBS3: polarization beam splitter cube used as a power attenuator for balancing. Chopper: mechanical chopper used with lock-in amplifier to reject part of the laser noise. Trans-impedance amplifier: amplifies electrically subtracted current output $A - B$ and converts it into a voltage signal. Image from [37].

relationship does not change over the dynamic range of the experimental system. An ultrafast pulse in a laser cavity may be as much as three orders of magnitude more intense than the ambient light in the cavity. To measure this behavior, the intensity to which the absorber is exposed must be varied over all three of these orders of magnitude. Unfortunately, it is difficult to control intensity accurately and continuously over such a large range, and it is more difficult to ensure that the intensity changes in the same way for both the sample beam and the calibration beam. The measure of how closely A and B reflect the desired relationship will be called the "linearity" of the system. Likewise, deviation from the desired behavior is called the "nonlinearity" of the system. These quantities can be measured by ensuring that $A - B = c$, where c is some constant, when the system measures a non-saturable absorber.

When no absorber at all is being measured, it is important that $A - B = 0$ so that $T = A/B = 1$. However, the sample beam passes through additional optical components, such as a pair of lenses to focus light onto the absorber sample and to recollimate the light after the absorber, the beam splitter likely splits

incident light into beams with unequal optical powers. To ensure that $A - B = 0$, then, a variable optical power attenuator must be placed in the path of the calibration beam, so that B can be adjusted. Adjusting B in this manner is called "balancing," and a system where $A - B = 0$ when there is no absorber in it is called "balanced." The less balanced a system is, the worse the nonlinearity and the noise will be. If the laser noise is stronger in one detector output than in the other, it will not be completely subtracted away and will appear in any resulting measurements.

3.3.2 Implementation

One common method to control the intensity is with polarization-dependent components, such as a half-wave plate and a polarization beam splitter (PBS), or a pair of PBSs. Polarization refers to the direction of the electric field vectors from the light waves [59]. Many optical effects such as refraction are dependent on polarization and lasers produce fairly uniformly polarized light, so it is possible to take advantage of polarization-dependent effects in optics. A half-wave plate rotates the polarization of light that passes through it without reducing intensity. It is called a half-wave plate to represent the angle required to rotate the polarization by 360°. A PBS splits incident light into two linearly polarized beams with orthogonal polarizations. The part of the incident light of one polarization is transmitted and the part with the orthogonal polarization is reflected at a 90° angle.

In the first configuration, the half-wave plate rotates incoming linearly polarized light to the same orientation as itself. The PBS then splits the beam according to its polarization so that the optical power at each output of the PBS is proportional to $P(\theta) = \cos^2(\theta)$, where θ is the relative angle between the polarization of the light (which is the same as that of the half-wave plate) and the PBS in radians. By using only one output from the PBS, one can continuously control intensity over up to three orders of magnitude. In the second configuration, the transmitted beam from each PBS is used. The first PBS acts as a polarization filter and takes the place of a half-wave plate with an additonal attenuation factor based on angle of rotation and the second PBS attenuates further and restores a uniform polarization in the system.

To ensure that A and B are the same to first order, the intensity to which the sample is exposed must be varied before the laser beam is split into the sample and calibration beams—although, as will be discussed

soon, being the same to first order is not enough to ensure linearity of the system. Unfortunately, most half-wave plates have a small wavelength dependence, and the more a wave-plate rotates the polarization of a light beam, the more severe this dependence becomes. This means that some parts of the spectrum of the laser beam are attenuated by the PBS after the half-wave plate and some parts are not. Because the beam splitter used to generate the calibration and sample beams is also wavelength dependent, this can generate large nonlinearity. For this reason, we used two PBSs rather than a half-wave plate and a PBS. Furthermore, to minimize nonlinearity due to the polarization dependence of components farther down the beam path, the second PBS must have an extremely high extinction ratio (100,000:1 in transmitted optical power); otherwise, the polarization in the system may not be uniform, and this non-uniformity would change as a function of the angle of the first PBS.

Because the intensity inside the system varies over 3 orders of magnitude, the heat of individual components varies wildly as well. At 1550 nm, no optical component is completely absorption free, and the energy of the absorbed light is converted into heat. This heat can stretch, bend, and warp the materials in an optical component, sending the system out of alignment as intensities increase. This effect is called "thermal lensing." For this reason, low-absorption components must be used whenever possible. High-reflectivity Bragg mirrors[6] must be used instead of silver-coated mirrors. Rather than using a beam splitter cube or a piece of glass at the Brewster angle,[7] the laser light is split into the calibration and sample beams by a laser output coupler at a shallow angle, which has a very well-defined ratio of reflected to transmitted light and reduces the thermal lensing effects and the angle dependence of the beam splitter that could influence the output power ratios.

We initially thought that variable attenuation could be accomplished by a piece of glass positioned slightly off of the Brewster angle to adjust loss and a set of neutral density (ND) filters, which are designed to attenuate light that passes through them by an extremely well-defined ratio independent of wavelength to a first-order approximation. However, the ND filters proved to absorb too much energy and to exhibit too much

[6] A Bragg mirror uses a stack of dielectric materials with different indexes of refraction to obtain extremely high reflectivities at normal incidence by taking advantage of constructive and destructive interference and the phase shift light undergoes when it passes through a dielectric interface. Bragg mirrors can obtain reflectivities as high as 99.99% and are used extensively in laser cavities to reduce loss.

[7] The Brewster angle is an angle different for every dielectric material. Light shone on the material at this angle will pass through with virtually no loss [59].

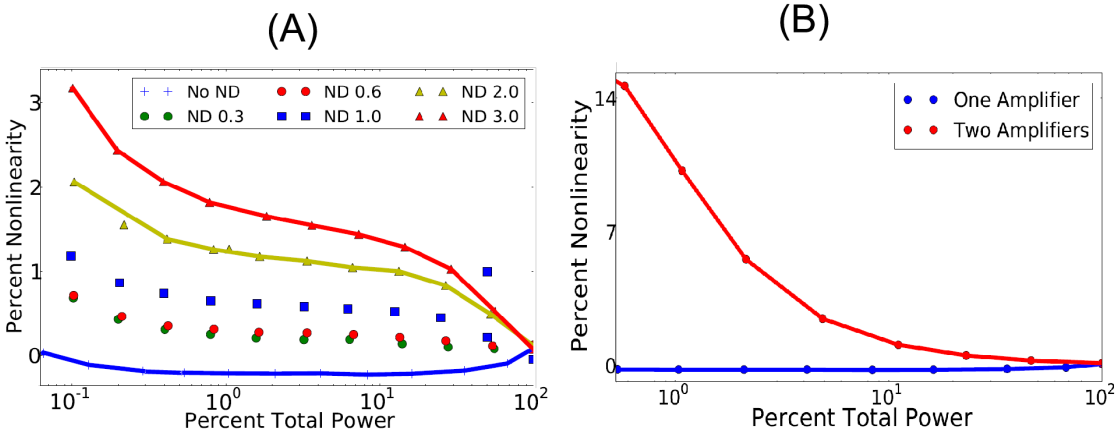

Figure 3.5: (A) The nonlinearity in differential transmission caused by absorptive components. ND x is an absorptive component that attenuates light to $\frac{1}{10^x}$ its original value. x-axis is intensity. y-axis is $1 - \frac{A-B}{A}$ for the system with no sample in it. (B) Comparison of nonlinearity of system that uses two trans-impedance amplifiers, one for each detector, to a system that uses one trans-impedance amplifier after signals have been electrically subtracted. x-axis is intensity. y-axis is $1 - \frac{A-B}{A}$ for the system with no sample in it. Dots are data points, lines are a spline for effect. Images from [37].

thermal lensing. Instead, another rotate-able PBS was used. If this PBS is aligned with the polarization of the incident light, there is no attenuation. As it is rotated to be orthogonal to the polarization of the incident light, more and more light is reflected such that, eventually, no light reaches detector A. This means that attenuated light is reflected out of the system, rather than absorbed and converted into heat.

Figure 3.5(A) shows the increased nonlinearity of a differential transmission setup as more absorptive components are added to the system. This is measured in a controlled way by adding absorptive ND filters to the calibration arm and re-balancing the system to compensate. The "ND rating" of an ND filter describes how much light the filter attenuates. An ND rating of 1, written "ND 1.0" reduces the transmitted light by a factor of 10, ND 2.0 reduces the transmitted light by a factor of 100, and so on. The formula for how much light is attenuated by an ND filter with ND rating ND x is thus

$$P_{transmitted} = \frac{1}{10^x} P_{incident},$$

where $P_{transmitted}$ is transmitted power and $P_{incident}$ is incident power.

Electronics also present a problem in linearity. The photodetectors at the end of each measurement

arm are photodiodes, which produce a small current in response to light. If the light shone on them is too intense, they themselves behave nonlinearly, so the light that hits them must be attenuated, reducing the current output further. To measure power accurately, it is convenient to convert the small current signal into a large voltage signal with a "trans-impedance amplifier," which converts current to voltage and amplifies the amplitude of the signal substantially. Initially, we thought that two identical trans-impedance amplifiers—one for each photodiode—would be sufficient. The difference between the outputs of the trans-impedance amplifiers could then be used to calculate $A - B$, and the output from detector A used to calculate A and the power at which T is measured. Even two supposedly identical amplifiers behave differently over such a large dynamic range, resulting in nonlinearity. Much better performance can be achieved by using a trans-impedance amplifier to amplify the *difference* between the current outputs of each photodiode, thus amplifying the signal $A(1+T) = A-B$. To attain A, one photodiode must be covered so that the difference is $A - 0 = A$. By using a single amplifier rather than two, any nonlinearity in the electronics affects both A and B equally, and $A - B$ remains unchanged. Figure 3.5(B) shows the difference in nonlinearity measured when two amplifiers are used and when one amplifier is used.

Unfortunately, the size of the laser spot on the surface of the photodetector changes the nonlinear behavior of that detector. This means that if the laser spot size on one detector is different from that of another detector, the two detectors will behave differently as a function of optical intensity. For this reason, the spots on each detector must be made as close to the same size as possible. Spot size can be controlled by changing the focal lengths of the lenses used to focus light on the photodetectors.

Even after all known systematic nonlinearities have been addressed, some nonlinearity can remain. To address it, a background "nonlinearity curve" is taken before measuring a sample, where $A - B$ is measured for every A value at which a sample will be measured. This curve is then crudely fitted by a spline and the spline subtracted from the raw $A - B$ values measured for the sample before calculating T. So long as these background curves are reproducible, this method reduces nonlinearity down to almost nothing. Measurements over many hours show these curves to be reproducible to well below 0.5%, making error negligible compared to variation over physical spots on a sample.

Figure 3.6 shows differential transmission measurements made on monolayer and bilayer graphene

grown at approximately 1 Torr pressure. The bilayer graphene is not lattice matched and thus behaves as if it were two monolayers stacked on top of each other. Solid lines show fits which approximate graphene as a slow saturable absorber. This is acceptable as an example since the overall shape of the curve does not change much in either approximation. Both $F_{sat,A}$ and $I_{sat,A}$ are listed for both monolayer and bilayer graphene. The monolayer graphene burns before it is fully saturated, due to the high optical intensities to which it is exposed, while the bilayer graphene exhibits greater resilience. These types of plots provide feedback for optimizing the growth and transfer process of graphene.

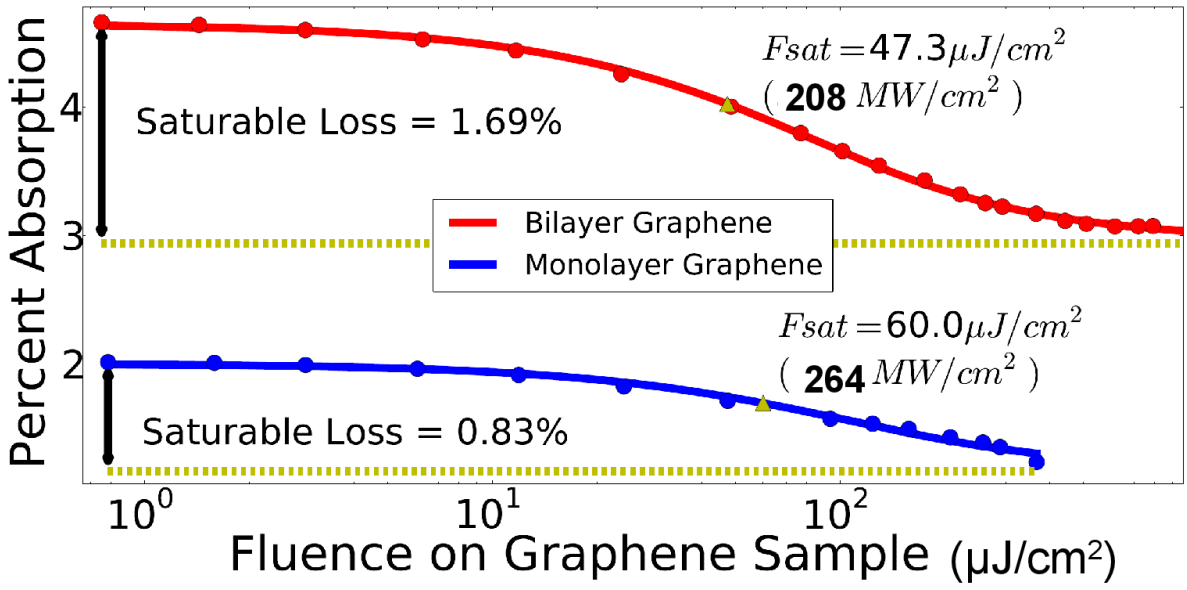

Figure 3.6: Differential transmission measurements comparing monolayer graphene to bilayer graphene. Solid lines are fits approximating graphene as a slow saturable absorber. Saturation fluence is labeled F_{sat} while saturation intensity is listed in parentheses. The monolayer curve stops before complete saturation because the sample is damaged due to high optical intensities. The bilayer graphene proves to be more resilient.

3.4 Time-Resolved Spectroscopy

Time-resolved spectroscopy, or pump-probe spectroscopy, is a method of measurement in which one first fires a high-intensity pulse of laser light at a sample, in order to excite the sample energetically so that it transmits more light, then fires a low-intensity pulse and measures the transmittance of the excited sample. By varying the time delay between the high-intensity and the low-intensity pulses, one can observe

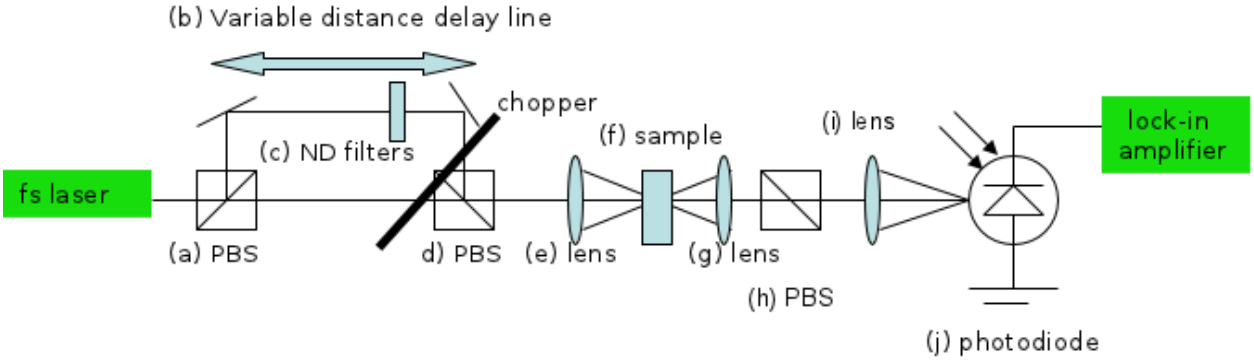

Figure 3.7: A time-resolved spectroscopy experiment used by Chien-Chung Lee. Light from a fs laser is split by a polarization beam splitter (a) into a stronger pump beam and a weaker probe beam. The probe passes through a variable distance delay line (b) which controls how much time will have passed between when the pump beam hits the sample and when the probe beam hits the sample. The probe beam is also attenuated with neutral density filters (c). Each beam, pump and probe, is chopped at a different frequency so that the lock-in amplifier can differentiate the two. The two beams are made collinear by another polarization beam splitter (d). They then pass through a focusing lens (e) into the sample (f), and into a re-collimating lens (g), after which the pump light must be filtered out through another PBS and (h) before the light is finally re-focused (i) onto a photodiode (j) which transmits all information to a lock-in amplifier.

the sample's capability to transmit light as a function of time—hence the name "time-resolved spectroscopy."

To produce these two pulses, time-resolved spectroscopy is usually performed with a single mode-locked laser operating at high intensity. To be certain of how much time has passed since the sample has been excited by the pump beam, one must know exactly when the pump beam hits the sample and exactly when the probe beam hits the sample, although one only needs to know the relative time between when the pump beam hits the sample and when the probe beam hits the sample. To get a resolution of roughly 100 femtoseconds, one needs a 100-fs laser. As Figure 3.7 shows, the laser light is split—either by reflecting it off of a glass slide or by the use of a PBS—and the stronger of the two beams is sent through the sample. Meanwhile, the weaker of the two beams bounces between several mirrors and passes through ND filters to attenuate it further and to delay it before it finally passes through the sample and into a photodetector. The two beams, pump and probe, are chopped at different frequencies, and the lock-in detects either the sum frequency or the difference frequency produced by the superposition of the two chopped beams. The amplitude of the probe beam can then be extracted. The delay line for the weaker beam is changed over time to accumulate a number of measurements, such that one can eventually build a picture of a saturable absorber saturating and then relaxing on a picosecond timescale (see figure 2.8).

Unfortunately, even with a high intensity mode-locked laser, time-resolved spectroscopy can be very difficult to perform. It is extraordinarily difficult to align powerful lenses so that they focus the laser light from both the pump beam and the probe beam onto the same spot on a sample. Because of this difficulty, one often has to settle for much lower intensities than might be desirable. Another issue is scattered light, which causes noise. The pump beam is much stronger than the probe beam, so if some light from the pump beam scatters off of the sample—and it will—it is focused by the collimating lens and follows the same beam path as the light from the probe beam at the detector, causing it to overwhelm any useful data. This is the reason that the two beams are chopped at different frequencies—to extract the signal from the coaxial beams. However, the light from the two beams also superimposes and causes constructive and destructive interference, which interferes with the signal. Differential chopping cannot prevent this effect; it can only be avoided if the frequency of one of the beams is shifted by some high-speed device (an AOM can do this). These factors make pump-probe spectroscopy more difficult than differential transmission.

Chapter 4

Optimizing Graphene Growth and Transfer Methods

4.1 A Brief Overview of Methods to Produce Graphene

Graphene can be produced by a number of methods. The first method to be discovered was the reduction of graphite oxide by heating it to high temperature [28].[1] Unfortunately, the yield is very low and the quality of the graphene flakes produced very poor. The first popular method to be discovered was "mechanical exfoliation," or the "scotch tape method," pioneered by Andre Geim and Konstantin Novoselov [29]. It involves pulling flakes off of highly-ordered graphite with tape, and then pulling those flakes apart repeatedly until flakes consisting of between one and ten layers of graphene sheet are achieved. The sheets are then placed on a substrate and the tape is removed [10, 29]. While this method produces high-quality graphene, it is extremely slow, does not reproducibly generate monolayer sheets, and is not scalable to large-area sheets. However, the scotch tape method is still popular because of how cheap it is for research purposes, where large quantities are not required, and because high-quality graphene can be achieved with very little optimization.

Another popular method is to heat silicon carbide (SiC) to high temperatures. The bonds between the silicon and the carbon atoms break, and graphene forms on top of the silicon-carbide crystal lattice [31, 60]. This method is called "epitaxial growth." Epitaxial growth is scalable to high quantities of graphene, and, most importantly, silicon carbide wafers are compatible with standard nanofabrication techniques used to make modern electronics. This makes epitaxial growth very attractive to those interested in making

[1] Technically, H.P. Boehm discoved graphene long before Geim and Novoselov, as early as 1962. However, the graphene produced by Boehm et al. was of very poor quality, and it did not exhibit any of the properties that graphene is famous for now.

graphene-based electronics. However, epitaxially-grown graphene usually has more defects in the lattice, resulting in lower conduction and poorer overall quality.

The method used in these experiments is "chemical vapor deposition" (CVD). CVD uses a transition metal—such as nickel [61], iridium [62], or copper [63]—to catalyze the high-temperature breakdown of a carbon-containing gas (such as methane) into carbon and the gas's other constituents. The carbon deposits on the metal as graphene and the rest of the gas constituents are blown away from the reaction. The metal substrate must then be etched away and the graphene deposited onto an arbitrary substrate. At ambient pressures using most transition metals, growth times must be chosen carefully to limit the number of graphene layers produced. However, when using copper at low pressures, when statistical mechanics begin to fail and Newtonian physics prevail, the CVD process on copper becomes self-limiting and produces nearly single-layer graphene sheets. Theoretical work on this topic was explored by Wenhua Zhang and colleagues [64], and a controlled experimental study was performed by Sreekar Bhaviripudi et al. [65].Because CVD requires only a sheet of transition metal, a furnace, maybe a vacuum pump, and some carbon-containing gas, it is reasonably cost-effective and extremely scalable. In 2010, Sukang Bae and his colleagues managed to produce meter-by-meter sheets of graphene using CVD on copper [11].

Unfortunately, CVD requires a large initial investment of time and money. Each CVD system is different, and growth involves a large number of variables that need to be optimized, including the partial pressures of gases used during growth, the total pressure of the reaction, the temperature of the reaction, the types of gases and transition metals used, and the pre-growth preparation of the metal to be used as a catalyst. The transfer method also has many parameters. What etchant should be used to remove the transition metal, and in what concentration? How should the graphene be cleaned? Can a monolayer survive a wet transfer process? Because of this uncertainty, it is necessary for each lab or company to optimize their own CVD process until commercially developed CVD systems are available. One goal of this research is to develop graphene for use as a saturable absorber by iteratively growing a sample, measuring it by differential transmission, and using the information gained to tweak the growth recipe. This chapter is about achieving that goal. Growth and transfer methods will be discussed in broad terms, followed by a discussion of various recipes arrived at in the optimization of the growth and transfer process.

4.2 Methods

Graphene was grown by CVD on copper foil (Alfa Aeser #13382, 25 μm) following the work by Li et al. [63]. The carbon-containing gas was methane. Hydrogen and argon gases were added to the mixture at various partial pressures. We flattened our copper catalysts between two clean glass slides and placed them in a reaction chamber. We attempted growths at ambient pressure, at approximately 10 Torr of pressure, and at approximately 10 mTorr of pressure. The temperature of growth was varied from approximately 850°C, where little to no growth occurred, to approximately 1030°C (Furnace: Thermo Scientific Lindberg Blue M). A small piece of copper/graphene was cut off for imaging by scanning electron microscope (SEM), and the rest was prepared for transfer by flattening a sheet of graphene/copper as much as possible and taping it to a microscope slide by the edges.

The transfer process reproduced another method established by Li et al. [66]. The copper was spin-coated with poly(methyl methacrylate) (PMMA)[2] to act as a temporary substrate during wet transfer so that the graphene sheet does not break apart under the mechanical stress. The copper foil was then etched by 0.5 M ferric chloride (Alfa Aesar), leaving graphene/PMMA floating on the surface of the etchant. The graphene/PMMA combination was then purified by prolonged soaking in de-ionized (DI) water, first of reactant grade and then of spectrograph grade—reactant grade and spectrograph grade are purities of deionized water: Spectrograph grade is the most pure, while reactant grade is the second most pure. Finally, the sample was placed on the desired final substrate, and the PMMA was washed off with organic solvent. For the solvent, different combinations of acetone, methanol, chloroform, and isopropyl alcohol (IPA) were experimented with. It was found that two baths of chloroform at 60°C ,interspersed by rinses in acetone and then methanol, followed by a bath in IPA at room temperature and a final rinse by acetone and methanol produced the best results. The final transfer method can be found in Appendix A.1.

The saturable absorption of the graphene sample was then measured by differential transmission. By looking at the SEM images of the sample, and by randomly measuring the linear absorption of many spots over the area of the sample using the differential transmission setup, it could be determined whether the

[2] PMMA is a transparent plastic often used in nanofabrication as a photoresist. It dissolves in organic solvents, but not in weak acid.

graphene sample was many flakes or a single large sheet. In the case of sheets, it is not difficult to measure graphene by differential transmission. In the case of flakes, the flake size as measured on the SEM roughly represents the single-crystal domain size of the graphene. Domain size means how large each single crystal formation is in a graphene sheet.

Ideally, large crystals of arbitrary size should be possible to produce. In practice, however, many crystal domains form. However, it can be difficult to locate a flake with diameter on the order of tens of microns to measure. By keeping the intensity constant in differential transmission, it is possible to sample the linear absorption of many spots on a graphene sample. Flakes can then be located and their nonlinear absorption measured by varying the intensity from 3 to over 3000 MW/cm^2. However, to avoid damaging samples with low damage threshold, intensities were only varied up to 1000 MW/cm^2. To increase prototyping speed, as few as 3 spots on a graphene sample would be measured, with between 2 and 4 samples produced per growth recipe. Because the intensity on the sample is automatically increased incrementally during a measurement, damage can be mistaken for saturable absorption, except that the absorption rises again as the intensity is reduced. For this reason, each spot was measured at least twice to ensure that damage did not give a false signal. Preliminary work on growth recipes was done by Chien-Chung Lee and Brian Benton. Later work was done by the author in collaboration with Chien-Chung Lee.

4.3 Recipe Case Studies

As shown in figure 4.1, the CVD process depends on a variety of parameters, each of which needs to be optimized. This section will describe, in loose narrative, the optimization process we went through to attain high-quality CVD graphene. It will emphasize a few notable steps in the process where we discovered a useful guiding principle or an especially good (or especially bad) recipe. The goal during this process was to develop a good recipe as quickly as possible. Unfortunately, because of graphene's relatively low damage threshold, it often burned before fully saturating, making curve-fitting difficult. Because of this, very little attention was paid to error analysis. We made educated guesses regarding the next recipe to try after observing the qualitative information gained from saturable absorption curves (up until damage), poor fits, and SEM images. Measurement variance was only calculated for samples used in later experiments.

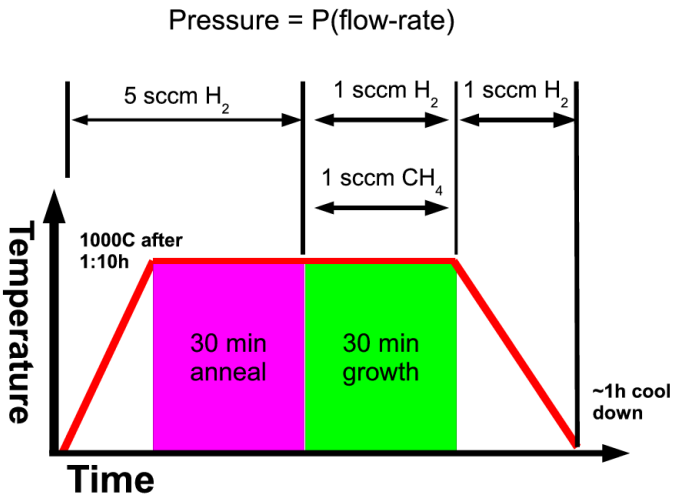

Figure 4.1: One of the recipes attempted during the optimization process. A large number of parameters had to be adjusted, including growth temperature, growth time, annealment time, and gas flow during each phase. Gas flow was especially important, as it determines total pressure and partial pressures.

Most of this work focused on reproducing the work of Xuesong Li and colleagues from [63, 66, 67, 68] in our own lab and applying it to optics.

Initially, growths were performed at ambient pressure and temperature. However, the graphene quality was extremely poor, and differential transmission measurements showed very little saturable absorption (although linear absorption was an integer multiple of approximately 1.9%, as expected). To more closely emulate Li et al., a roughing pump was used to lower the pressure in the reaction chamber to approximately 10 Torr. This low pressure drastically improved results. One high-quality growth recipe from this period of experimentation was the following:

The flattened copper foil was placed in the reaction chamber, and the pressure lowered to approximately 10 Torr. The chamber was then heated to 1000°C, which took approximately 1 hour and 10 minutes (1:10h). During the heat-up phase, 20 standard cubic centimeters per minute (sccm) of hydrogen gas flowed through the tube, raising the pressure marginally. After the target temperature was reached, the copper was allowed to anneal[3] in the 20 sccm hydrogen flow for approximately 30 minutes (30m). After annealing, the copper was exposed to 20 sccm of hydrogen and 35 sccm of methane for approximately 30m. This was the

[3] Annealment is a heat treatment that alters the properties of a material. In this case, the goal is to remove any adsorbants from the surface of the copper.

"growth phase" of the process. After the growth phase, the copper was allowed to cool to room temperature under the same gas flow as the growth phase. Cool-down took approximately 1h.

The purpose of annealing during growth was to remove any contaminant or oxidation layer that had accrued on the copper. The copper surface must be uncontaminated for continuous low-defect graphene. This annealing step remained in all recipes after initial trials; it is in current recipes as well. In this phase of experimentation, the following flow controllers were used:

- Hydrogen: MKS Mass-Flo model#14794A0722CR1BM, dynamic range 0–200 sccm.
- Argon: MKS Mass-Flo model#1479A0418CR1BM, dynamic range 0–1000 sccm.
- Methane: MKS Mass-Flow model#1479A02922CR1BM, dynamic range 0–200 sccm.

The sample shown in 4.2, had a large linear absorption, indicating multilayer graphene. This multilayer sample was likely produced by accidental folding during the wet transfer process. Only multilayer samples grown by this recipe had a high enough damage threshold to be accurately measurable or reliably used as saturable absorbers. However, multilayer graphene is undesirable because high linear absorption adds to the loss in a laser cavity, thus requiring more laser gain for the laser to operate. Most solid state gain mediums have low gain, so a high loss absorber is useless in solid state lasers, which often have the widest gain-bandwidth and thus generate the shortest pulses. Graphene grown in this regime also had a higher saturation fluence/intensity and a lower single-layer damage threshold than later samples.

We theorized that the high saturation fluence/intensity and low damage threshold might both be caused by the graphene sheet consisting of many small crystal domains. The domain boundary between two crystals traps charge and blocks conduction, perhaps changing the band structure and increasing the fluence/intensity required for saturation. Furthermore, it is possible that damage initially occurs at the edges of a crystal domain; and thus, the more domain boundaries there are, the lower the damage threshold. In another paper, Xuesong Li and his colleagues suggested that high pressure is the cause of small domain size and that the lower the pressure the reaction takes place in, the larger the graphene domains will be [67]. Li et al. also hypothesized that a high density of methane molecules in the reaction causes more methane to break down more quickly and in more places on the copper than a low density. This high break-down

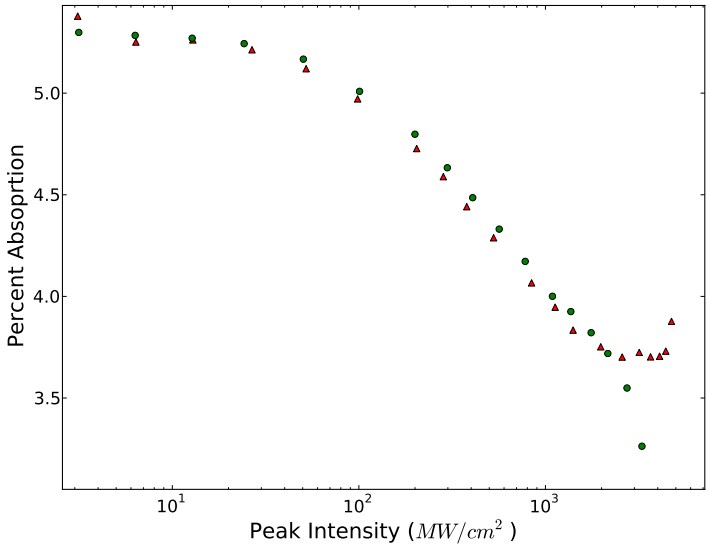

Figure 4.2: The saturable absorption of a recipe grown at approximately 10 Torr. Graphene plotted as a fast saturable absorber for simplicity. Red triangles are the first measurement, green circles are the second. Both measurements made on the same spot. The green curve does not saturate, indicating damage. The approximately 5 percent linear absorption indicates that the sample is at least bilayer graphene.

rate means that a graphene crystal has less room to grow before it encounters another crystal and must stop growing, resulting in a small domain size [67].

In order to grow graphene in the ultra-low pressure regime, a turbopump/roughing pump combination was acquired (Drytel 100-R), and a high-vacuum system constructed. This work was performed by Chien-Chung Lee and Professor Thomas Schibli. Figure 4.3 shows a photograph of the ultra-low pressure (ULP) CVD system. To enable more rapid cooling of a sample, the furnace was placed on a rail so that it could be moved away from the sample, allowing the sample to cool. New flow controllers had to be purchased because high flow rates increased pressure to unacceptably high levels and the resolution on the high-flow rate flow controllers was not good enough. The following flow controllers were used:

- Argon: MKS Mass-Flo model#1479A0722CR1BM, dynamic range 0–200 sccm.
- Hydrogen: MKS Mass-Flo model#1479A00711C51BM, dynamic range 0–10 sccm.
- Methane: MKS Mass-Flo model#1479A02811C51BM, dynamic range 0–10 sccm.

In addition, the following two flow controllers were used as bypass valves to prevent a buildup of pressure

behind the active flow controllers and to prevent gas leakage into the reaction chamber.

- Argon: MKS Mass-Flo model#1479A0418CR1BM, dynamic range 0–1000 sccm.
- Methane: MKS Mass-Flow model#1479A02922CR1BM, dynamic range 0–200 sccm.

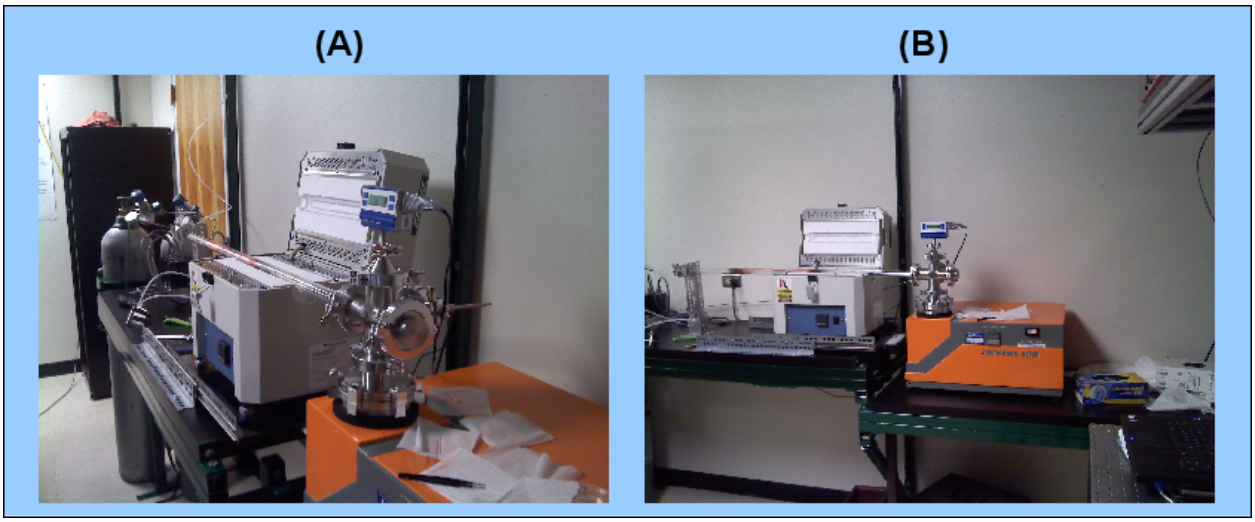

Figure 4.3: Ultra-low pressure vacuum system. (A) long view. (B) side view.

Graphene grown in the ultra-low pressure regime consists of disconnected graphene flakes with diameters greater than 10 μm and large micron-order gaps between the flakes. These gaps make many measurements difficult, since the graphene is not conductive across the entire sheet and it can be difficult and time-consuming to find a flake to make measurements on by differential transmission. In [68], Li et al. suggested that a two-step growth process could be used to produce a more connected graphene sheet. Li and colleagues suggested that there should first be a long growth phase with extremely low pressure in the reaction chamber and very small gas flow rates to produce large domain-size flakes, then a short second growth phase with a higher flow rate of methane (10 sccm compared to 1 sccm) to produce many very small domain size crystals to fill in the gaps. Ideally, this recipe should produce graphene of the same high quality as the single-step growth listed above, but the sheet will be more consistent. This recipe was adapted to our system and can be found in Appendix A.2.1.

As shown in Figure 4.4(B), the two-step process produces a near-uniform sheet of graphene, with domain boundaries barely visible. The inset shows graphene produced by a single-step ultra-low pressure

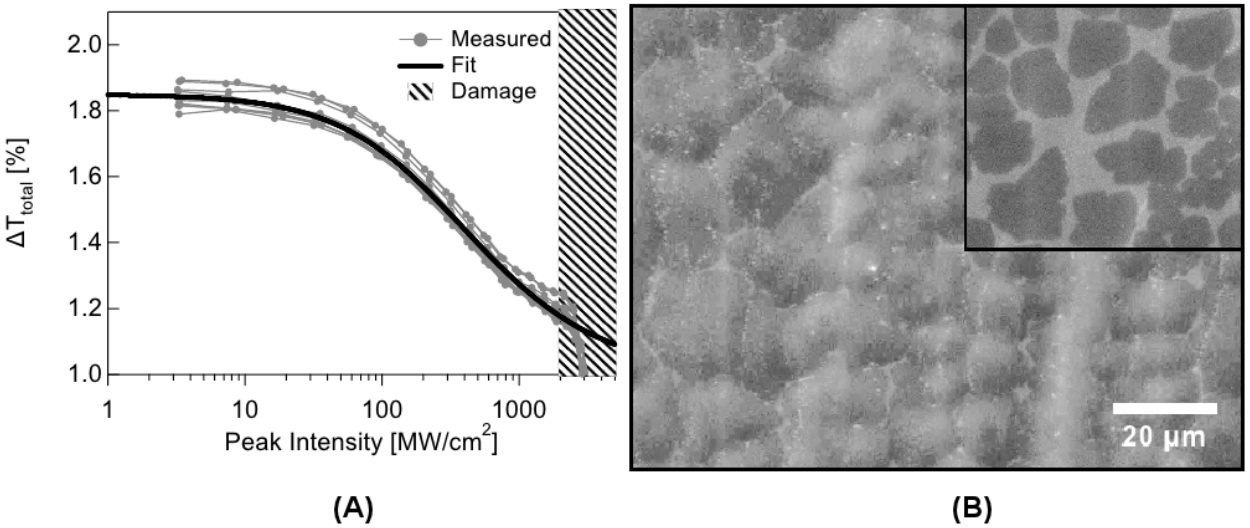

Figure 4.4: Samples grown using Li et al.'s recipes for ultra-low pressure graphene. (A) Differential transmission measurements of graphene approximated as a fast saturable absorber. Shaded region shows damage threshold. Grey curves are measurements and dark black curve is a fit. Measurements made in collaboration with Chien-Chung Lee. (B) SEM image of graphene sheet produced by two-step process. Inset: SEM image of graphene produced without the second growth phase to fill in the gaps between flakes, showing the approximate domain size of the primary graphene flakes (10 to 16 microns in diameter). Scale is the same for both images. SEM measurements made by Chien-Chung Lee.

growth. The crystal domain size for the large flakes should be the same for both growths, while there are regions in the sheet produced by the two-step growth that have much smaller grains between the large ones. The crystal domains for large grains range in size from 100 to 200 μm^2—which is substantially larger than the laser spot focused onto the sample, which is approximately 15 μm^2. However, in the case of the single-step growth, there are often gaps between flakes as large as 15 μm in diameter, which often makes finding a flake to measure by differential transmission difficult and the system inconsistent. Figure 4.4(A) shows typical differential transmission measurements of graphene produced by these two recipes. Both recipes produce graphene with the same properties as a saturable absorber, although the single-step process is less consistent. Grey curves are measured data, while the black curve is a fit over all data points. When the data diverges from the fit, the graphene has been damaged. Because of its high level of consistency, we still often use the two-step recipe.

Modeling this graphene as a fast saturable absorber, we found that the graphene produced by these recipes showed a linear absorption of $(1.85 \pm 0.08)\%$, a saturable loss of $(0.85 \pm 0.04)\%$, and a saturation

peak intensity of (250 ± 80) MW/cm^2. If it is modeled as a slow saturable absorber, the saturation fluence is found to be approximately 40 μJ/cm^2. The linear absorption is for graphene on a glass slide, and it is lower than the absorption for suspended graphene (2.3%) because the dielectric interface between air and glass mediated by the graphene sheet reduces this loss. Theoretical work on this topic was performed by Stauber et al., who first calculated the optical conductivity of graphene from first principles and then used this result to calculate the absorption for a graphene sheet placed on a dielectric-dielectric interface [32].

Because ultra-low pressure makes it much easier to grow high-quality monolayer graphene. The following question arises: In this regime, is it better to make the *total* pressure in the reaction chamber as low as possible, or is it better to make the *partial* pressure of methane gas as low as possible compared to that of the other gases in the chamber while still maintaining a nonzero flow rate? To answer this question, we performed growths where the total pressure in the reaction chamber during the growth phase was as low as possible (approximately 1 mTorr) and growths where the partial pressure of methane was as low as possible compared to that of hydrogen (we achieved a ratio of approximately 1:50). To attain the low total pressure, the flow rates of both hydrogen and methane were reduced to approximately 0.2 sccm during the growth phase and the copper was exposed to only 0.2 sccm of hydrogen during cool-down. To achieve a low partial pressure of methane compared to hydrogen, the methane flow rate was reduced to 0.2 sccm and the hydrogen flow rate increased to 10 sccm during the growth phase.

In both cases, these low flow-rate growths proved to be extremely inconsistent compared to the growth recipes outlined above. This inconsistency could be attributed to a number of factors. First, the flow controllers used are only reliable to about $1/50^{th}$ of their dynamic range—i.e., 0.2 sccm, the flow rates used in these growths. It is thus possible that gas did not flow for the entirety of the growth process. It is also possible that over the long times required for the growth, the sublimation of the copper substrate caused inconsistency. At such low pressures and high temperatures, the copper substrate slowly sublimates into the vacuum around it in the reaction chamber. In the total 3:10h that a high flow-rate growth occurs in, this sublimation is probably irrelevant. However, in the 6h or more that a low flow-rate growth might take, it can make a nontrivial contribution to the growth process. In fact, we found that the flake size for low flow-rate growths is self-limiting. We never observed a graphene flake with diameter larger than 150

μm, even when there was ample room for the flakes to grow and when the sample was exposed to methane at 1000 C for over 4 hours. We hypothesize that this self-limiting behavior might be caused by "elevated terraces" that appear on the copper foil. During growth, the growing graphene flakes might protect the copper underneath them from sublimation, while the exposed copper foil slowly sublimates. Eventually, the vertical gap between the area covered by the graphene flakes and the uncovered copper might become wide enough that a single crystal domain cannot grow across this gap.

Graphene samples grown at the lowest possible total pressure were never observed to be superior in saturation intensity/fluence or damage threshold to graphene grown by the one-step process detailed above, and they were often substantially worse. Graphene samples grown by reducing the partial pressure of methane were observed to be comparable or superior to the graphene grown by the one-step and two-step processes above approximately once out of every three growths. The poor growths, however, were very poor. The recipe used can be found in Appendix A.2.2.

As shown in Figure 4.5, this recipe produced widely varying domain sizes for the same growth parameters, although the saturation fluence/intensity was not much affected by domain size. The crystal domain size ranged from approximately 25 μm in diameter for an average sample—notably larger than the domains for the other growths outlined in this chapter—to approximately 120 μm in diameter for the very best sample measured. Saturation intensity was found to be (241 ± 12.0) MW/cm^2, and if graphene was modeled as a slow saturable absorber, saturation fluence was found to be (57.7 ± 2.90) μJ/cm^2. Saturable loss was found to be $(0.66 \pm 0.01)\%$ and non-saturable loss was found to be $(1.11 \pm 0.08)\%$. While the saturation fluence/intensity and linear and nonlinear absorption of the samples did not vary greatly with increasing domain size, the damage threshold did. The average sample shown in Figures 4.5(A1) and (A2) damaged at approximately 1 GW/cm^2, which is comparable to the samples discussed above. However, the damage threshold of the best sample measured, shown in Figures 4.5(B1) and (B2), could not be determined because our laser could not produce an intense enough pulse.

Overall, we found two recipes that produce high quality graphene. The two-step growth process first proposed by Li et al. [68] produces relatively lower quality graphene but it is highly reproducible; on the other hand, the extremely low partial-pressure process produces relatively higher quality graphene, but it is

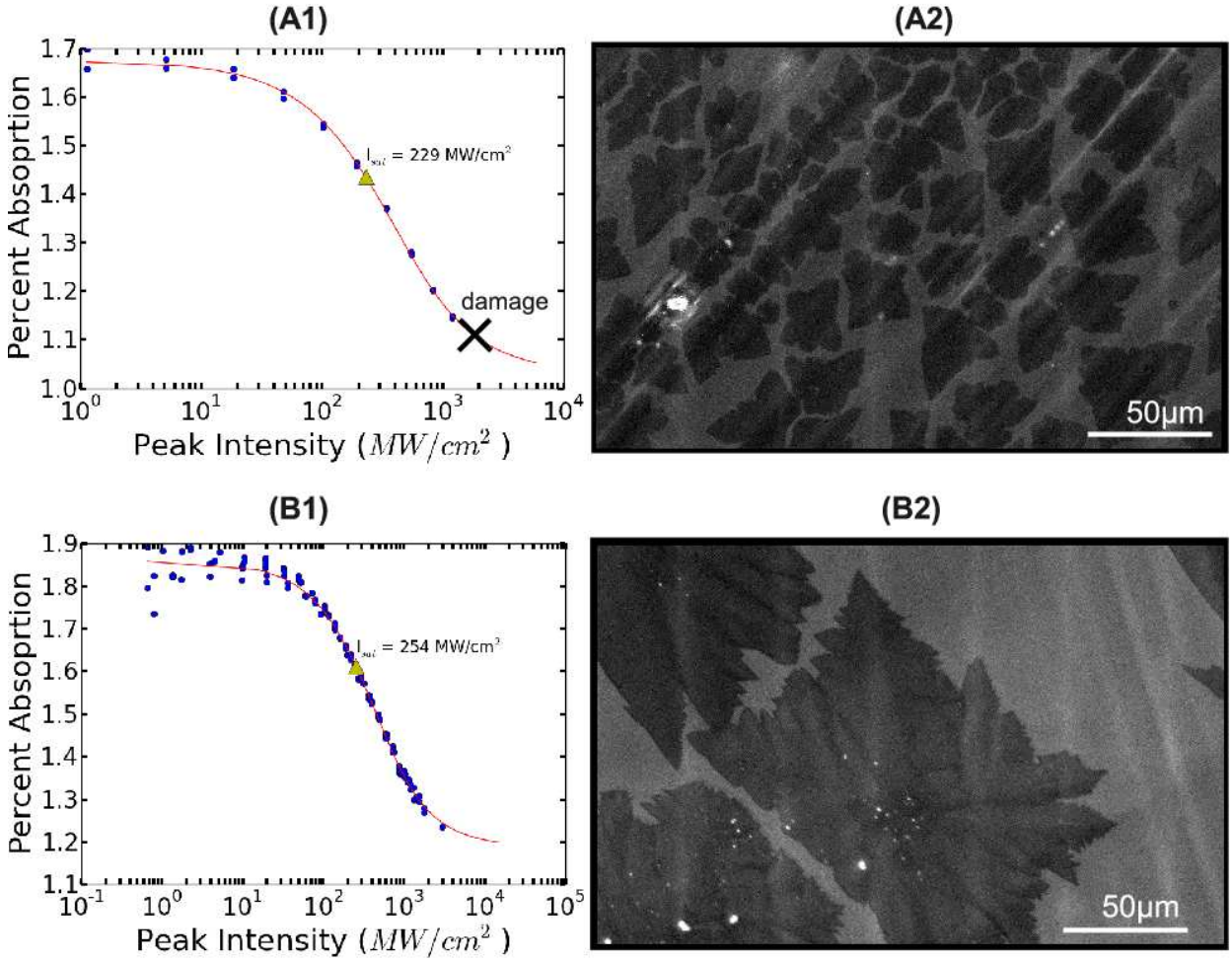

Figure 4.5: Samples grown by ultra-low pressure CVD such that the partial pressure of methane compared to hydrogen was as low as possible. (A) An average sample grown using this recipe. (A1) Differential transmission measurements made for an average sample. Dots are data, solid line is a fit with graphene modeled as a fast saturable absorber. (A2) SEM image for an average sample grown using this recipe. Average domain size is approximately 25 μm in diameter. Image taken by Chien-Chung Lee. (B1) Differential transmission measurements for the most durable sample produced by this recipe. Dots are data, solid line is a fit with graphene modeled as a fast saturable absorber. Damage threshold could not be measured because peak intensity could not be made high enough. (B2) SEM image for the most durable sample grown using this recipe. Average domain size is approximately 120 μm in diameter. This is the largest domain size we have produced to date. Measurement taken by Chien-Chung Lee.

substantially less reproducible. The large domain-size, low partial-pressure growth recipe was later used to generate suspended graphene (not discussed here), while the more reproducible two-step process was used to study ways to tune graphene's optical properties, discussed in the remaining chapters. F.T. Vasko calculated that, for light approximately 1.5 μm in wavelength, the peak intensity of a pulse must be approximately 60 MW/cm^2 [40]. Taking into account the dependence of saturation intensity on pulse width, our values, (250

$\pm$ 80)MW/cm^2, agree with Vasko's calculations within roughly a factor of 4. A higher saturation intensity implies a shorter time required for electrons to decay from the conduction band to the valence band. This might be caused by graphene's interaction with the substrate—a very strong effect, since graphene is only two-dimensional—or by defects in the graphene lattice. The discrepancy might also be due to fitting error. We assumed a fast saturable absorber for our fits, which is an approximation (see section 2.3.1).

4.4 Optical Damage

Unfortunately, while the graphene we produced has a saturation intensity/fluence comparable with most semiconductor saturable absorber mirrors (SESAMs), a satisfactorily low non-saturable loss, and acceptably large modulation depth,[4] full saturation is usually impeded by the onset of permanent damage around 2 GW/cm^2. (Operating below damage threshold then results in unsatisfactorily high insertion loss[5] and low modulation depth.) We hypothesized that this damage occurs due to the peak intensity of a laser pulse, rather than from the average power of the beam. We tested and confirmed this hypothesis by observing the damage properties of the graphene under radiation from a mode-locked laser and from the same laser operating in the CW regime. We kept the average power the same in both cases, but only observed damage when the laser was mode-locked and the peak intensity was thus 50,000 times greater.

To better understand this process, we measured the damage threshold of the graphene in an argon atmosphere, and found it unchanged. This implies that the cause of damage is not oxidation or "burning." Rather, it is likely due to an interaction between the graphene and residual contaminants or between the graphene and the substrate, enabled by the extremely large electric fields from the laser pulse. Further steps to examine this process might include generating purer graphene in some way, measuring the damage properties of suspended graphene, and measuring the damage properties of graphene on different substrates. Preliminary steps have been made in all of these directions, but, no reliable conclusions have yet been drawn.

[4] Modulation depth is the difference between linear absorption and non-saturable loss.
[5] Insertion loss is the amount of loss observed when the absorber is as saturated as it will get in the laser cavity.

Chapter 5

Characterization of Doped Graphene

5.1 Doping and State Blocking

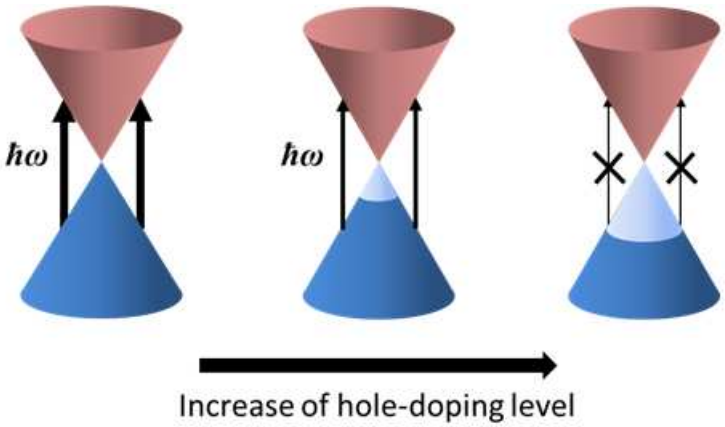

Figure 5.1: State blocking due to hole-doping in graphene as viewed near the Dirac point. Red cone is the conduction band. Blue cone is the valence band. Dark blue represents states occupied by electrons, while light blue represents states occupied by holes. As the Fermi level decreases, fewer electrons are in the proper energy level ($E = -\hbar\omega/2$) for excitation. Eventually, no electrons remain with energy greater than or equal to $\hbar\omega/2$, and absorption ceases. An analogous picture can be formed for electron doping. Image by Prof. Thomas Schibli.

One of the great advantages of SESAMs is that the optical properties of an individual SESAM can be adjusted during production. Relaxation time, linear absorption, and saturable loss can all be tuned to meet design specifications for a variety of laser systems. For graphene-based saturable absorbers to compete with SESAMs, they too must be tunable during production. One possible way to adjust the optical properties of a semiconductor is to adjust its Fermi level. As shown in Figure 5.1, one can block absorption by shifting graphene from the insulating phase to either the electron or hole conducting phase so that, for a given photon

energy, no electrons can be excited from the valence band into the conduction band—either because there are no electrons in the valence band at the required energy to excite, or because there are no open states at the required energy in the conduction band for the excited electrons to enter. This is called "state blocking."

The question then arises: how does one change the Fermi level in a material? The answer is that one must immobilize charge in the material, effectively removing charge carriers from the band structure. Charge carriers can be immobilized by adding stationary charges to the material, which attract the carriers of the opposite charge to them. This is called "doping." Figure 5.2 shows the doping of a bulk semiconductor by a strong acid. The H^+ ions in the acid contact the material and attract electrons to the surface of the semiconductor. The electrons in the semiconductor then form dipoles with the H^+ ions. The number of charge-carriers is thus reduced, and the Fermi level decreases. Because charge-carrying *electrons* are removed, this is called "hole-doping" or "p-doping." If *holes* are immobilized, rather than electrons, the process is called "electron-doping" or "n-doping." An analogous process can occur in graphene, although it is much more difficult to illustrate because of the two-dimensional nature of the material.

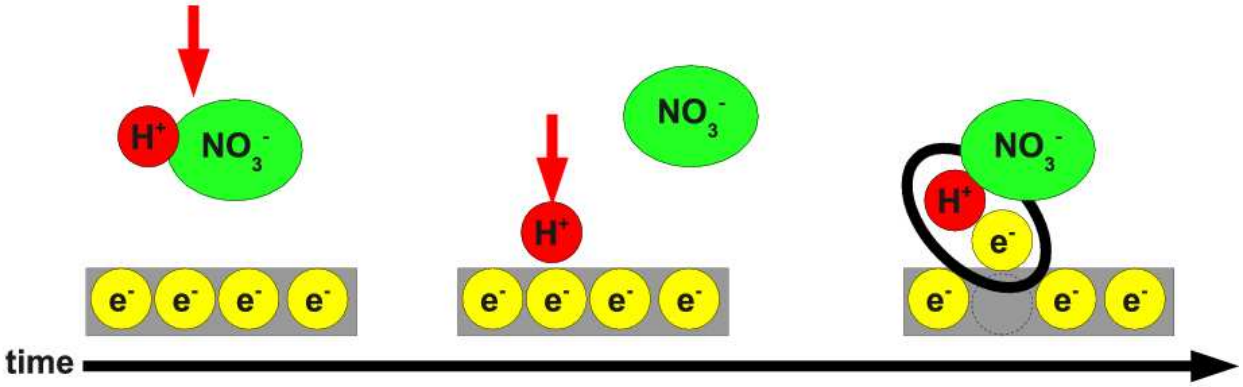

Figure 5.2: Hole-doping of graphene by a strong acid. First, the H^+ cations (red) and their associated anions (green) dissociate in water. The cations attach themselves to the material, attracting electrons (yellow) from inside the bulk (grey). The electrons then form dipoles with the H^+ ions, leaving holes behind in the material and lowering the Fermi level. The holes can then move through the material, carrying positive charge.

Because fewer electrons in the valence band means a lower probability of an individual electron being excited into the conduction band, absorption decreases continuously as the Fermi level shifts away from the K point, even when state blocking has not yet taken full effect. This provides a tool for continuously tuning the optical absorption of graphene during production. Because state blocking affects all photons with energy

less than twice the difference between the K point and the Fermi level, doped graphene no longer has a constant linear absorption. The absorption spectrum of doped graphene can then be used to determine the Fermi level.

This chapter will discuss our characterization of this process using nitric acid as a dopant. We doped graphene with various concentrations of nitric acid and determined the Fermi level by fitting to the transmission spectrum measured by spectrophotometry, which measures the transmission spectrum of a material $T(\omega)$. We then measured the nonlinear absorption of the samples by differential transmission and correlated it to Fermi level. The bulk of this work was done by Chien-Chung Lee. To confirm that the nitric acid was indeed doping the graphene as expected, we also studied the Raman spectrum of pristine and doped graphene, discussed below. Raman spectroscopy is a proven tool for studying graphene and there is an enormous body of literature discussing the Raman spectrum of graphene, which is now well understood. We drew on this body of knowledge to characterize our own graphene and confirm that the behavior we observed in spectrophotometry and differential transmission was due to doping. The bulk of Raman spectroscopy work was done by the author.

In this chapter, spectrophotometry will first be discussed in slightly more detail, and the results of differential transmission measurements on doped graphene will be discussed. This will be followed by a detailed discussion of Raman spectroscopy, starting with a highly abridged theoretical analysis of Raman scattering in general. Then, previous work on the Raman spectrum of graphene will be summarized, with an emphasis on studies relevant to the doping of graphene. Finally, results of our own study will be discussed and analyzed.

5.2 Spectrophotometry and Differential Transmisson of Doped Graphene

5.2.1 Spectrophotometry

All work on spectrophotometry was done by Chien-Chung Lee and Linna Cooley. The following theoretical treatment was adapted from work done by T. Stauber and colleagues [32]. The transmission spectrum of doped graphene strongly depends on the optical conductivity (σ) as a function of Fermi level,

μ, frequency of incident light (ω), and temperature ($\mathcal{T}$). derived by Stauber et al. [32]:

$$\sigma = \frac{\sigma_0}{2}\left[\tanh\left(\frac{\hbar\omega + 2\mu}{4k_B T}\right) + \tanh\left(\frac{\hbar\omega - 2\mu}{4k_B \mathcal{T}}\right)\right], \tag{5.1}$$

where σ_0 is the optical conductivity of pristine graphene ($\mu = 0$), k_B is Boltzmann's constant, e is the charge of an electron, and $\hbar$ is the reduced Planck's constant, $h/2\pi$. At normal incidence, the transmittance (T) of a graphene sample placed at the interface between two dielectric materials with indexes of refraction n_1 and n_2 is then [32]:

$$T = \frac{4n_1 n_2}{\left(n_1 + n_2 + \dfrac{\sigma}{c\varepsilon_0}\right)^2}, \tag{5.2}$$

where ε_0 is the permittivity of free space and c is the speed of light in vacuum. This can be Taylor expanded to give

$$T \approx T_0\left[1 - \frac{s\sigma}{c\epsilon_0(n_1 + n_2)}\right] \tag{5.3}$$

where T_0 is the transmittance at the same interface without graphene:

$$T_0 = \frac{4n_1 n_2}{(n_1 + n_2)^2}. \tag{5.4}$$

In the case of an interface between air ($n = 1$) and glass ($n = 2$), $T_0 = 0.96$. With some algebra, one finds that the change in transmittance due to the presence of graphene on a glass slide (including both interfaces of the slide) is

$$\Delta T_{total} = |TT_0 - T_0^2| = \frac{2\sigma T_0^2}{c\varepsilon_0(n_1 + n_2)}. \tag{5.5}$$

The Fermi level can be found by measuring $T(\omega)$ with spectrophotometry and then fitting equations 5.5 and 5.1 to the measured spectrum. The concentration of dopants on the graphene surface is likely a spatially-dependent random distribution. In other words, the concentration of H^+ ions ρ_{H^+} at some coordinates (x_0, y_0) might be different than the concentration at some other coordinates (x_1, y_1), where ρ_{H^+} depends on some undetermined random variable. Assuming that ρ_{H^+} is symmetric around its mean $E[\rho_{H^+}]$, we can compensate for this nonuniformity by allowing the temperature in the fit function, $\mathcal{T}$, to represent

an effective temperature rather than the physical temperature of the electron gas[1] in the material. This effective temperature is then an added degree of freedom in the fit. In our fits, the effective temperature ranged from about 3000K to about 5000K.

Figure 5.3(A) shows the transmission spectrum of graphene hole-doped to various Fermi levels by immersion in nitric acid as measured by spectrophotometry. The Fermi level is positively correlated with the nitric acid concentration. Although the exact increase is not reproducible with nitric acid, the trend is. It is likely that if another dopant is chosen, the behavior could be made to be quantifiably reproducible.

5.2.2 Differential Transmission

Figure 5.3(B) shows differential transmission curves of the same samples shown in 5.3(A). The linear absorption decreases significantly with increasing doping concentration (and thus with increasing Fermi level) while the non-saturable loss decreases only slightly. This implies that the modulation depth of a given absorber can be tuned with the Fermi level. The fact that the non-saturable loss does not increase with increased doping concentration is an indication that the graphene lattice is not damaged by exposure to nitric acid.

5.3 Raman Spectroscopy

To further understand the effects of nitric acid on graphene, and to confirm that we were reversibly doping our graphene, we measured the Raman spectra of graphene samples doped to various Fermi levels and by various concentrations of nitric acid. Raman spectroscopy is an extremely powerful tool for the study of condensed matter systems, especially organic molecules. It takes advantage of Raman scattering, named after its discoverer Sir Chandrasekhar Venkata Raman [69], which is the inelastic scattering of light off of a material. This is in contrast to Rayleigh scattering (named after its discoverer Lord Rayleigh), which is elastic. In Rayleigh scattering, light scatters off of a material with the same wavelength as it had before it hit. In contrast, in Raman scattering, the scattered light can have either a longer or a shorter wavelength

[1] The behavior of electrons in a material can be modeled by treating all electrons as particles in a "Fermi gas,"—a construct similar to a classical gas, with the added complications that the electrons are delocalized in the material and that no two electrons can exist in the same state, since they are fermions.

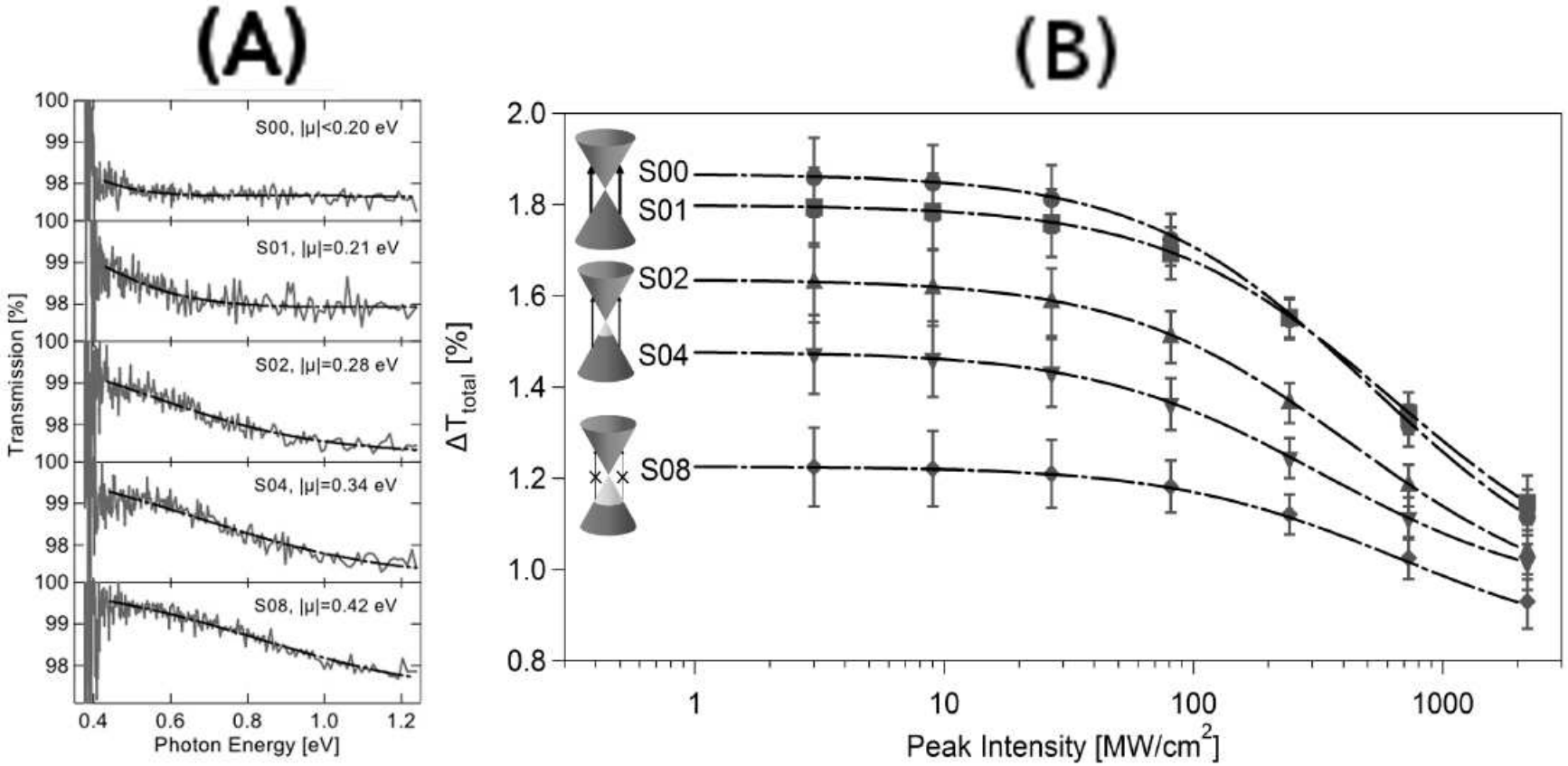

Figure 5.3: The tunable optical properties of graphene. Here $|\mu|$ represents the Fermi level. S00, S01, S02, S04, and S08 represent different samples on glass slides. In order from top to bottom: S00 is baked graphene. S01 is graphene baked and doped by 0.1wt% nitric acid. S02 is graphene baked and doped by 0.2wt% nitric acid. S04 is graphene baked and doped by 0.4wt% nitric acid. S08 is graphene baked and doped by 0.8wt% nitric acid. (A) The transmission spectrum measured by spectrophotometry of graphene hole-doped to various Fermi-levels by nitric acid. x-axis is photon energy, y-axis is transmission. Light grey curve is data, black line is fit. As doping concentration is increased, transmission increases and becomes more non-uniform as a function of wavelength. (B) Differential transmission measurements of graphene p-doped to various Fermi levels by nitric acid. Points with error bars are averaged data, lines are fits. The three cones show the band structure of graphene at different doping levels. Upper cone: conduction band. Dark lower cone: electron-filled valence band. Light-colored area: hole-occupied states. Figures made by Chien-Chung Lee.

than the incident light. Raman scattering is a much weaker effect than Rayleigh scattering, and one must filter out all Rayleigh-scattered light to observe the Raman-scattered light off of a material.

5.3.1 Theory of Raman Scattering

The following semiclassical treatment of the theory of Raman spectroscopy is covered in some depth and expanded upon by John R. Ferraro et al. [70]. In section 2.2, the structure of the electron energy levels in a condensed matter material was developed. However, this treatment neglected the fact that complex molecules vibrate.[2]

5.3.1.1 The Classical Theory

Consider the classical picture of a vibrating polar molecule. For simplicity, the molecule will contain only three atoms, as shown in Figure 5.4.

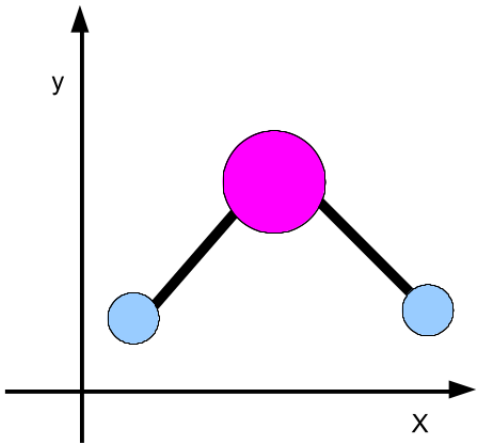

Figure 5.4: A toy model of a molecule. Purple represents one sign of charge when the molecule becomes polarized, while blue represents the other.

This molecule is undergoing simple harmonic motion, which obeys Hooke's law. There is then an equilibrium position for the "spring" that acts as the resistive force and tries to hold the charge clouds in the atom a specific distance away from each other. Define the parameter r as the distance of the centers of charge—i.e., the poles of a polar molecule, and this molecule will become polar momentarily—from the

[2] As a first-order approximation, the atomic nuclei in a molecule do not vibrate; rather the electron clouds carrying charge vibrate. For simplicity, however, this distinction will be ignored.

equilibrium position, as shown in Figure 5.5. In the Figure, r_0 is some constant nonzero value. However, in a moment, it will be defined as the amplitude of harmonic oscillation, set by initial conditions.

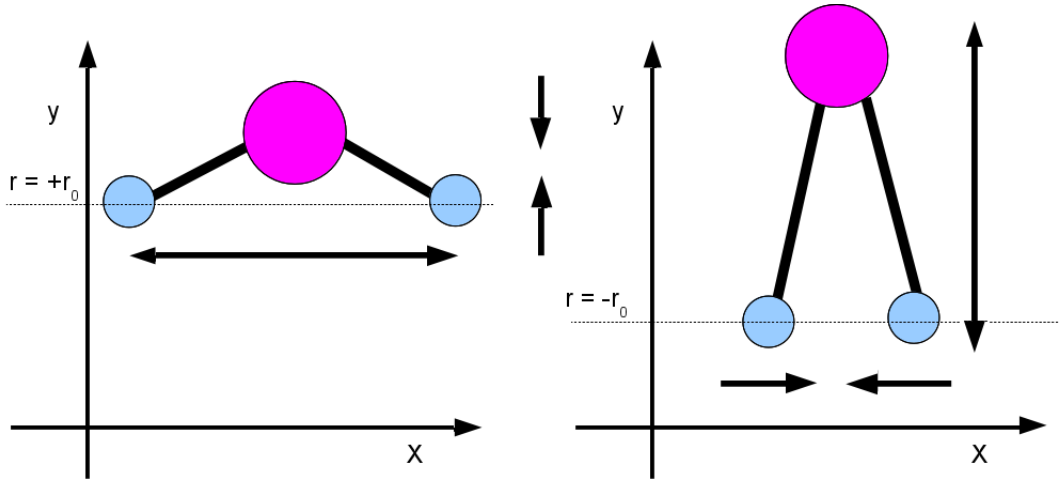

Figure 5.5: Definition of a coordinate system for classical Raman scattering. r is the distance of the poles from the equilibrium position for the "spring" that tries to hold the poles a specific distance away from each other. In this case r_0 is some constant nonzero value. It is important to note that this picture is a simplistic model. To first order, the bonds of the molecule do not actually shift; rather, the electron clouds move.

Hooke's law then reads

$$m_r \frac{d^2 r}{dt^2} = -k_s r, \tag{5.6}$$

where k_s is the spring constant, determined by the attractive force between the two poles of the molecule (not discussed here), and m_r is the reduced mass for the two charge clouds of masses m_1 and m_2:

$$m_r = \frac{m_1 m_2}{m_1 + m_2}. \tag{5.7}$$

The solution space to Hooke's law is sinusoidal, and all solutions are of the form

$$r(t) = r_0 \cos(\nu_m s t - \phi_s) \quad \texttt{where} \quad \nu_m = \sqrt{\frac{k_s}{m_r}}. \tag{5.8}$$

r_0 and ϕ_s are constants determined by initial conditions. Later, it will be important that this implies that the oscillating charges have a constant total energy, which is the sum of the kinetic energy (KE) and the

potential energy (PE) of the system:

$$\begin{aligned} E_{tot} &= KE + PE = \frac{1}{2}m_r\left(\frac{d}{dt}r(t)\right)^2 - \int(-k_s r(t))dr \\ &= \frac{1}{2}m_r r_0^2\nu_m^2\sin^2(\nu_m t - \phi_s) + \frac{1}{2}k_s r_0^2\cos^2(\nu_m t - \phi_s) \\ &= \frac{1}{2}m_r\frac{k_s}{m_r}r_0^2\sin^2(\nu_m t - \phi_s) + \frac{1}{2}k_s r_0^2\cos^2(\nu_m t - \phi_s) \\ &= \frac{1}{2}k_s r_0^2\left[\sin^2(\nu_m t - \phi) + \cos^2(\nu_m t - \phi)\right] \\ &= \frac{1}{2}k_s r_0^2. \end{aligned} \tag{5.9}$$

Now consider the same molecule irradiated by a beam of monochromatic light. For simplicity, this is a plane wave of frequency ν_0. At a single position in space, the electric field of this light wave can be described as

$$E = E_0\cos\left(2\pi\nu_0 t\right), \tag{5.10}$$

where E_0 is the amplitude of the wave, t is time, and ν_0 is the frequency of the light. To first order, the magnetic field can be neglected because the amplitude is $B_0 = E_0/c$, where c is the speed of light. This radiation induces an oscillating dipole in the molecule, in addition to the oscillations already occurring. The induced dipole moment[3] (P) of the molecule then follows harmonic motion at a different frequency:

$$P = \alpha E_0\cos(2\pi\nu_0 t), \tag{5.11}$$

where α is the "polarizability" of the molecule. Intuitively, the polarizability represents how easy it is to induce a dipole moment in the molecule, since in a linear dielectric material, the dipole moment (or polarization) is defined as $P = \alpha E$. Thus, in this case, we are implicitly assuming the molecule is a linear dielectric.

This oscillating dipole moment does not account for the implicit vibration of the molecule discussed earlier. To account for it, assume the vibration is small and Taylor expand α as a function of $r(t)$:

$$\alpha = \alpha_0 + \left(\frac{\partial\alpha}{\partial r}\right)_0 r + ..., \tag{5.12}$$

where α_0 is the polarizability for the molecule at the equilibrium position $r = 0$ and $\left(\frac{\partial\alpha}{\partial r}\right)_0$ is the rate of change of α with respect to a change in r, evaluated at $r = 0$. Now substitute equation 5.12 into equation

[3] The dipole moment of a material is the electric field caused by the dipole of the material. It has units of volts/meter.

5.11:

$$\begin{aligned} P &= \alpha E_0 \cos(2\pi\nu_0 t) \\ &= \alpha_0 E_0 \cos(2\pi\nu_0 t) + \left(\frac{d\alpha}{dr}\right)_0 r E_0 \cos(2\pi\nu_0 t) \\ &= \alpha_0 E_0 \cos(2\pi\nu_0 t) + \left(\frac{d\alpha}{dr}\right)_0 r_0 E_0 \cos(2\pi\nu_0 t)\cos(2\pi\nu_m t) \\ &= \alpha_0 E_0 \cos(2\pi\nu_0 t) + \left(\frac{d\alpha}{dr}\right)_0 r_0 E_0 \left[\cos\left((2\pi(\nu_0+\nu_m)t\right) + \cos\left(2\pi(\nu_0-\nu_m)t\right)\right]. \end{aligned} \tag{5.13}$$

The result is three superimposed oscillations in the dipole: (1) one oscillating at the original frequency of the perturbing radiation ν_0, (2) one oscillating at the sum frequency of the perturbing light and the vibrations of the unperturbed molecule $\nu_0+\nu_m$, and (3) one oscillating at the difference frequency between the perturbing light and the unperturbed molecule $\nu_0-\nu_m$. An oscillating dipole radiates energy, so new light is emitted by the molecule at all three of these frequencies. The emitted light that is the same frequency as the perturbing radiation is "Rayleigh-scattered" light. The emitted light of the other two frequencies is "Raman-scattered," and it comes in two varieties. The difference-frequency scattering produces light that is lower energy than the incident light,[4] and it is called "Stokes scattering." The sum-frequency scattering produces light that is higher energy than the incident light, and it is called "anti-Stokes scattering."

It is important to note that not every molecular vibration (called a "vibrational mode") results in Raman scattering. For a mode to contribute to Raman scattering,

$$\left(\frac{d\alpha}{dr}\right)_0 \neq 0. \tag{5.14}$$

In other words, the change in polarizability at the equilibrium position must be nonzero. Modes that contribute to Raman scattering are called "Raman-active" modes, while modes that do not are called "Raman-inactive" or "IR-active." This is because IR-active modes cause the molecule to absorb light in the infrared spectrum, allowing for IR-active modes to be observed using infrared (IR) spectroscopy, which is considered a complementary technique to Raman spectroscopy. Figure 5.6 shows the difference between Raman-active and IR-active modes. The diagrams showing how the molecule moves are associated with plots $\alpha(t)$. The Raman-active mode has its minimum and maximum in polarizability at the extremal positions. On the

[4] Recall that the energy of a photon is proportional to its frequency: $E = h\nu$, where h is Planck's constant.

other hand, the Raman inactive mode has its minimum in polarizability at the equilibrium position, while the maxima are symmetric about the origin.

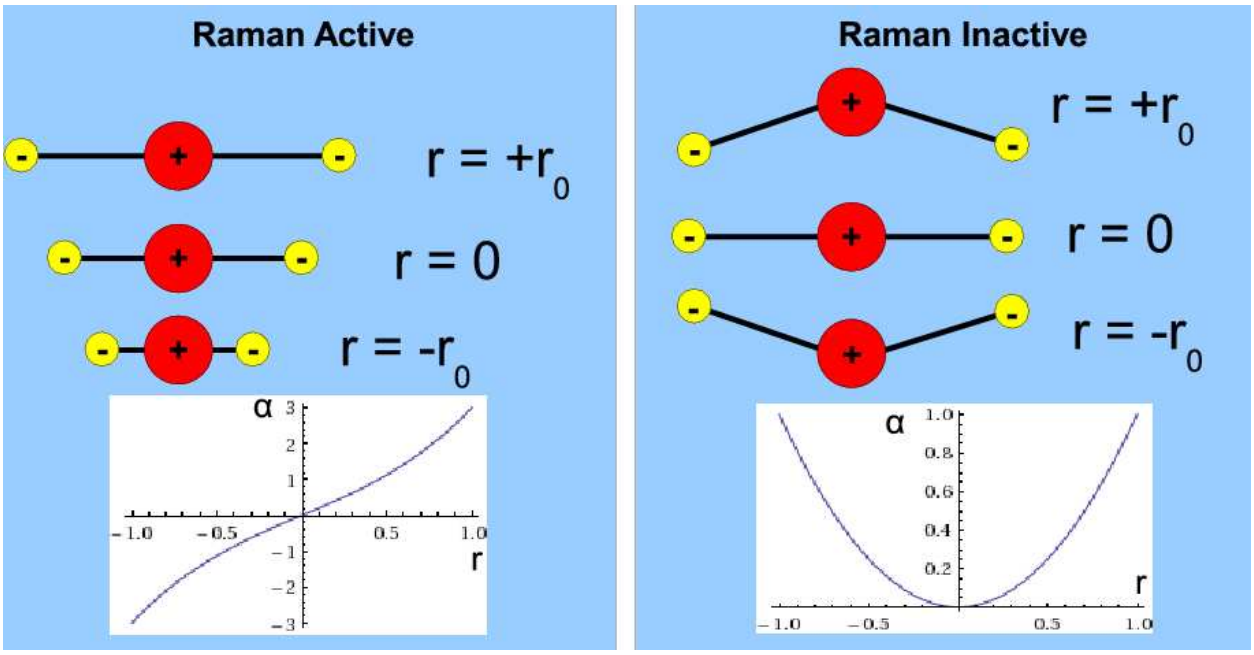

Figure 5.6: Raman-active and -inactive modes. Vibrations of molecules are shown with a corresponding plot of $\alpha(r)$ in arbitrary units. Red and yellow are areas where opposite charge clouds would be induced by an electric field. Left: Modes that have a nonzero change in the molecule's polarizability at the equilibrium position are Raman-active. This stretching mode is called a "longitudinal phonon." Right: Modes that have a zero change in the polarizability at the equilibrium position are Raman-inactive. This bending mode is called a "transverse phonon." Note that in more complex molecules, longitudinal phonons can be Raman-inactive and transverse phonons can be Raman-active.

5.3.1.2 Aside: Phonons and Types of Phonons

Note that the two types of vibration shown in Figure 5.6 are fundamentally different in a way not related to their polarizability. The mode displayed on the left is a "stretching" or "breathing" mode. It relies on the stretching and compression of the distance between the charge clouds. On the other hand, the mode displayed on the right is a "bending" mode. There is an oscillation perpendicular to one of the axes. In condensed matter materials, these vibrational modes can be restricted to discrete energies by the periodic boundary conditions of a unit cell. When vibrations are quantized, they are called "phonons." A stretching mode is called a "longitudinal phonon" and a bending mode a "transverse phonon."

5.3.1.3 The Quantum Connection

The classical description of Raman scattering fails to account for a key observation: Stokes scattering, is a much stronger effect than anti-Stokes scattering. While equation 5.13 correctly predicts that Rayleigh scattering is a stronger effect than Raman scattering—r was assumed to be small so that we could Taylor expand it; Raman scattering can be thought of as a higher-order correction to Rayleigh scattering—it does not reflect the difference in intensities for Stokes and anti-Stokes scattering at all. To understand this discrepancy, one must consider the quantum-mechanical picture of scattering.

In Rayleigh scattering, an incident photon that does not match the energy distance between two well-defined energy states in the system excites an electron from its ground state to what is called a "virtual excited state," an energy state allowed only by the Heisenberg uncertainty principle, $\Delta E \Delta t \gtrsim h$. The virtual excited state can only exist for a small time, since the more well-defined a time is, the less well-defined a corresponding energy is. As time passes, the uncertainty that allowed the state to exist disappears, and the state disappears with it. When this happens, the electron decays back into its ground state, emitting a photon with the same energy as the exciting photon, but in a random direction. It is important to note that, while this sounds very similar to stimulated emission or saturable absorption, it is a fundamentally different process. In stimulated emission, the stimulating photon is not absorbed and the emitted photon goes in the same direction as the stimulating photon. In the case of Rayleigh scattering, the stimulating photon is absorbed and the emitted photon propagates in a random direction. That said, Raman scattering is a *coherent* process, just like stimulated emission.

In a vibrating molecule, the electron has an additional allowed energy state: the vibrational semi-classical simple harmonic oscillator state with energy equal to $E = E_0 + \frac{1}{2}k_s r_0^2$, where the first term is the ground-state energy and the second comes from equation 5.9. In Stokes scattering, the electron is excited out of its ground state into the virtual excited state, but it decays into the vibrational state, emitting a photon less energetic than it absorbed. In anti-Stokes scattering, the electron starts in the vibrational state, is excited into a virtual excited state, and then decays back into its ground state, emitting a photon more energetic than the one it absorbed. Figure 5.7 depicts this model of scattering and highlights the differences

between Rayleigh, Stokes, and anti-Stokes scattering.

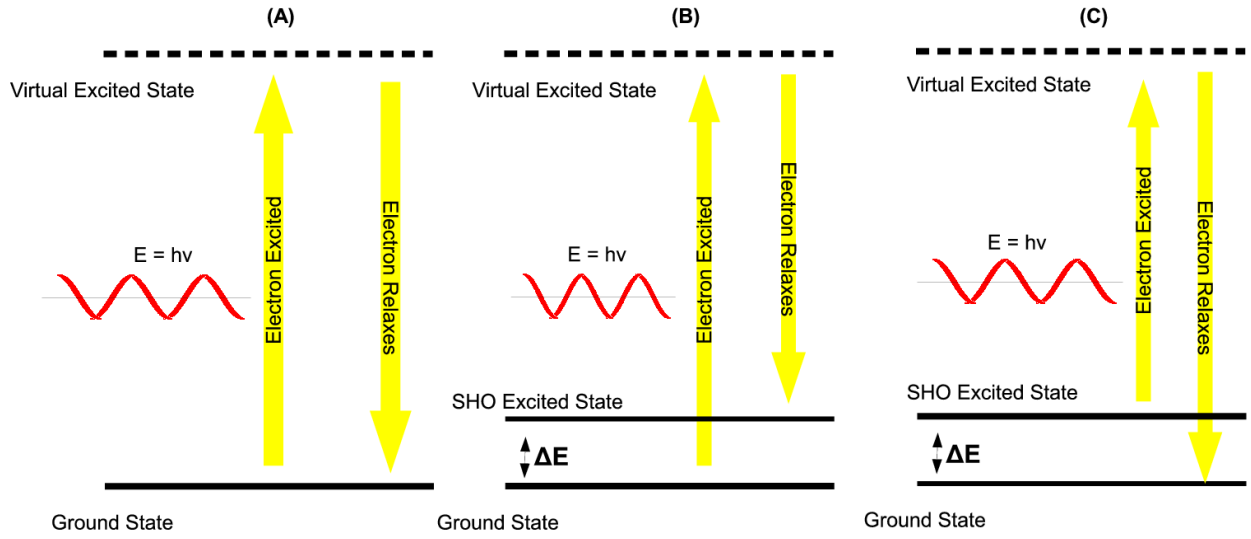

Figure 5.7: The quantum description of scattering. (A) Rayleigh scattering. An electron absorbs a photon and is excited from its ground state into a virtual excited state. It then decays back down into the ground state, emitting a photon of the same energy in a random direction. (B) Stokes scattering. An electron absorbs a photon and is excited from its ground state into a virtual excited state. It then decays into an excited state from the simple harmonic motion of the molecule and emits a photon of reduced energy in a random direction. (C) anti-Stokes scattering. A photon is excited from an excited state due to simple harmonic motion into a virtual excited state. It then decays into its ground state, emitting a higher-energy photon.

At any given time, the number of electrons in the excited vibrational state compared to the number of electrons in the ground state is given by the Boltzmann distribution:

$$\frac{N_1}{N_0} = \frac{g_1}{g_0} e^{-(E_1 - E_0)/k_B \mathcal{T}}. \tag{5.15}$$

In this case, N_1 is the population of the vibrational excited state, N_0 is the population of the ground state, g_1 is the degeneracy of the excited state, g_0 is the degeneracy of the ground state, $E_1 = \frac{1}{2} k_s r_0^2 + E_0$ is the energy of the vibrational state, E_0 is the energy of the ground state, k_B is Boltzmann's constant, and $\mathcal{T}$ is the temperature of the electrons in the material. This explains why anti-Stokes scattering is a weaker effect than Stokes scattering. There are far fewer electrons that start in the vibrational state than in the ground state, so the probability of one absorbing an incident photon is proportionally lower. However, the frequencies of Stokes and anti-Stokes scattered light are symmetric around the frequency of the exciting photon. For this reason, spectroscopists almost universally measure Stokes scattering rather anti-Stokes scattering.

It is important to note that this neglects the fact that electrons are fermions. If there are a finite number of momentum states at each energy level, this ratio is instead given by the Fermi-Dirac distribution, which accounts for the Pauli Exclusion Principle. In the Fermi-Dirac distribution, the number of electrons in a given state i of energy E_i is given by $N_i = \left[e^{(E_i - E_F)/k_B \mathcal{T}}\right]^{-1}$. However, the trend is the same.

5.3.1.4 Resonance Raman

The above treatment relied on there not being an excited state that matched the energy of the incident photon. However, Raman scattering still exists when such a state is allowed, although the timescale can be much longer—the timescale was originally so short before because the virtual excited state could not exist for very long. In this case, the probability of absorption and subsequent intensity of scattering is much greater. Figure 5.8 shows resonant Stokes scattering for a generic two-level system under laser radiation. Note that in the case of quantum mechanical systems, selection rules determine which modes are Raman or IR active. These are more abstract symmetry arguments than the ones used for the classical picture of a simple molecule.

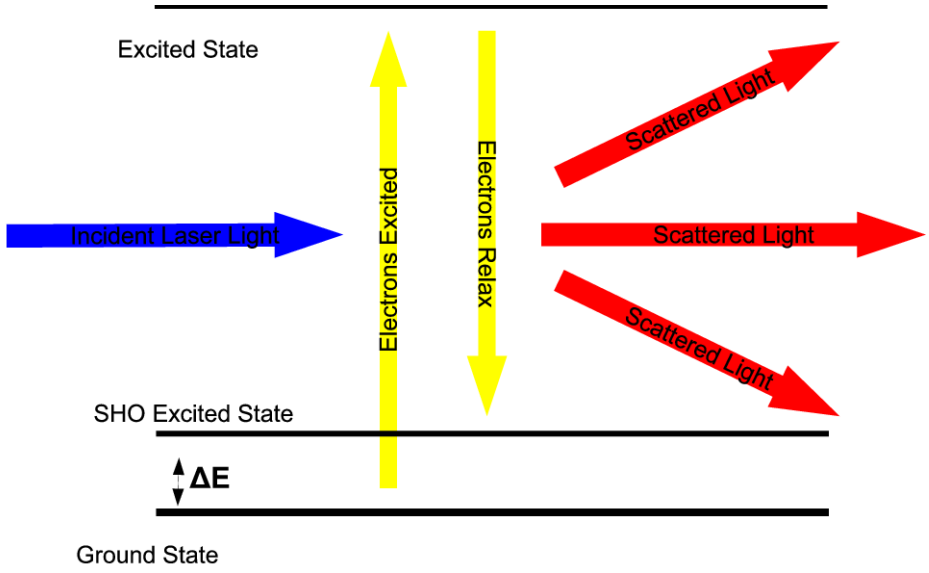

Figure 5.8: Resonant Stokes scattering for a generic two-level system under laser radiation. Laser light excites an electron from the ground state to an excited electronic state before that electron decays into a vibrational state, emitting a lower-energy photon. Probability of absorption, and thus scattering is much higher than in normal scattering because the excited state is an allowed electronic state.

5.3.1.5 Connection to Band Structure

The following treatment draws heavily from the work of G.F. Dresselhaus et al. [51], who perform a much more in-depth analysis. All of the Raman theory described above can be extended to band structure, with one complication. In band structure, momentum plays a critical role in the state of a particular electron, and allowed energy as a function of momentum can vary wildly (see section 2.2.1). While a vibrational state usually has only slightly greater energy than any nearby purely electronic state, the momentum of a harmonic oscillator state can be significant compared to the momentum of a purely electronic state. To reflect this, an electron moving from an electronic state to a vibrational state is represented by "electron-phonon scattering," where the energy of an electron will change only slightly, but its momentum might change drastically.[5] The new energy and momentum may not appear to be an allowed state, since band structure is calculated purely from an electronic perspective and the vibrational effects are a perturbation. However, it is allowed as a superposition state of vibrational and electronic allowed states. After at least one such electron-phonon scattering event, and perhaps one or more non-vibrational transitions, the electron must end up at its original momentum, or it will move out to infinity and no scattering will be observed.

When the electron scatters into another purely electronic state after interacting with a phonon, this is called a "resonance event." The "resonance order" of a Raman scattering emission is equal to the number of resonant transitions that occur between absorption and emission. For instance, consider the Stokes scattering that causes the so-called G peak in the Raman spectrum of graphene (left Figure 5.9). In this scattering event, an electron is excited from the valence band to the conduction band, scatters off of a phonon to an energy slightly below the valence band but at approximately the same momentum, and then decays into the valence band. This is called "single resonance" Raman scattering. On the other hand, consider Stokes scattering that causes the 2D (also called the G' peak) peak in graphene (upper right Figure 5.9). In this event, an electron is excited into the conduction band from the valence band, scatters off of a phonon to another allowed momentum state in the band structure with only slightly reduced energy, scatters off of another phonon back to its original momentum (but at a lower energy than allowed by a purely electronic band structure), and decays down into the valence band. This is called "double resonance" Raman scattering.

[5] It is important to note that there are electron-phonon events where the momentum of the electron changes negligibly.

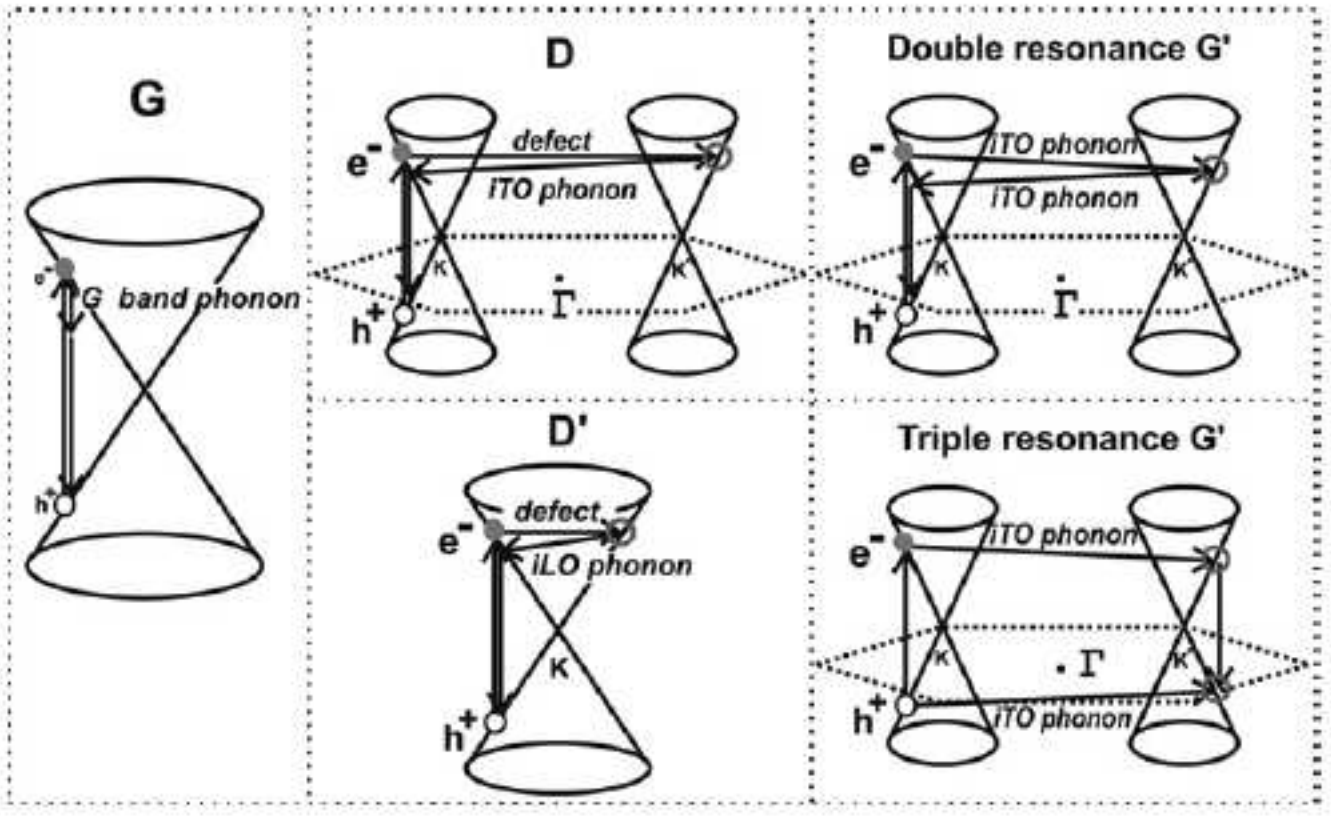

Figure 5.9: Stokes scattering in the band structure of graphene, viewed near the Dirac point. Assumes insulating phase ($E_F = 0$). iTO represents in-plane transverse optical phonons. iLO represents in-plane longitudinal optical phonons. e^- represents the excited electron. h^+ represents the hole left behind by the excited electron. **Left:** The single-resonance event responsible for the G peak in graphene's Raman spectrum. An electron is excited from the valence band into the conduction band, scatters off of a phonon to a lower energy with negligible change in momentum, and then decays back into the valence band, emitting a photon. **Center:** Defect peaks. One-phonon double resonance processes responsible for the D peak (top, spans two Dirac cones) and D' peak (bottom, spans a single Dirac cone) in the Raman spectrum. An electron is excited into the conduction band, then violates conservation of momentum by scattering off of a defect in the graphene lattice, moving into another allowed state of the same energy in the conduction band. It then scatters off of a phonon back to its original energy, but at reduced momentum, before decaying back into the valence band and emitting a photon. The D peak will be discussed below. However, the D' peak is only presented as another example of a Raman process in graphene. **Right:** The double (top) and triple (bottom) resonance processes that contribute to the 2D or G' band in the Raman spectrum. **Top right:** Double resonance. An electron is excited from the valence band into the conduction band, scatters off of a phonon to an allowed state of lower energy in a nearby Dirac cone, scatters off of another phonon back to its original momentum but at a further-reduced energy, and decays into the valence band, emitting a photon. **Bottom right:** Triple resonance. An electron is excited from the valence band into the conduction band and scatters off of a phonon into an adjacent Dirac cone. It then decays to another electronically allowed state in the adjacent Dirac cone, emitting a photon, before recombining with its original hole, which has scattered into the adjacent Dirac cone off of another iTO phonon. Images from L. M. Malard et al. [71].

5.3.2 The Raman Spectrum of Graphene

This section will discuss the major landmarks in the Raman spectrum of graphene, acquired by measuring the frequency of Stokes-scattered laser light off of the graphene surface at normal incidence. Unless otherwise stated, all information in this section is contained in works by both G.F. Dresselhaus et al. [51] and by L.M. Malard et al. [71]. In general, the spectrum is independent of the frequency of incident laser light, since it is the difference between phonon energy and electron energy that matters. For this reason, the spectrum is measured in Raman shift, with units of relative wavenumbers (rel. cm^{-1}). With these units, Raman shift is defined as

$$R.S.(\lambda) = \left(\frac{1}{\lambda_0} - \frac{1}{\lambda}\right) \times 10^7, \tag{5.16}$$

where λ_0 is the wavelength of the exciting laser in nm and λ is the wavelength of the Stokes-scattered light in nm. These units give Stokes scattered light a positive shift and anti-Stokes scattered light a negative shift, since the former is more likely to be measured. This has the added benefit of setting the energy of a vibrational mode to be the same sign as the Raman shift. As Raman shift increases, so does the energy of the phonon being measured. However, graphene does have some dependence, especially in the 2D peak (discussed below). For the purposes of this work, it can be assumed that all Raman spectra were measured with a laser wavelength of $\lambda_0 \approx 632.8$ nm unless otherwise stated. Every spectrometer is different, so absolute intensities for spectral lines mean very little in Raman spectroscopy. Instead, the ratios of the peaks are important. As such, the y-axis is usually in arbitrary units.

Since graphene has no bandgap and absorbs light at every frequency, all Raman scattering is resonance Raman scattering. This means that graphene's Raman spectrum is much more intense than for a material with a bandgap. This is fortunate, since graphene has substantially fewer atoms in it to produce a Raman signal than bulk materials, since a graphene layer is only one atom thick. In fact, it is resonance Raman scattering that makes the Raman spectrum of graphene measurable at all—most substances only have a measurable Raman spectrum in bulk. The spectrum from a thin film of silicon dioxide, for example, is probably negligible. Resonance Raman peaks usually obey the Lorentzian distribution, or a superposition of many Lorentzian distributions in the case of peaks near each other. A single Lorentzian-distributed Raman

peak, $I(\Delta\nu)$, obeys the following equation:

$$I(\Delta\nu) = \frac{I_0}{\pi}\left[\frac{w}{(\Delta\nu - \Delta\nu_0)^2 + w}\right], \tag{5.17}$$

where $\Delta\nu$ is Raman shift, $\Delta\nu_0$ is the center wavenumber of the peak, I_0 is the amplitude of the peak, and w is the full width at half maximum (FWHM) of the peak. Figure 5.10 shows an example of what the Raman spectrum of graphene looks like, with the peaks labeled.

Because graphene is a two-dimensional system, it has become convention to name transverse phonons as either in-plane (i) or out-of-plane (o). This convention is often extended to longitudinal phonons, though it is somewhat redundant in the case of a two-dimensional material (for further discussion, see Dresselhaus et al. [51]). All phonons that contribute to Raman scattering are so-called "optical phonons" (O), named because they have energies and frequencies of approximately the same order of magnitude as light. This is in contrast to "acoustic phonons," (A), which have frequencies of the same order of magnitude as human-audible sound. These symbols can be strung together: first in-plane or out-of-plane, then transverse or longitudinal, and finally optical or acoustic. So, as an example, an in-plane transverse optical phonon would be denoted as an iTO phonon.

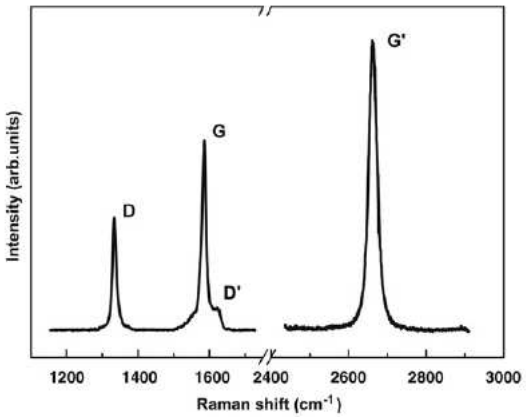

Figure 5.10: A sample Raman spectrum of a graphene edge showing all of its salient peaks. From left to right: D peak, G peak, D' peak, and G' or 2D peak. It is important to note that the edge of a graphene sheet is a defect in the lattice, and thus this Raman spectrum represents low-quality graphene. Ideal undoped monolayer graphene shows no D peak and a 2D peak at least twice as intense as the G peak. Image by Malard et al. [71].

5.3.2.1 The G Peak

The G peak of the Raman spectrum of graphene is present in all sp^2-bonded carbon systems and is named after "graphite." Intuitively, it is generated by photons scattering off of transverse in-plane (iTO) vibrations, a process described above and shown in Figure 5.9 (left). It is the center peak in Figure 5.10, located at a Raman shift approximately 1585 rel. cm^{-1} with a full width at half maximum of about 13 rel. cm^{-1}. It responds to strain, Fermi level shift (i.e., doping), and nearly any process that alters the thermodynamic qualities of the system. How doping affects the G peak will be discussed later. However, a simple and interesting example of how the environment can affect the G peak is uniaxial strain. In a "pristine" state, graphene is totally unaffected by its environment, and the lattice is radially symmetric. Because of this, iTO phonons with amplitudes of vibration in the $\hat{x}$ direction, for instance, are the same as those with amplitudes of vibration in the $\hat{y}$ direction, where $\hat{y} \perp \hat{x}$. However, as shown in Figure 5.11(A), when strain along a single linear axis is applied to the sheet, this symmetry is broken, and vibrations *parallel* to the strain axis have a lower energy than vibrations *perpendicular* to it. This causes the G peak to split, as shown in Figure 5.11(B).

5.3.2.2 The 2D Peak

The 2D peak of the Raman spectrum of graphene, also called the G' peak, is found at approximately 2680 rel. cm^{-1} with a full width at half maximum of approximately 24 rel. cm^{-1}. It is generated by two separate processes; the first is described above and shown in Figure 5.9 (top right). The second is shown in Figure 5.9 (bottom right) and will be described now. An electron absorbs an incident photon and is excited from the valence band into the conduction band. It then scatters off of an iTO phonon into an adjacent Dirac cone. At the same time, the hole it left behind scatters off of another iTO phonon into the valence band of the adjacent Dirac cone. The electron then decays into the valence band of the Dirac cone, recombining with its hole and emitting a photon. It is difficult to intuitively understand what causes the 2D peak in the same way as with the G peak because the double and triple resonance processes defy a first-order description. However, the 2D peak is related to the radial breathing modes of the benzene rings in the graphene, which grow and shrink and wiggle. For a much deeper description of these double and triple resonance processes,

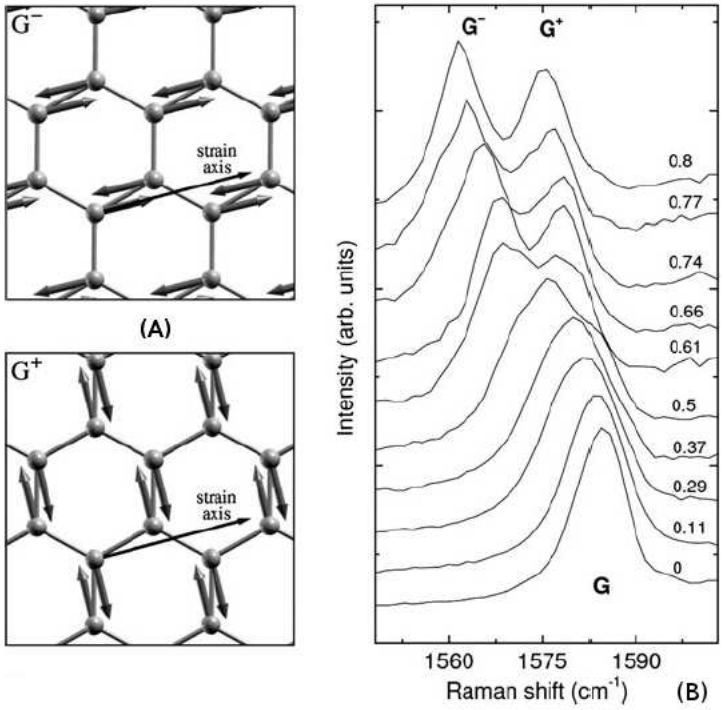

Figure 5.11: The effects of uniaxial strain on the G band of graphene. (A) The broken symmetry of the G phonons under strain. Without a strain axis, all directions are the same. However, under a strain axis, the G^- band (top) has less energy than the G^+ band (bottom). (B) The splitting of the G peak into the G^+ and G^- peaks in the Raman spectrum under uniaxial strain. Strain in units of % breaking point is listed next to each measurement. Image adapted by Dresselhaus et al. [51] from Mohiudden et al. [72].

see Dresselhaus et al. [51].

These higher-order processes are extremely sensitive to perturbation such as doping (discussed later) and energy of the exciting laser. As shown in Figure 5.12, the center wavelength of the 2D peak depends linearly on the wavelength of the exciting laser. This dependence is related to the requirement that the process be related across two Dirac cones. The state that the electron reaches in the second Dirac cone is dependent on the energy it is excited to in the conduction band of the first cone, and thus on the excitation energy.

5.3.2.3 The D Peak

The D peak of graphene, found at approximately 1350 rel. cm^{-1} with a FWHM of approximately 10 rel. cm^{-1}, is related to a loss of momentum conservation. Loss of momentum conservation, in turn, is

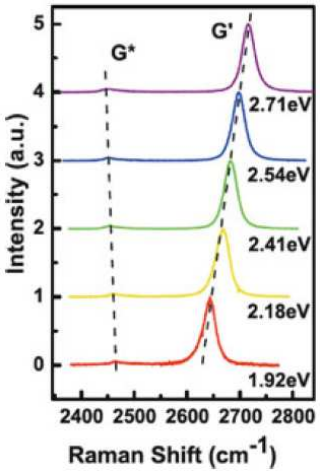

Figure 5.12: The wavelength dependence of the 2D band of graphene, (photon energy listed next to each curve). The G* band is a higher-order peak than the 2D band and also depends strongly on exciting photon energy. Image from Dresselhaus et al. [51].

enabled by defects in the graphene lattice. A hole in the graphene lattice or an edge to a flake can act as an impenetrable wall and cause an electron or phonon to suddenly stop or scatter in a new direction, resulting (from the perspective of the band structure) in conservation of energy but not of momentum.[6] The process resulting in the D peak is shown in Figure 5.9 (top center). An electron is excited from the valence band into the conduction band, where it scatters off of a defect, changing its momentum so greatly that it ends up in an allowed state in another Dirac cone. It then scatters off of an iTO phonon back to its original momentum but at a lower energy than allowed by the strictly electronic band structure. The electron then decays back into the valence band, emitting a photon and recombining with the hole it left behind. Since it is proportional to the number of defects in the lattice, the intensity of the D peak relative to the intensities of the other peaks is an extremely good indicator of the quality of a graphene sheet. Ideally, a graphene sheet should have no D peak whatsoever. Depending on the spot size of the probing laser light, it is often possible to approximate the region emitting scattered light as much smaller than the total sheet. In this case, the intensity of the D peak can be used as a sensitive probe of the local quality of the lattice, and it has been used to detect edges of the graphene crystal domains [73].

[6] Momentum is actually conserved for the total system, but the electron or phonon's momentum is lost to the large atomic nuclei. This is analogous to a car hitting a cement wall. The large mass of the cement wall gives it a much greater momentum than the car. So, the wall can absorb the momentum of the car without any apparent motion. Thus, although momentum transfer occurs, it appears as if the car suddenly stops.

5.3.3 Previous Work

Since Geim and Novoselov started the "graphene gold rush," an enormous amount of time and effort has gone into understanding the Raman spectrum of graphene. Two important topics in this research effort are understanding the relationship between the number of layers of a graphene sheet and its Raman spectrum and the behavior of doped graphene.

5.3.3.1 The Relationship Between the Number of Layers of Graphene and its Raman Spectrum.

Early in the research effort focused on graphene, when high-quality sheets could only be attained by mechanical exfoliation, it was important to be able to easily determine the number of layers—and the type of stacking of those layers—of a graphene sheet easily and non-intrusively. "Lattice-matched" graphene is stacked in such a way that the layers are highly ordered. This strongly affects the band structure. In contrast, monolayers in so-called "turbostratic" graphene are stacked randomly. This has a weaker but non-trivial effect on the band structure. Unfortunately, individual measurements by optical microscopy are difficult and atomic force microscopy (AFM) damages the samples. A.C. Ferrari et al. established that the number of layers of lattice matched graphne can be determined by the Raman spectrum of a sample [74]. Similarly, L.G. Conçado and colleagues found a way to distinguish between monolayer and turbostratic multilayer graphene [75].

The only noticeable difference between turbostratic multilayer graphene and monolayer graphene is a broadening of the 2D peak. The FWHM of the 2D peak for turbostratic graphene is approximately between 45 rel. cm^{-1} and 60 rel. cm^{-1}. This is an important measurement to be able to make, since CVD graphene grows turbostratically. Thus, Raman spectra can be used to determine the number of layers of graphene grown by chemical vapor deposition. In contrast, the shape of the 2D peak changes drastically for lattice-matched multilayer graphene. As Figure 5.13 shows, as the number of layers grow, the graphene sheet becomes more and more like highly-ordered graphite. The intensity drops from greater than twice the intensity of the G peak to about half. The 2D band further splits into a number of bands that superimpose to generate an extremely broadened asymmetric peak.

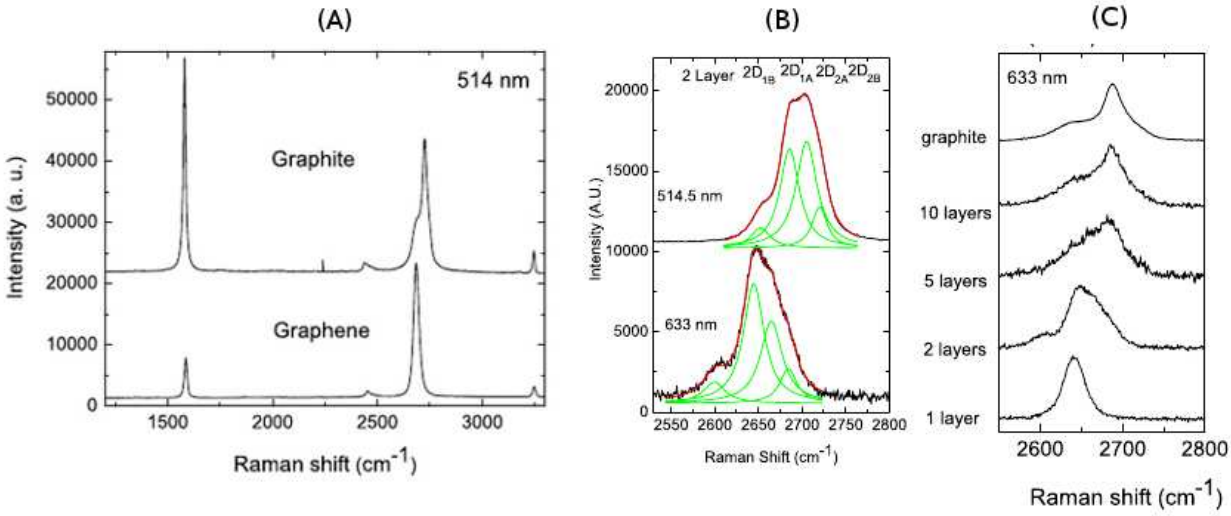

Figure 5.13: The Raman spectrum of lattice-matched graphene of many layers. (A) The Raman spectrum of graphite compared to graphene measured with a laser excitation wavelength of $\lambda_0 = 514.5$ nm. (B) The 4 Lorentzian peaks superimposed to produce the 2D peak of bilayer lattice-matched graphene. Top measured at $\lambda_0 = 514.5$ nm; bottom measured at $\lambda_0 = 633$ nm. (C) The shape of the 2D peak as a function of number of layers. Measured at $\lambda_0 = 633$ nm. Image adapted from Ferrari et al. [75].

5.3.3.2 Doping

Two types of study have been performed on doped graphene. The first type of study performed was on electrostatically-doped graphene, rather than chemically-doped graphene. To electrostatically dope graphene, one places it between an electrode and a dielectric material in a capacitor. When a voltage is applied, the dielectric material polarizes and develops a bound surface charge density. Intuitively, this charge behaves like the H^+ ions in chemical doping by a strong acid (see Figure 5.2) and attracts and immobilizes charge within the graphene, effectively doping it. Figure 5.14 shows a possible electrostatic doping experiment. A number of electrostatic doping experiments were performed on graphene. Works by Novoselov et al. [29], J. Yan et al. [76], and A. Das et al. [77] will be discused: all of them show the same basic trends.

As Figure 5.15 shows, studies of electrostatic doping found that center wavenumbers of both the G and 2D peaks initially increased in Raman shift—this is called "up-shifting" if the center wavenumber increases and "down-shifting" if the wavenumber decreases—as the Fermi level moved away from the Dirac point.

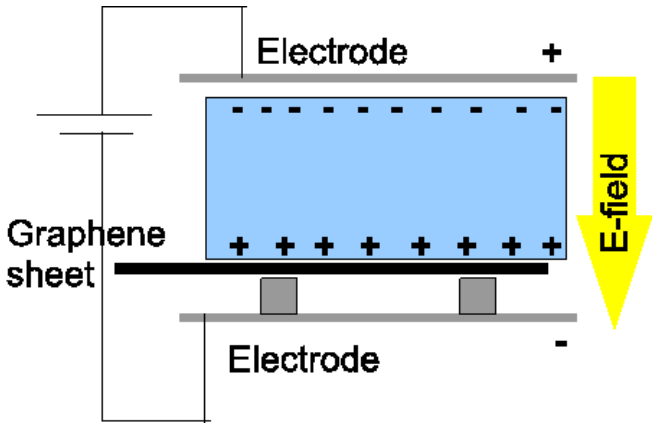

Figure 5.14: Electrostatic doping of graphene.

Eventually this trend reversed, but only for n-doping and for the 2D peak at extremely large Fermi-level shifts. The G peak ratio also narrowed as the Fermi level shifted away from the Dirac point. However, the most obvious change was in the ratio of the intensity of the 2D peak to the intensity of the G peak, $I(2D)/I(G)$, which decreased drastically with increased doping. This indicates that this ratio is a strong indicator of Fermi level if the graphene is known to be monolayer. It is important to note that this ratio can change depending on the substrate. Constructive and destructive interference in the substrate can cause surprisingly drastic differences, and doping can vary widely by substrate material.

The second type of study was performed on chemically doped graphene by X. Dong et al. [78]. Dong and colleagues doped graphene by a variety of organic molecules, attaining both electron- and hole-doped graphene. They used a variety of known p-doping and n-doping organic molecules to attempt to shift the Fermi level of their graphene samples, then measured the Raman spectra of those samples. They found that their organic dopants induced a strong D peak in the material (see Figure 5.16), indicating that their dopants damaged the graphene lattice. They also found that $I(2D)/I(G)$ decreases rapidly with increased doping level, just as the researchers who studied electrostatic doping found, which confirms that this ratio is a strong indicator of doping level. However, Dong et al. had fundamentally different results concerning the shifts of peaks. Both Dong et al. and those who studied electrostatically doped graphene found that the 2D peak up-shifts for both p-doped and n-doped graphene. However, Dong et al. found that the G peak up-shifts for p-doped graphene and down-shifts for n-doped graphene. This indicates that chemical doping

affects graphene in ways that electrostatic doping does not and that different molecules might have different effects.

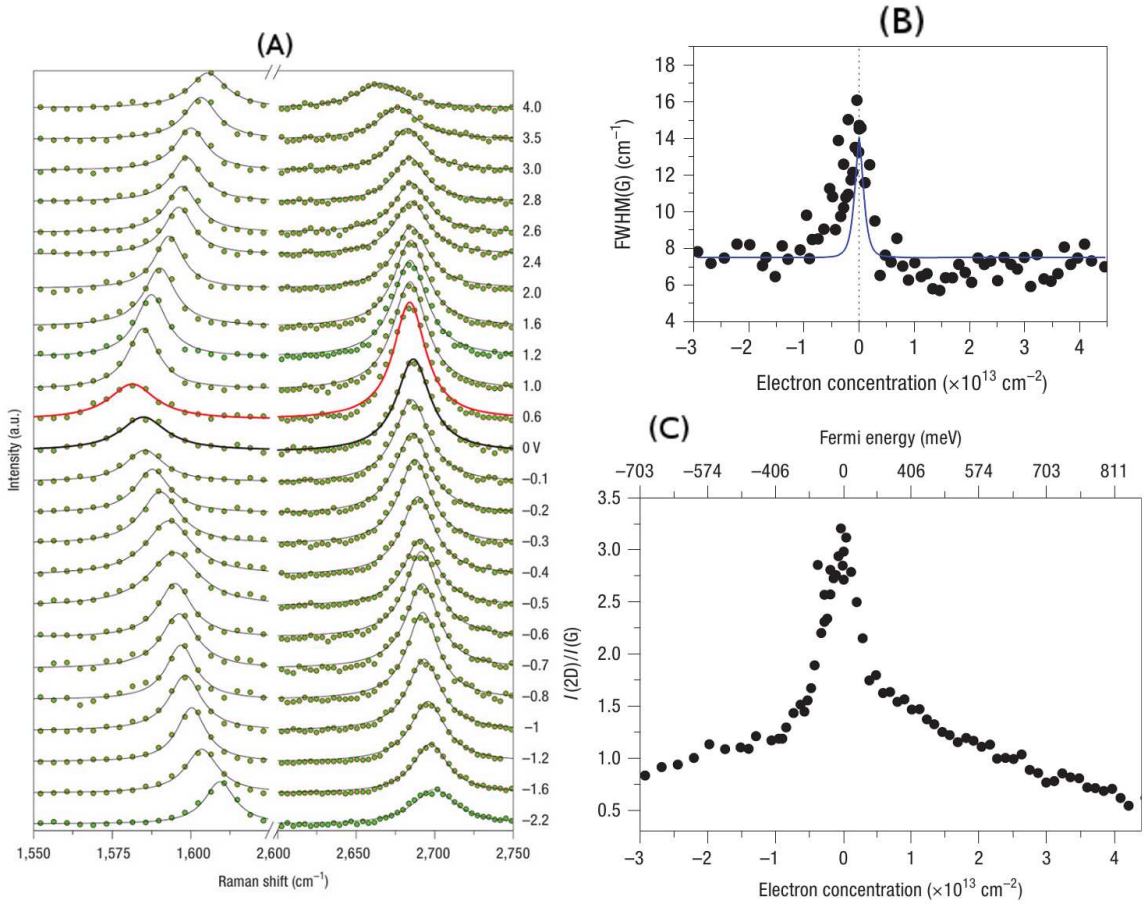

Figure 5.15: Raman Spectrum of electrostatically doped graphene. (A) The full Raman spectrum of the doped graphene as a function of applied voltage (analogous to doping concentration). The applied voltage in volts is marked next to each curve on the right of the plot. Red curve denotes undoped. In this case, a positive voltage corresponds to electron doping, while negative voltage corresponds to hole doping. (B) The FWHM of the G peak as a function of concentration of charge-carrying electrons in the material. (C) The ratio of the intensity of the 2D peak compared to the intensity of the G peak as a function of Fermi level (upper axis) and concentration of charge-carrying electrons (bottom axis). Image adapted from work by Das et al. [77].

5.3.4 Our Study

To collaborate the results from Section 5.2, we performed Raman spectroscopy on samples doped by various concentrations of nitric acid and to various Fermi levels as measured by spectrophotometer. The

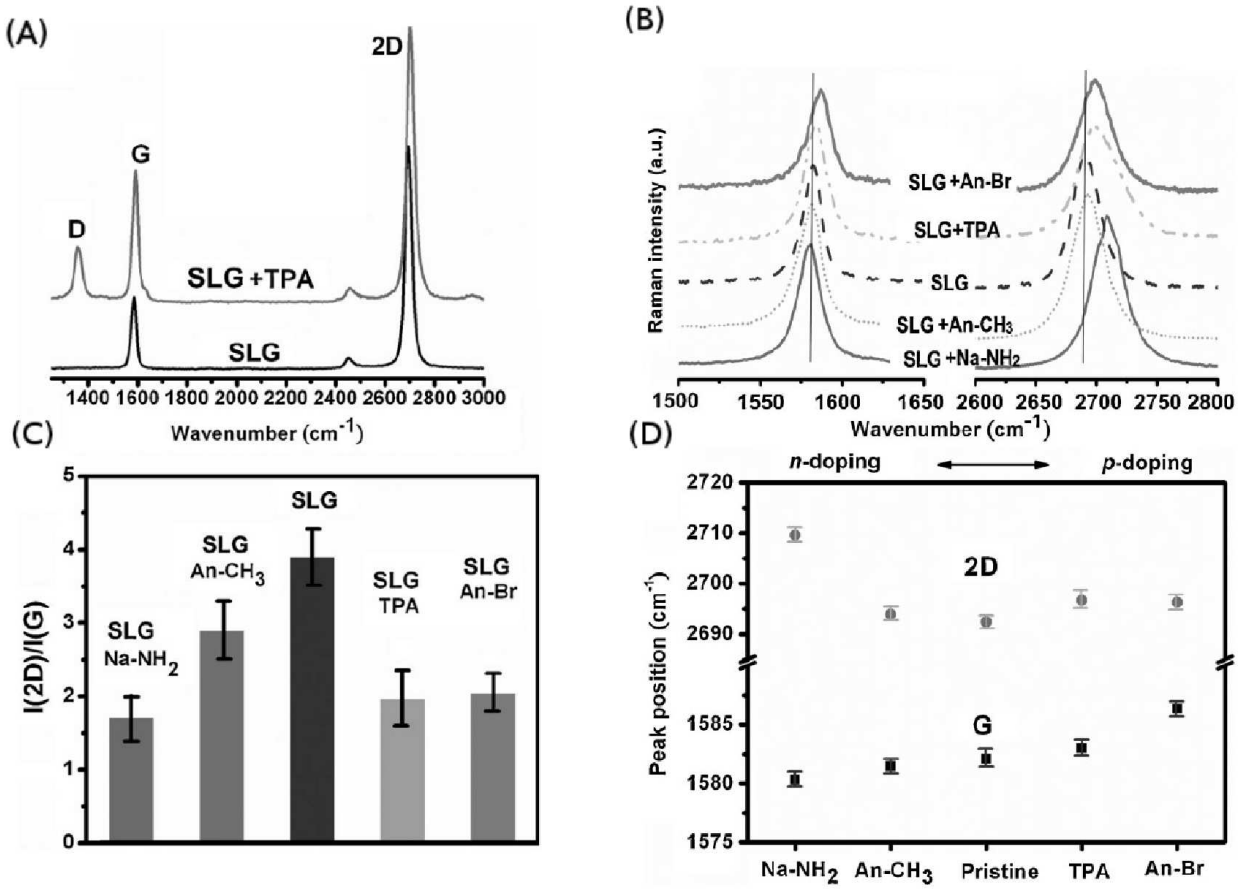

Figure 5.16: The doping of graphene by aromatic (for these purposes, organic) molecules. (A) The Raman spectrum of pristine single-layer graphene, denoted SLG, compared to graphene doped by a strongly p-doping aromatic molecule, denoted TPA. A D peak is induced and the G and 2D peaks both up-shift. (B) The G (left) and 2D peaks (right) of graphene doped by various organic molecules. Ranges from strongly n-doped (bottom) to strongly p-doped (top). (C) Ratio of the intensity of the 2D peak compared to the G peak, I(2D)/I(G), for graphene doped by various organic molecules. Ranges from strongly n-doped (left) to strongly p-doped (right). (D) Mean peak positions of the 2D (top) and G (bottom) peaks in terms of dopant. Ranges from strongly n-doped (left) to strongly p-doped (right).

primary goal of this study was to confirm that doping was indeed occurring due to the acid and to confirm that the process is reversible.

5.3.4.1 Methods

Samples grown by the method outlined in Appendix A.2.2 were baked at 150°C and then prepared by immersion in various concentrations of nitric acid as in Section 5.2. We found that baking prevented delamination in the nitric acid. Undoped samples were baked so as to remain consistent. The samples

were then measured by Raman spectroscopy as quickly as possible—Nitric acid naturally evaporates into the environment, so time is a critical factor—or first measured by spectrophotometry to discover the Fermi level before being measured by Raman spectroscopy if a correlation was desired.

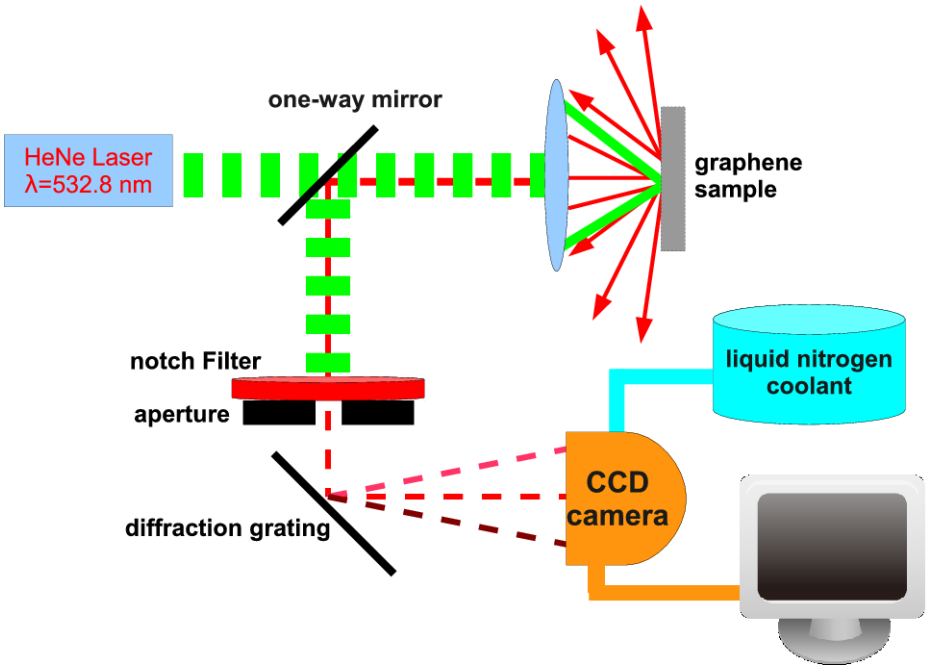

Figure 5.17: The home-built micro-Raman system used for measurements. Light from a Helium-Neon laser (depicted as green here, although the light is red in reality) is focused tightly onto a sample. As much Stokes scattered light (red) as possible is collected and collimated by the same lens (blue). The Rayleigh scattered light is then filtered away from the Raman scattered light by a cut-off filter. The Raman scattered light continues through an aperture (to prevent ambient room light from interfering with the measurement) and is reflected off of a diffraction grating. The grating reflects different colors of light by different angles, and each Stokes-scattered line falls on a different pixel on a liquid nitrogen-cooled charge-coupled device (CCD). A computer then reads the output from the CCD and converts it into a wavelength spectrum.

Raman measurements were performed on a home-built Raman microscope (see figure 5.17) designed such that exciting laser light is focused onto a sample at normal incidence to the sample and such that Raman scattered light is collected and recollimated by the same focusing lens. In this regime, it is important that the focusing lens have a large numerical aperture so that the solid angle of Raman scattered light caught by the lens and thus measurable is as large as possible. The excitation was provided by a 633 nm Helium-Neon (HeNe) laser. The laser light was focused to a spot size of approximately 1 μm by a 0.8 NA objective (Olympus 50x, MPlan FL). The Stokes scattered light is spectrally filtered with a 160 cm^{-1} cut-off filter (Semrock, LP02-633RU-25) and detected with a spectrometer with a 1200 g/mm grating (Newport,

53-*-220H) for single-peak measurements or a 600 g/mm grating (Newport, 53-*-350R) for measurements spanning the full relevant spectrum of graphene, and a liquid nitrogen-cooled charge-coupled device (CCD) (Princeton Instruments, Spec-10 2KB/LN). The spectrometer required some calibration, the details of which can be found in Appendix B.

B. Krauss et al. [79] found that laser light of even moderate intensity can cause damage to a graphene lattice over time. They report change in the Raman spectrum for intensities > 1.25 kW/cm^2 after several hours. To avoid damaging the sample or removing adsorbants with thermal effects, we kept the total power at the sample between 0.5 and 3 mW (< 1 kW/cm^2). We further ensured that our samples were never exposed on a single spot for more than 10 minutes. To confirm that our measurements were non-intrusive, an extremely short measurement was made before and after the longer integration-time, more precise measurements to confirm no change in the spectrum.

After Raman spectra were measured, a clean signal was extracted by using the algorithms found in Appendix C. The amplitudes of individual peaks were then measured and peaks were fit to Lorentzian distributions to find their center wavenumbers and FWHM values (see Appendix C). It is important to note that because the D peak was often difficult to distinguish from background noise, we intentionally overestimated its intensity so as to generate conservative estimates of the quality of our graphene.

5.3.4.2 Results

Initially, the Raman spectrum of graphene doped by various concentrations of nitric acid was measured. Figure 5.18 shows the effects of concentration of nitric acid dopant on the positions and widths of the peaks. After initial doping, both G and 2D peaks up-shift and narrow significantly, as observed in electrostatic doping [29, 76, 77] and in chemical doping by organic molecules [78]. As shown in Figure 5.19(A), we observed an initial decrease in the intensity of the 2D peak with respect to the G peak, I(2D)/I(G), as observed in both electrostatic and chemical doping [29, 76, 77, 78]. Fortuitously, we also observed almost no dependence on doping of the relative intensity of the D peak compared to the intensity of the G peak, I(D)/I(G) (see Figure 5.19(B)), indicating that the acid did not damage the graphene lattice.

We also never observed an I(D)/I(G) ratio greater than 0.15, which indicates that our samples were

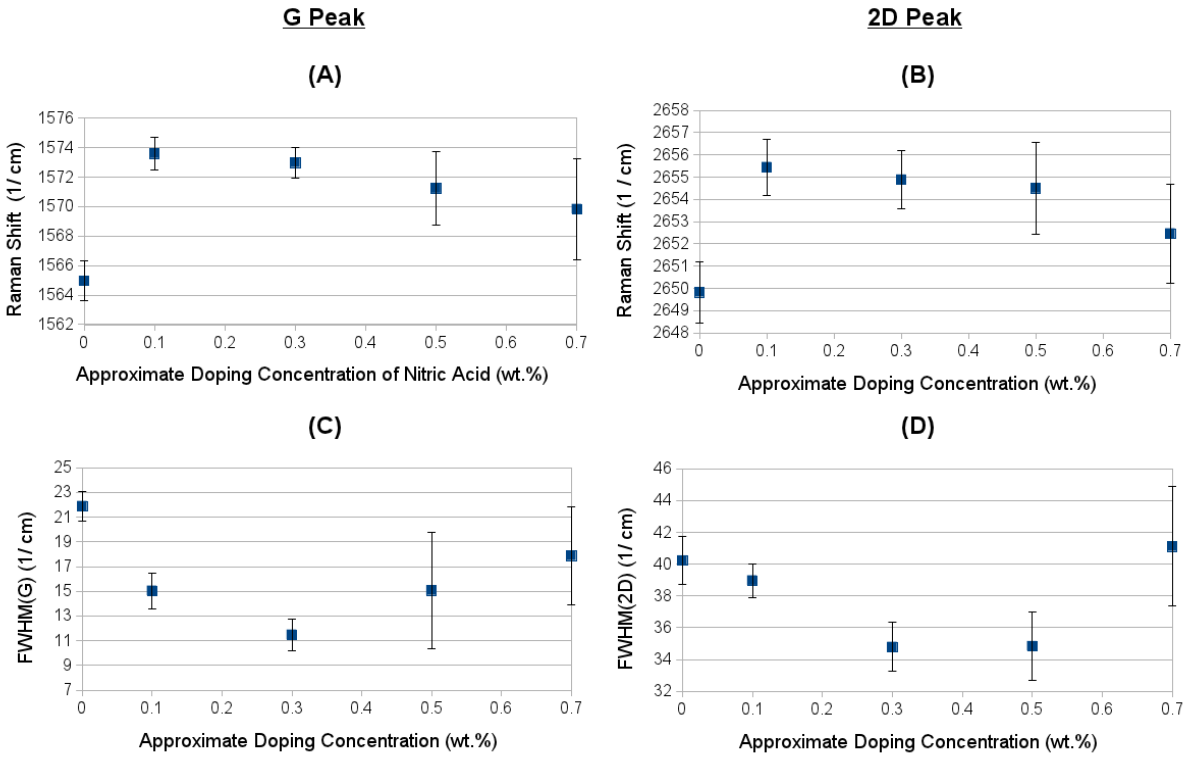

Figure 5.18: Mean peak positions and FWHMs as a function of doping concentration. On this scale, error in doping concentration is negligible. (A) Center wavenumber of the G peak. After initial doping, the G peak up-shifts significantly. It then slowly recovers with increased doping concentration. (B) Center wavenumber of the 2D peak. The 2D peak follows the same trend as the G peak. (C) The full width at half maximum of the G peak. The peak first narrows and then broadens again with increased doping. (D) The full width at half maximum of the 2D peak. It follows the same trend as the G peak.

of high quality. This is in contrast to the work of Dong et al., who reported an increase in I(D)/I(G) after doping by aromatic molecules [78]. Our undoped samples showed a single 2D peak with a FWHM ranging from 33 rel. cm^{-1} to 40 rel. cm^{-1}, indicating that the samples contained a mixture of monolayer and bilayer graphene—although the <2.3% absorption measured in differential transmission indicates that it was likely mostly monolayer, as expected. While ultra-low pressure CVD self-limits to produce mostly monolayer sheets, it has been observed that the nucleation site at the center of a crystal domain can be partly bilayer graphene [73].

However, with increased doping, we observed that the peaks began to recover, both down-shifting towards their original positions and broadening towards their original widths. This behavior diverges from that observed previously in either electrostatic doping or chemical doping [29, 76, 77, 78]. It is unclear if

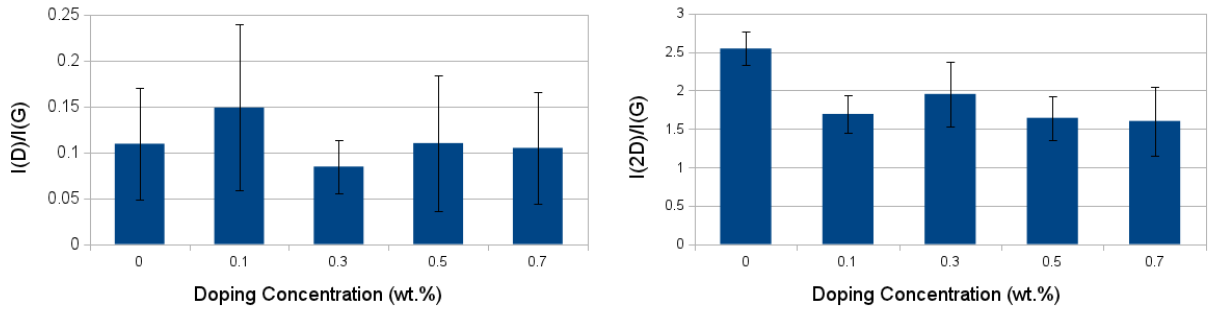

Figure 5.19: Dependence of relative intensities on doping concentration. Left: Dependence for ratio of intensities for D and G peaks, I(D)/I(G). Variation of I(D)/I(G) is statistically insignificant, with variation almost as great as its (very small) magnitude. Right: Dependence for ratio of intensities for 2D and G peaks, I(2D)/I(G). After doping, there is a clear initial decrease in this ratio. However, subsequent trends (if any) are statistically insignificant.

the behavior of I(2D)/I(G) diverges, since the decrease in this ratio becomes much less dramatic after the Fermi level has shifted substantially from the Dirac point. It is worth noting that uncertainty increases drastically with doping concentration, making exact behavior unclear. This is likely due to some spatial dependence of doping concentration (see Section 5.2), whose variance increases with concentration. This is not inconceivable, since nitric acid contains a high density of H^+ ions, which repel each other. The higher their concentration, the more likely they are to interact in some complicated way.

The following question then arises: Is there some systematic effect that causes the doping concentration to fail to accurately correlate to the shift of the Fermi level away from the Dirac point? It is possible that doping by nitric acid simply has poor reproducibility. Alternatively, it is possible that the dopant is removed by heating due to the laser used to excite Raman scattering, or simply by the time delay between doping and measurement.

To answer this question, we first measured the Fermi level of our doped graphene by spectrophotometry before measuring its Raman spectra. We ensured that we measured the Raman spectra of graphene doped to disparate Fermi levels by increased doping concentration if the Fermi level did not shift enough. Listed Fermi levels are approximate, since a more exact Figure with a listed uncertainty would only distract from any observed trends. The uncertainty in these values is small compared to a change in energy of more than 100 meV. We also baked the sample that had been doped to $E_F \approx 200$ meV at 100˚C for 1 hour

to remove dopants and determine if the process is reversible. Figure 5.20 shows representative spectra of pristine graphene and graphene doped to Fermi levels of approximately 200 meV and 400 meV, as well as the spectrum of the sample that was baked after doping.

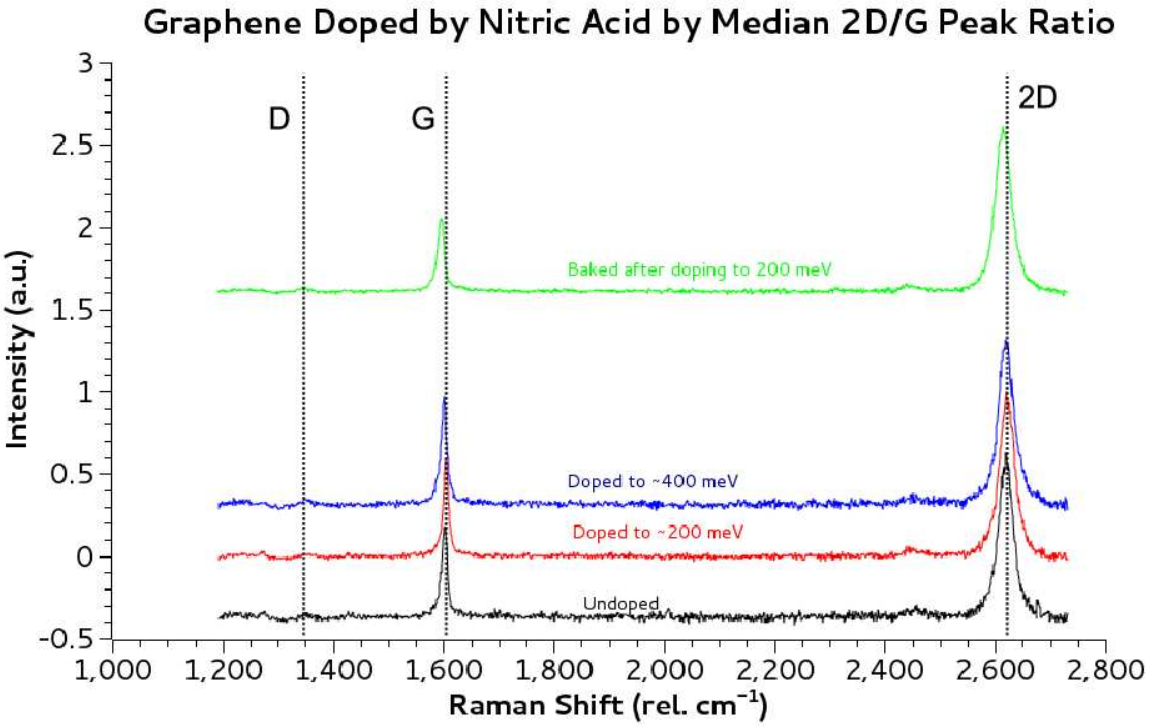

Figure 5.20: The Raman spectrum of graphene doped to various Fermi levels by nitric acid. The lack of a D peak indicates the high quality of the pristine samples and that doping by nitric acid does not damage the doped samples.

As shown in Figure 5.21, the peaks of graphene doped to various Fermi levels show the same up-shift after initial doping and then recovery with increased doping. In fact, this recovery is even more dramatic, indicating that the effect is not correlated with an inconsistency in Fermi level shift due to doping concentration. Although the change in I(2D)/I(G) is not large compared to the variance at higher doping levels, the initial drop after doping is likely significant, and the mean value continues to monotonically decrease with increased doping level, which is consistent with previous measurements on electrostatically-doped graphene [29, 76, 77] or graphene doped by aromatic molecules [78]. We thus conclude that the oscillation we observe in the center wavenumbers of the G and 2D peaks is a reproducible effect from doping by nitric acid. Since the Raman spectra of graphene doped by nitric acid is, to our knowledge, a never-

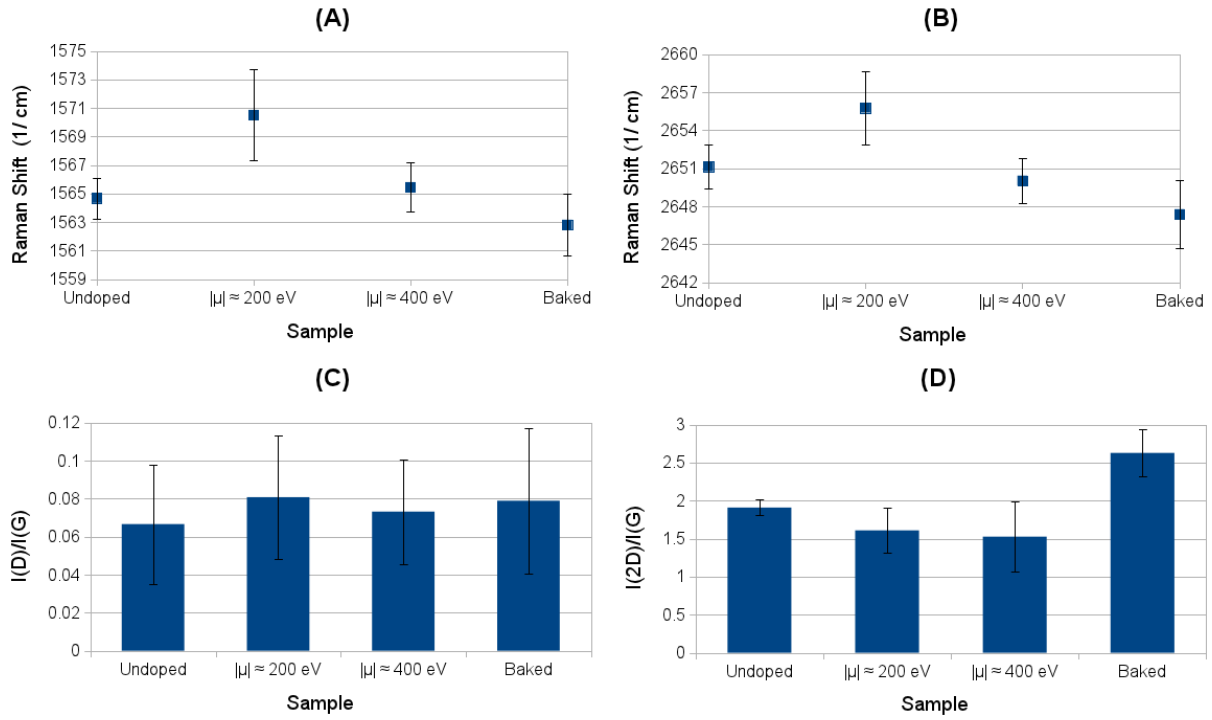

Figure 5.21: Trends for graphene doped to various Fermi levels by nitric acid. Here "$|\mu|$" represents E_F, undoped represents baked but never doped, and "baked" represents baked after doping. (A) Mean G peak position. (B) Mean 2D peak position. (C) Ratio of intensities of the D and G peaks. As before, this indicates no defects. (D) Ratio of intensities of the 2D and G peaks. FWHM of peaks not shown because the variation is too large for any change to be significantly significant.

before-studied phenomenon, it seems reasonable to believe that we do not observe this effect through error. Since the initial up-shift, peak narrowing, and monotonic shift in peak ratios are consistent with previous results [29, 76, 77, 78], we further conclude that we are indeed doping our graphene.

The sample that was baked after being doped to $E_F = 200$ meV exhibited full recovery. In fact, it down-shifted an additional 3.5 rel. cm^{-1} for the 2D band and an additional 1.87 rel. cm^{-1} for the G band beyond the undoped sample. Furthermore, the I(2D)/I(G) ratio increased to about 2.6. All of these changes imply extremely pristine graphene. Because graphene is very sensitive to surface adsorbents, including water in the atmosphere [29], it is very likely that baking after doping also removed the adsorbents that had accumulated on the graphene sheet in the time between initial sample preparation of the undoped sample and its measurement in Raman. This would account for the seeming increase in purity after doping and baking. As such, it is reasonable to conclude that this process is reversible.

In summary, then, graphene hole-doped by nitric acid shows decreased saturable loss as measured by differential transmission, shifted Fermi level as measured by spectrophotometry, and shifts in peak location and intensity ratios as measured by Raman spectroscopy. Furthermore, Raman spectral measurements indicate that this doping process is reversible and does not induce any defect in the carbon lattice. While it is true that the behavior of the Raman spectra we measured of graphene doped by nitric acid are not entirely consistent with previous measurements, they are consistent enough to lend them some credibility. Furthermore, the primary goal of these measurements was to corroborate evidence from differential transmission and spectrophotometry measurements indicating that the optical properties of graphene are tunable by chemical doping for application in mode-locked lasers. Our Raman spectra indicate that doping does not damage the lattice, that the process is reversible, and that doping is occurring. These results meet the goals of our study. However, since nitric acid is sometimes used to alter the conductivity of graphene [11], the behavior of its Raman spectrum under the effects of nitric acid certainly merits more study.

Chapter 6

Conclusions And Outlook

In the course of this work, the mechanisms of mode-locking, semiconductor physics, and Raman spectroscopy have been—at least superficially—established. By reproducing the work of Li et al. [63, 66, 67, 68], a method of generating graphene for ultrafast applications has been developed. By measuring the nonlinear absorption of graphene, its applications as a saturable absorber for ultrafast lasers have been explored. Furthermore, we have used spectrophotometry to measure changes in graphene's Fermi level due to chemical doping, and we have correlated these measurements to changes in the nonlinear behavior of graphene due to a shifted Fermi level. We have used Raman spectroscopy measurements to confirm that doping is occurring and that the doping process is both non-damaging and reversible. The differential transmission system used to measure graphene was presented at the annual meeting of the Four-Corners Section of the American Physical Society and won a prize for outstanding student poster. The poster and awards can be found in appendix D. The measurements of the doping of graphene were recently submitted for publication. The submission is in appendix E.

Although the growth process developed did not generate graphene with sufficiently high damage thresholds or sufficiently low saturation intensities/fluences for use as a saturable absorber comparable to SESAMs, it did bear fruit. It was a critical step in our development of other graphene-based optical devices and it enabled the study of the tunable optical properties of graphene by doping. This study of tunable optical properties served as a pilot study for—and a critical stepping-stone towards—a graphene-based ultrafast electro-optic modulator (EOM).

Because of graphene's linear dispersion near the Dirac point (i.e., the Dirac cones), it has been

demonstrated to be an extremely fast conductor and been found to carry very high-frequency electronic signals [12]. It is therefore possible to use electrostatic doping to adjust graphene's linear absorption very quickly and create an extremely high-frequency optical switch, thus constructing an ultrafast EOM. It is possible that a graphene-based EOM could react quickly enough to suppress Q-switching instabilities in a laser mode-locked by other means. Our optimization of CVD methods made the graphene for this system available, and our study of tunable optical properties by differential transmission, spectrophotometry, and Raman spectroscopy gave us the understanding to attempt building such a device.

Through the hard work and insight of Seiya Suzuki, Chien-Chung Lee, Wanyan Xie, and Prof. Thomas Schibli, a prototype of this EOM has been realized as a mirror structure (see Figure 6.1). The structure consists of a ring electrode on the surface of the mirror structure to apply a voltage across the graphene sheet. Below the graphene sheet, tantalum pentoxide (Ta_2O_5) is used as a transparent dielectric to supply the doping effect; beneath the Ta_2O_5, an aluminum bottom electrode acts as the mirror. The thickness of the dielectric layer is designed so that constructive interference produces a strong electric field at the graphene layer, amplifying its effect on the absorption of the device. At the time of writing, a device has been fabricated and tested for a laser with wavelength $\lambda = 1550$ nm. Figure 6.2 shows the device in action.

The device has been shown to have a modulation depth as large as 0.8% of the incident laser light over a large surface area and has been shown to function at frequencies as high as 10 MHz (frequency detection limited by measurement devices). Admittedly, 10 MHz is not ultrafast. However, with optimization, the device should eventually be able to function in the GHz or THz regime. To conclude, then, we may yet find applications for graphene in ultrafast mode-locked lasers.

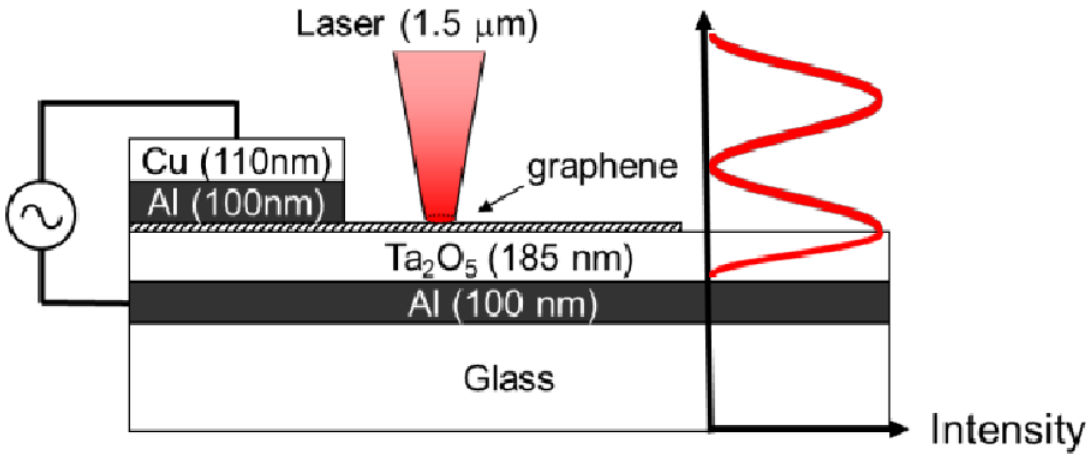

Figure 6.1: A schematic of a graphene-based electro-optic modulator.

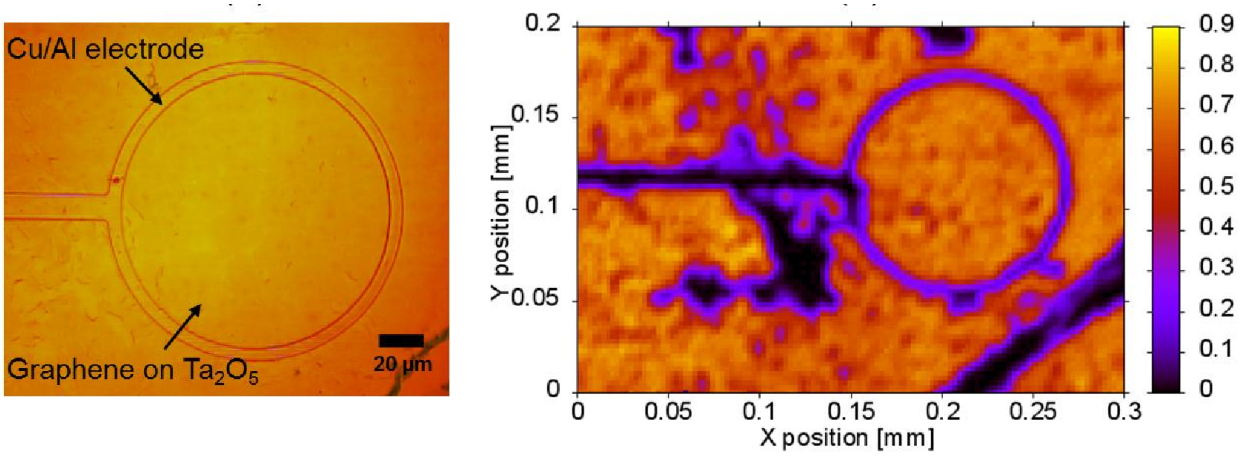

Figure 6.2: A graphene-based EOM prototype. Left: An optical image of the device showing the top ring electrode. Right: A two-dimensional scan of the device's modulation depth in percent. Scan is for the same device as shown on the left.

Appendix A

Final Graphene Growth Recipes and Transfer Method

A.1 Transfer Method

(1) From a sample of copper with graphene grown on it, carefully cut a roughly square piece, about the width of a microscope slide (preferably a little less wide than the slide). Place it on the center of a slide, graphene side up, and tape the edges so that the foil is as flat as possible.

(2) Pipette 3-4 drops of poly(methyl methacrylate) (PMMA)–or enough to cover the entire foil–onto the sample.

(3) Spin-coat the sample: Put on spinner for 120s. Set the spinner so that it measures 12,000 rpm. Acceleration is mostly irrelevant.

(4) Let PMMA cure on copper for about 12 hours. Keep it somewhere free of contamination.

(5) Make 0.5 M etchant: 27 g ferric chloride hexahydrate (Alfa Aesar) in 200 ml DI water. Assume that 1mL = 1g and measure DI water out by mass.

(6) With tweezers, place graphene/copper piece in etchant bath with PMMA side up.

(7) Wait and watch by eye. The copper will disappear, leaving graphene/PMMA floating on top of the used etchant. Samples typically take about 30 minutes for the copper to etch away.

(8) Transfer the released graphene to reactant grade DI water with a smooth plastic spoon and soak until the water changes color. A wide, high-volume container is best. Large volume is desirable

because a larger ratio of water picked up in the spoon to water in the container results in faster cleaning. Wide is desirable because this provides the maximum surface area of water, making it easier to move the graphene/PMMA with a spoon.

(9) Repeat as needed using a new water bath. When the water doesn't change color after 2 hours, transfer the graphene to spectrograph-grade DI water and wait for a minimum of five minutes.

(10) Transfer the graphene sample to a substrate: Scoop up the graphene with the substrate, and the graphene will stick so that it can be pulled out of the water, then carefully dry the substrate by dabbing the edges of the graphene sheet with a Kimwipe. Alternatively, transfer the graphene to the substrate via spoon: Lift the graphene from the water with the spoon, remove all but a small drop of water from the spoon by dabbing it with a Kimwipe, carefully pour the drop and the graphene onto the substrate, and remove the rest of the water from the substrate by dabbing with another Kimwipe. Substrate must be insoluble in water and in organic solvents.

(11) Wait about 12 hours to dry (again, away from contamination).

(12) Place substrate in chloroform bath at 60 C for 10 minutes.

(13) Gently rinse with acetone and methanol, in that order.

(14) Place substrate back in chloroform bath at 60 C for 10 minutes.

(15) Gently rinse again with acetone and methanol, in that order.

(16) Place substrate in ambient temperature IPA for 10 minutes.

(17) Gently rinse again with acetone and methanol, in that order.

(18) Gently blow dry with nitrogen gun.

A.2 Selected Recipes for Graphene Sheets and for Large Domain-Size Graphene Flakes.

A.2.1 Recipe for Graphene Sheets

Place the flattened copper foil in the reaction chamber, and lower the pressure to approximately 0 mTorr. Heat the chamber to approximately 1000°C, which takes approximately 1:10h. During the heat-up phase, expose the copper to a gas flow of 5 sccm of hydrogen, which raises the pressure to approximately 14 mTorr. After the target temperature is reached, allowed the copper to anneal in the same 5 sccm hydrogen flow for approximately 30m. After annealing, expose the copper to 1 sccm of hydrogen and 1 sccm of methane for approximately 30m. The pressure during the first growth phase is approximately 4 mTorr. After the first growth phase, expose the copper to 10 sccm of methane and 1 sccm of hydrogen for 5m. The pressure during this phase is approximately 20 mTorr. After the two growth phases, allow the copper to cool to room temperature under a gas flow of 1 sccm of hydrogen. Rapid cool-down can be effected by moving the sample out of the furnace immediately after the growth phase. Cool-down takes approximately 1h. After cool-down, turn the vacuum pump off and fill the reaction chamber with an argon atmosphere, with a flow rate of 50 sccm, to bring the pressure up to atmospheric normal.

A.2.2 Recipe for Large Domain-Size Graphene Flakes

Place the flattened copper foil in the reaction chamber, and lower the pressure to approximately 0 mTorr. Heat the chamber to approximately 1000°C, which takes approximately 1:10h. During the heat-up phase, expose the copper to a gas flow of 5 sccm of hydrogen, which raises the pressure to approximately 14 mTorr. After the target temperature is reached, allow the copper to anneal in the same 5 sccm hydrogen flow for approximately 30m. After annealing, expose the copper to 10 sccm of hydrogen and 0.2 sccm of methane for approximately 3h. The pressure during the growth phase is approximately 22 mTorr. After the growth phase, allow the copper to cool to room temperature under a gas flow of 1 sccm of hydrogen. Cool-down takes approximately 1h. Rapid cool-down can be effected by moving the sample out of the furnace immediately after the growth phase. After cool-down, turn the vacuum pump off and fill the reaction chamber with an

argon atmosphere, with a flow rate of 50 sccm, to bring the pressure up to atmospheric normal.

Appendix B

Calibration of the Home-Built Raman System

B.1 Y-Axis Calibration

Initial measurements on the Raman spectrum of graphene showed a strong background signal. It was thus necessary to determine if this background could safely be subtracted away to generate a clean signal. To determine whether the intensities on the spectrometer were accurate with or without this background signal, the spectrum of n-Hexane was measured and compared to the results of other groups. n-Hexane was chosen because it is a liquid, requiring little to no sample preparation that could cause inconsistency; because it has well-defined peaks in the same range as graphene; and because it is a well understood material that has been measured several times since the inception of Raman spectroscopy.

As a first guess, we subtracted the background from the n-Hexane measurements we made and compared the resulting spectrum to measurements made by the following sources: a product demonstration of a Newport spectrometer [80], the work of F.T. Cleveland and P. Porcelli [81], E.J. Rosenbaum et al. [82], V.S. Gorilek et al. [83], and the Raman/Infrared Atlas of Organic Compounds compiled by B. Schrader [84]. These sources were grouped into two categories: modern sources that made measurements with a modern CCD camera[1] and pre-CCD camera sources. Because absolute intensity means very little in Raman spectroscopy, the ratios of various obvious peaks in the spectrum were chosen for comparison. Figure B.1 shows the spectrum, with chosen peaks labeled. The names given to these peaks are completely arbitrary and do not reflect any convention.

[1] A CCD camera detects light by absorbing a photon in a semiconductor, thereby exciting a charge. This charge is caught in a potential difference and pulled into an amplifier in the camera, which reads the absorption as a pixel lighting up.

Figure B.2 shows the ratios of peak intensities for different measurements of n-Hexane grouped by the era in which they were performed. It compares our measurements to pre-CCD and post-CCD measurements. In every chosen ratio, our measurements are at approximately the mode value, implying that subtracting the background is the proper thing to do. Figure B.3 then shows the method by which we subtract our background for a specific graphene sample. Points that are part of peaks are first removed from the spectrum. A higher-order polynomial is then fitted to the remaining points. Finally, this polynomial is then subtracted from the original spectrum to produce a clean signal. This analysis can be performed in batches using the scripts written in appendix C.

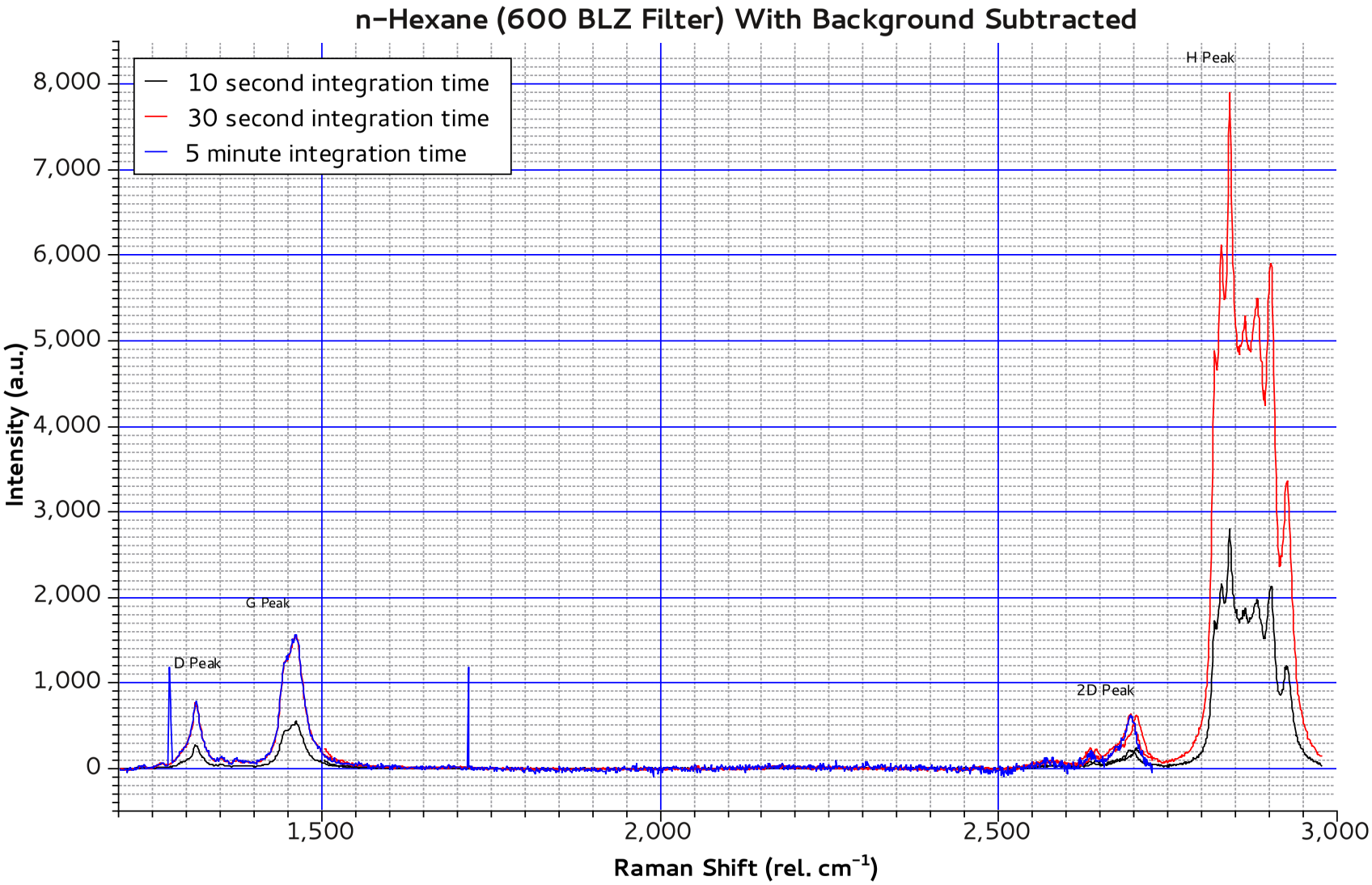

Figure B.1: The Raman spectrum of n-Hexane measured over different exposure times and with the salient peaks labeled. Because of their similarity in position to the peaks in graphene, the peaks at approximately 1300 rel. cm^{-1}, 1450 rel. cm^{-1}, and 2670 rel. cm^{-} were called the D, G, and 2D peaks respectively. The tallest peak at approximately 2800 rel. cm^{-1} was called the H peak.

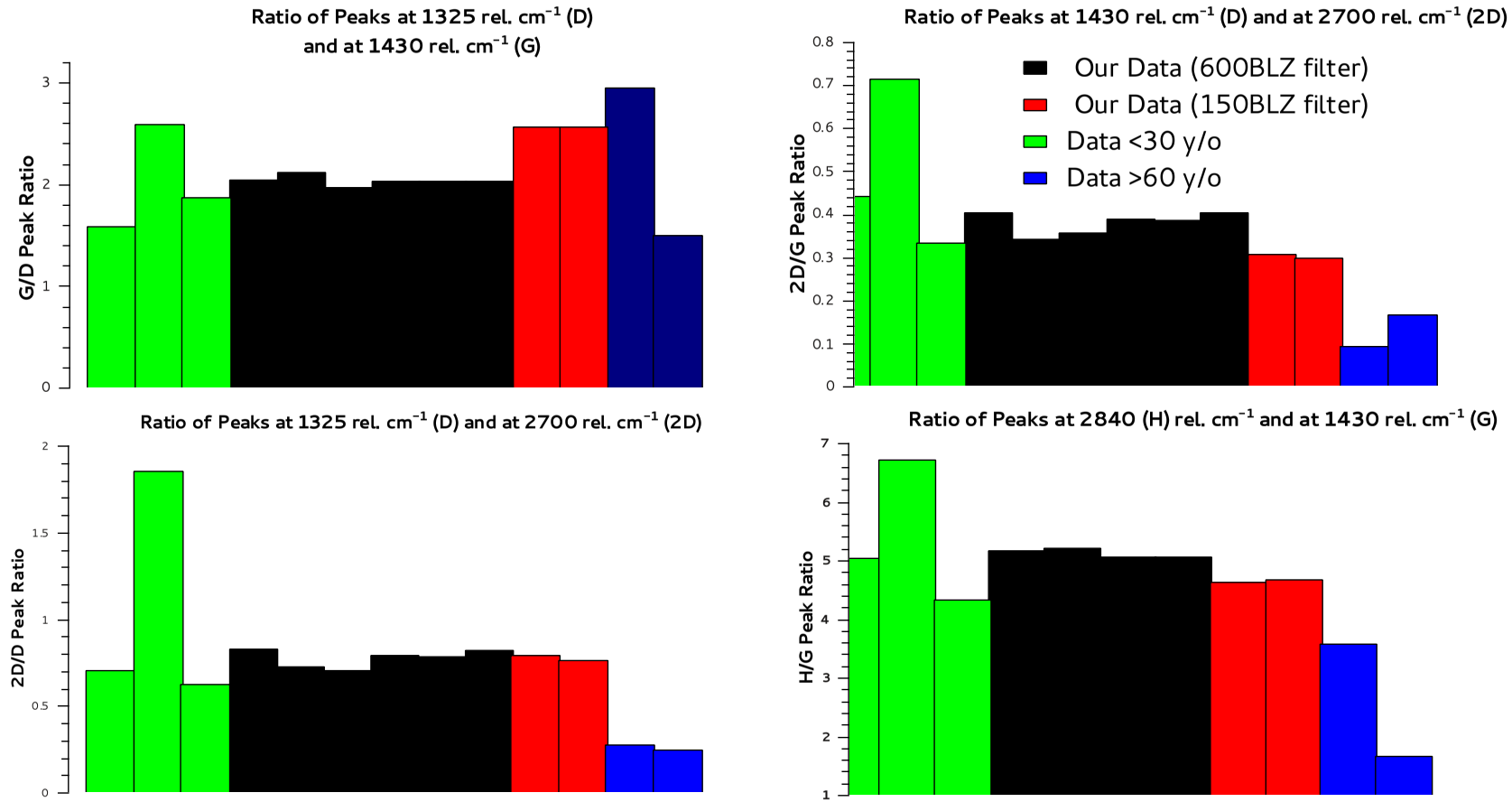

Figure B.2: Comparison of various measurements of ratios of intensities between peaks of n-Hexane. Black and red measurements are both ours. Black is data taken with a 600 BLZ diffraction grating, while red is data taken with a 150 BLZ diffraction grating.

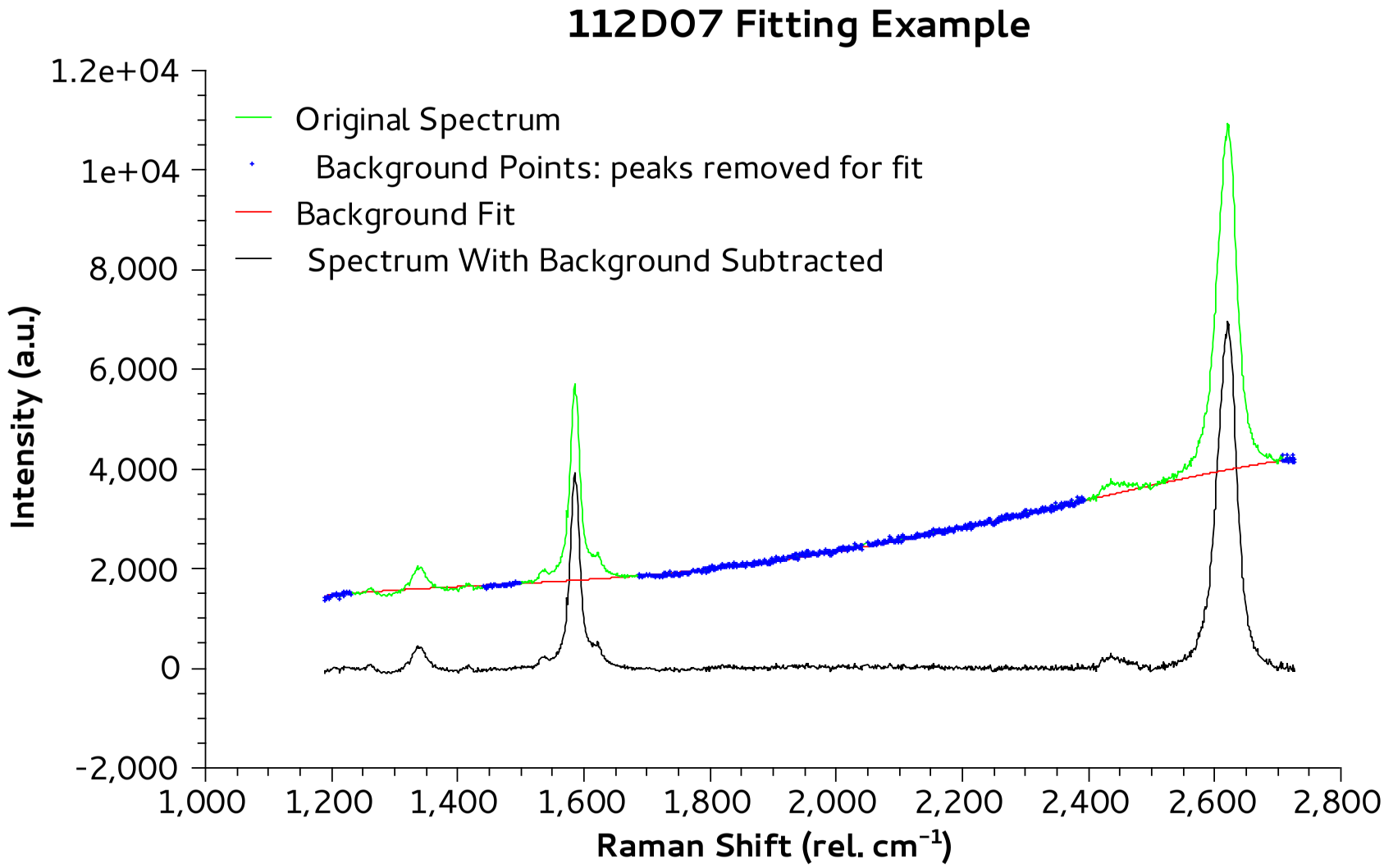

Figure B.3: An example of removing the background from a measurement of the Raman spectrum of graphene. Points that are part of peaks are first removed from the spectrum. A higher-order polynomial is then fitted to the remaining points, and subtracted from the original spectrum to produce a clean signal.

B.2 X-Axis Calibration

There was later found to be an error in the wavelength values measured by the Raman system. To correct for this, emission lines from a neon gas lamp were used to correlate measured wavelength values to actual wavelength values. Measurements of the neon lamp were performed by Doctor Joanna Atkin. For the sake of completeness, these measurements are presented here. All plots and tables relating to x-axis calibration by neon lamp were generated by Doctor Joanna Atkin.

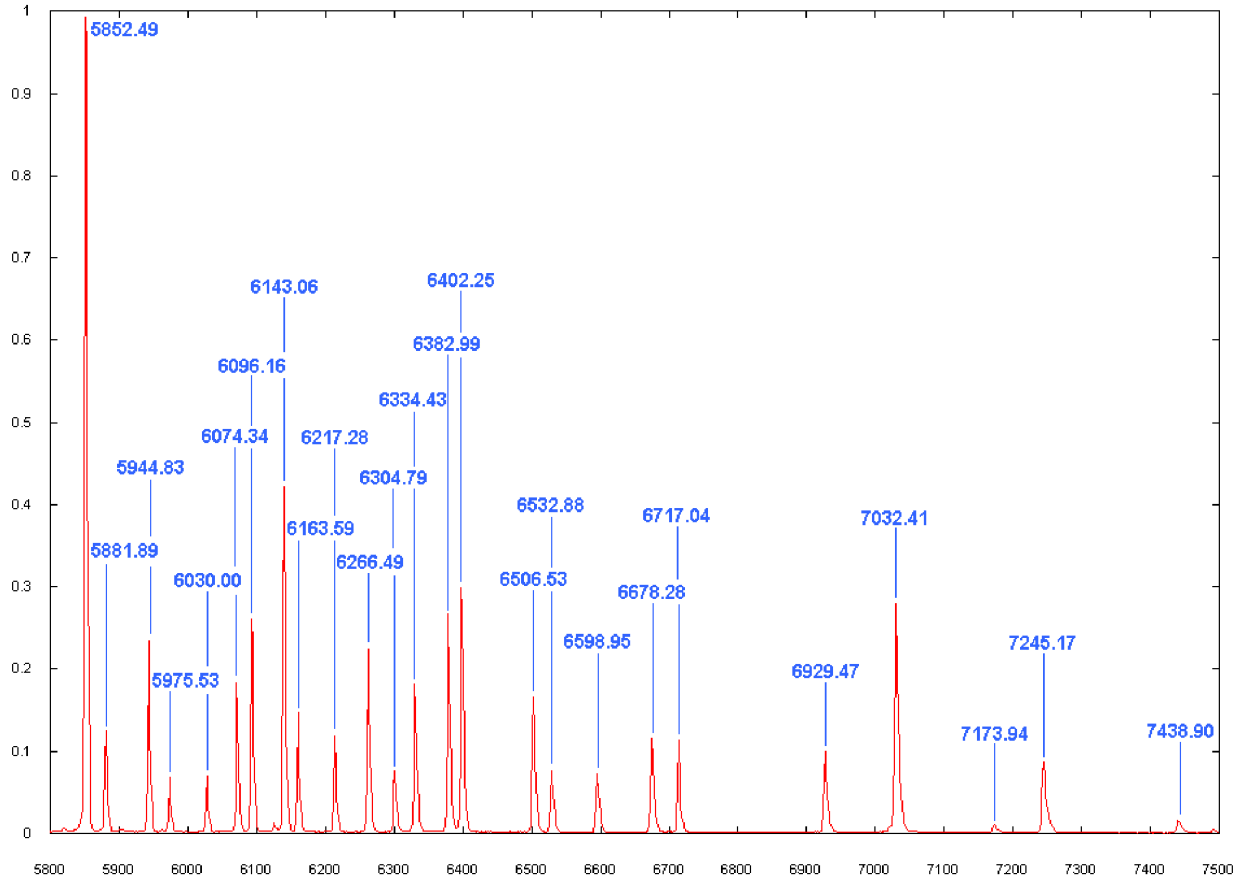

Figure B.4: The known spectrum of neon. These lines were measured to calibrate the x-axis of the spectrometer. Intensities are normalized to unity.

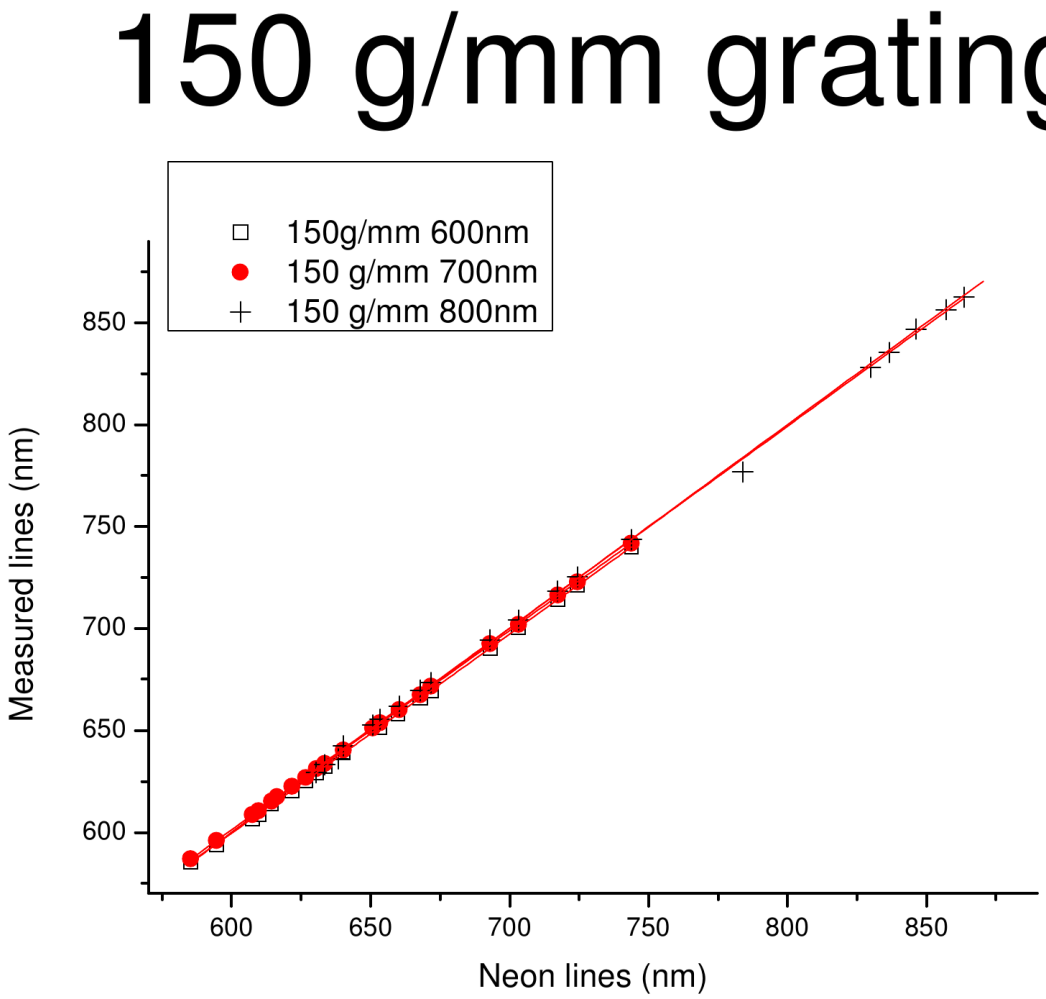

nm	y-int	err	slope	err
600	13.20354	0.66555	0.9771	0.00102
700	14.78873	0.82813	0.97732	0.00127
800	7.3695	4.09278	0.98976	0.00563

Figure B.5: Plot: Measured wavelength as a function of actual wavelength for the 150BLZ grating. Different sets of points in the legend represent different center wavelengths of the grating as adjusted by a motor in the spectrometer. Table: Linear fits based on center wavelengths. “y-int” refers to y-intercept. “err” refers to fit error by least squares fitting.

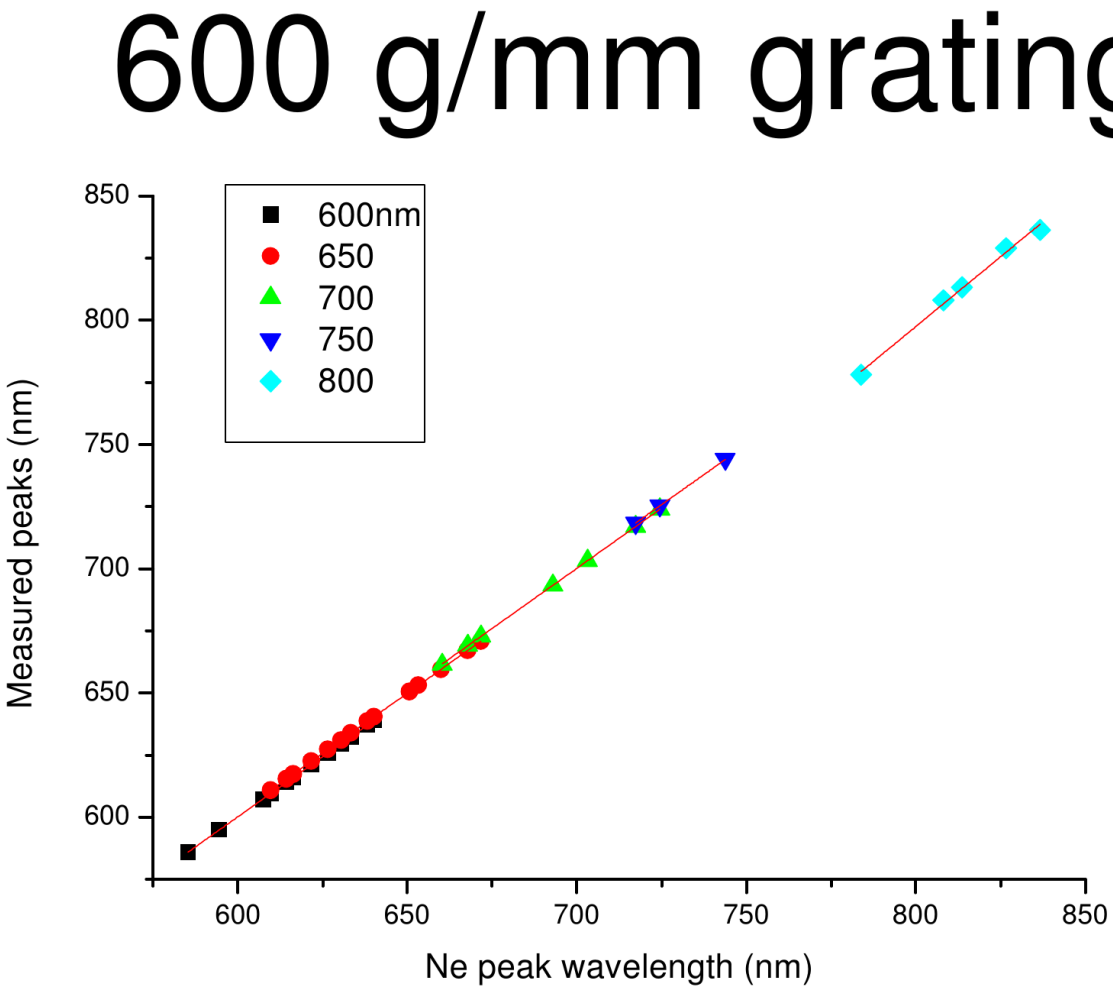

nm	y-int	err	slope	err
600	25.36849	1.3227	0.96607	0.00182
650	-100.82342	38.94648	1.12284	0.04785
700	20.67779	0.52221	0.96574	8.44E-4
750	21.28843	0.28425	0.96704	4.452E-4
800	21.91977	1.51005	0.96888	0.00218

Figure B.6: Plot: Measured wavelength as a function of actual wavelength for the 600BLZ grating. Different sets of points in the legend represent different center wavelengths of the grating as adjusted by a motor in the spectrometer. Table: Linear fits based on center wavelengths. "y-int" refers to y-intercept. "err" refers to fit error by least squares fitting.

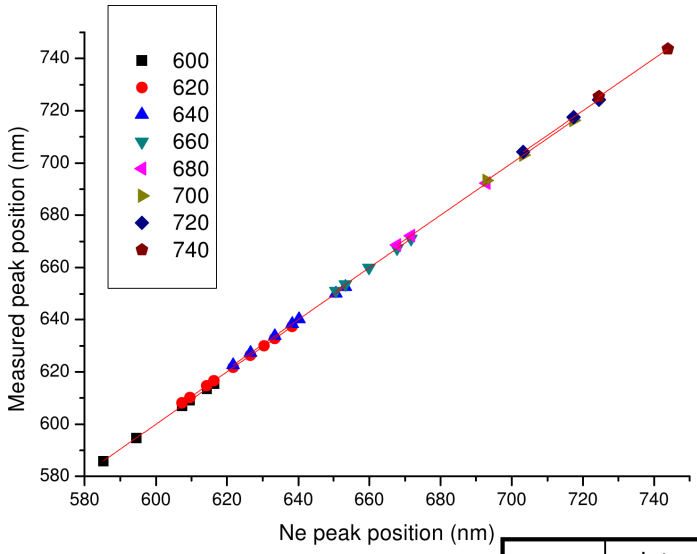

nm	y-int	err	slope	err
600	29.84448	0.25058	0.9501	4.144E-4
620	32.17773	0.23099	0.94816	3.713E-4
640	33.47419	0.39073	0.94765	6.126E-4
660	36.13659	0.34418	0.94519	5.210E-4
680	38.35243	0.6073	0.94367	8.963E-4
700	41.08542	0.05285	0.94124	7.500E-5
720	41.02096	0.07158	0.94306	1.001E-4
740	44.2601		0.94022	

Figure B.7: Plot: Measured wavelength as a function of actual wavelength for the holographic grating, which is 1200BLZ. Different sets of points in the legend represent different center wavelengths of the grating as adjusted by a motor in the spectrometer. Table: Linear fits based on center wavelengths. “y-int” refers to y-intercept. “err” refers to fit error by least squares fitting.

Appendix C

Python Scripts Used to Analyze Raman Data

The following scripts were written for the Python interpreter[1] to batch analyze large quantities of Raman measurements. They are called by command line[2] on any number of files in the filesystem. To be most effective, the operating system they are used in needs to support globbing.[3] Python was chosen because its intuitive syntax is flexible and easy to learn and because a substantial number of packages for advanced mathematics, matrices, numerical analysis, and plotting have been developed in the C programming language[4] by the teams for Scipy [85] and Matplotlib [86]. These libraries can be called with the import command. Because the relevant algorithms were written in C and Python merely glues them together, Python is faster and less resource-intensive than other interpreted languages. Incidentally, although the author did not know at the time of research, there is an entire library of Python code devoted to spectrum analysis called Peak-O-Mat [87].

[1] Python is an interpreted language as opposed to a compiled one. A program called the interpreter reads every human-readable Python script—contained in an ASCII text file—and executes the commands in it in order.

[2] The command line is the text-based interface underneath most operating systems. Examples include MSDOS for Microsoft Windows, Unix for Apple's MacOS, and the Linux kernel for any Linux-based operating system.

[3] Globbing refers to a command structure where a command is called for a number of arguments at once, rather than calling them one at a time. This is a great time-saver for whomever calls the command.

[4] C is an extremely popular compiled language. A human-readable program is written in an ASCII text file and a program called a "compiler" takes this text file and converts it into assembly, which the computer's firmware can read.

C.1 rayleigh.py: The Offset Calculator

The Raman spectrometer used to make measurements uses a diffraction grating to generate scattered spectra. However, this grating cannot cover the entire wavelength range the spectrometer can measure, so it must move in order to cover the whole range. To generate a mean and variance for the offset caused by any inconsistency in this motion, the first-order Rayleigh-scattered light[5] was measured at approximately 630 nm after every measurement. The rayleigh.py program takes a number data files containing lists of wavelengths and intensities measuring the Rayleigh scattering, extracts the wavelength corresponding to the peak intensity in each file, and takes the mean and standard deviation. It then generates a new data file with this information in it.

————- BEGIN PYTHON SCRIPT ————-

```
#!/usr/bin/env python
#The above line tells the unix/linux shell where the python interpreter is.

#By Jonah Miller
#This program goes through Rayleigh line data and finds the mean shift
#in nanometers and the standard deviation

import sys, os
import numpy as np
import scipy as sp
import scipy.optimize as op
import time

ray = []
```

[5] Most Rayleigh-scattered light is filtered away, but some passes through the filter and can be measured on the spectrometer.

```
filenames = []

line = 633


#The function to convert wavelength (nm) to Raman Shift (cm^-1)

def rs(wavelength,laser):

    return ((float(1)/laser)-(float(1)/wavelength))*(10**7)


def main(argv): #Goes through a file and finds the peak position of the rayleigh line

    f = np.loadtxt(argv).transpose() #Opens the file

    maxi = np.amax(f[1]) #Finds the value of hte peak of the Rayleigh line

    intensity = [f[1,i] for i in range(len(f[1]))] #Extracts the array into a list

    indi = intensity.index(maxi) #Finds the index of the Rayleigh line

    ray.append(f[0,indi])

    filenames.append(str(argv))


#Executes the main subroutine

for filename in sys.argv[1:]:

    main(filename)


#Calculates the mean, variance, and standard deviation

#in wavelength (nm).

mean = np.mean(ray)

StandardDeviation = np.std(ray)

median = np.median(ray)

variance = np.var(ray)

#in raman shift (rel. cm^-1)

ramanshift = [rs(ray[i],line) for i in range(len(ray))]
```

```
rsmean = np.mean(ramanshift)

rsSD = np.std(ramanshift)

rsmedian = np.median(ramanshift)

rsvariance = np.var(ramanshift)


#Time of program call

tname = str(time.asctime())


#Output

output = open('rayleigh_'+tname+'.dat','w')

output.write('#The files used for this compilation are:\n')

for i in range(len(filenames)):

    output.write('#'+filenames[i]+'\n')

output.write('The wavelengths of the Rayleigh line are (in nm):\n')

for i in range(len(ray)):

    output.write(str(ray[i])+'\n')

output.write('The raman shifts of the rayleigh line for '+str(line)+'nm are (in rel. cm^(-1):\n')

for i in range(len(ray)):

    output.write(str(ramanshift[i])+'\n')

output.write('Mean = '+str(mean)+'nm, or '+str(rsmean)+' rel. cm^(-1)\n')

output.write('Standard Deviation = '+str(StandardDeviation)+' nm, or '+str(rsSD)+' rel. cm^(-1)\n')

output.write('Median = '+str(median)+'nm or, '+str(rsmedian)+' rel. cm^(-1)\n')

output.write('Variance = '+str(variance)+'nm or, '+str(rsvariance)+' rel. cm^(-1)\n')

output.close()
```

———— END PYTHON SCRIPT ————

C.2 RamanRecalibration.py: Batch Data Preparation For The Holographic Grating

The holographic grating on the Raman Spectrometer offers extremely high wavelength resolution, but has a small range over which a spectrum can be viewed in a single measurement: only wide enough to view the D and G peaks *or* the 2D peak of graphene. This grating was used to measure the peak-shift of doped graphene, while the 600BLZ grating (discussed below) was used to measure the change in peak ratios of aforementioned doped graphene. Unfortunately, the holographic grating had some x-axis calibration issues and a linear tilt in the background signal. The RamanRecalibration.py program recalibrates the x-axis properly, removes the linear tilt, removes cosmic events which deviate dramatically from a rolling mean/variance, normalizes all peaks so that a single spectrum ranges from 0 to 1 in intensity, and shifts the x-axis from nanometers to relative wavenumbers (rel. cm^{-1}). A new file is then generated with the data points for the analyzed data.

————- BEGIN PYTHON SCRIPT ————-

```
#!/usr/bin/env python
#The above line tells the unix/linux shell where to find the python interpreter

#By Jonah Miller
#This program goes through Raman Data, finds cosmic events, and removes them.
#It also crudely normalizes the curve so that intensities range from 0 to 1.
#If there is a strong background tilt, the renormalization will fail.
#This should be used for small spectral widths.

import sys, os
```

```
import numpy as np
import scipy as sp
import scipy.optimize as op
import sys

#Calibration data. For a line, y=mx+b of measured value as a function of actual value for x-axis
#Of the form [(range minimum, range maximum),Y-intercept,error,slope]
calidat =[[(600.0001,620),29.84448,0.25058,0.9501],
          [(620.0001,640),32.17773,0.23099,0.94816],
          [(640.0001,660),33,47419,0.39073,0.94765],
          [(660.0001,680),36.13659,0.34418,0.94519],
          [(680.0001,700),38.35243,0.6073,0.94367],
          [(700.0001,720),41.08542,0.05285,0.94124],
          [(720.0001,740),41.02096,0.07158,0.94306],
          [(740.0001,8000),44.2601,1,0.94022]]

ray = 632.792 #The position of the Rayleigh scattering line. This is assumed to be the laserline.
laserline = np.array([[ray],[1337]]) #For the purposes of fitting into the calibration function

#Calibrates the x-axis
def calibrate(dataset,calibration):
    xax = []
    for i in range(len(calibration)):
        segment = [dataset[0,j] for j in range(len(dataset[0]))
                   if calibration[i][0][0] < dataset[0,j] < calibration[i][0][1]]
        segment = [(segment[j]-calibration[i][1])/calibration[i][-1] for j in range(len(segment))]
        xax = xax+segment
```

```
    return np.array([xax,dataset[1]])


#The Raman shift equation
def shift(ls,x):
    return ((1./float(ls))-(1./(float(x))))*(10**7)


#Calibrates the Rayleigh line as well
laserline = calibrate(laserline,calidat)
laserline = laserline[0,0]


#The primary subroutine
def main(argv):
    #Gets the data out of an ascii file. It is retrieved as an array in two collumns of data.
    f = np.loadtxt(argv)
    d = f.transpose() #Takes the transpose of the array


    #Replaces the x-axis with a Raman shift from the laser line specified
    d = calibrate(d,calidat)


    #Converts everything to a raman shift.
    rshift = []
    for i in range(len(d[0])):
        rshift.append(shift(laserline,d[0,i]))
    d = np.array([rshift,d[1]])


    #Deletes points that vary from the mean by too much
    def prune(numbers,width,tolerance):
```

```
    anomalous = np.zeros(len(numbers[0]))
    for i in range(width,len(numbers[0])-width):
        temp = [numbers[1,j] for j in range(i-width,i+width)]
        test.append(temp)
        mean = np.median(temp)
        variance = np.std(temp)
        if numbers[1,i] >= mean+variance*tolerance:
            anomalous[i]=1
    intensity = [numbers[1,k] for k in range(len(numbers[0]))]
    rs = [numbers[0,i] for i in range(len(numbers[0]))]
    for l in range(len(rshift)):
        if anomalous[l] == 1:
            intensity[l] = 'badpoint'
            rs[l] = 'badpoint'
    while intensity.count('badpoint') != 0:
        intensity.remove('badpoint')
    while rs.count('badpoint') !=0:
        rs.remove('badpoint')
    return np.array([rs,intensity],float)


#Prunes an array of data of any points "tolerance"
#standard deviations away from a rolling mean of radius "width"
processed = prune(d,7,2)
processed = prune(processed,7,2)


#Makes the plot go from 0 to 1
lhsy = [processed[1,i] for i in range(0,5)]
```

```
    rhsy = [processed[1,-i] for i in range(0,5)]
    lhsx = [processed[0,i] for i in range(0,5)]
    rhsx = [processed[0,-i] for i in range(0,5)]

    #Finds the linear tilt
    m = (np.median(rhsy)-np.median(lhsy))/(np.median(rhsx)-np.median(lhsx))
    processed[1] = processed[1] - (m*processed[0]) #Removes any linear tilt
    processed[1] = processed[1]-np.amin(processed[1]) #Subtracts away the DC background
    processed[1] = processed[1]/np.amax(processed[1]) #Normalizes the function




    #Output
    dname = 'Recalibrated_'+str(ray)[:3]
    a = os.access(dname,1)
    if a == False:
        os.mkdir(dname) #Creates a new directory for the output files
    outputfile = open(dname+'/'+argv.rstrip('.dat')+'_'+dname+'.dat','w')

    for i in range(len(processed[0])):
        outputfile.write('%s %s\n' % (processed[0,i], processed[1,i]))

    outputfile.close()



for filename in sys.argv[1:]:
    main(filename)
```

————- END PYTHON SCRIPT ————-

C.3 raman_fs.py: Batch Data Preparation for the 600BLZ Grating

The 600BLZ grating can view a wide enough spectrum that the entire relevant Raman spectrum of graphene is visible. It has no x-axis calibration error. However, it does have a strong background signal that behaves like part of a higher-order polynomial. Calibration efforts showed that this polynomial can be subtracted from the desired signal without error (see Appendix B). The raman_fs.py program converts a wavelength-based spectrum into the wavenumber (rel. cm^{-1}) domain. It then removes cosmic events which deviate dramatically from a rolling mean/variance. Then it removes the background curve by generating a set of data points that contain only background information, fitting a polynomial to this data, and then subtracting the fit from the original spectrum. Finally, the plot is normalized so that the intensity of the spectrum ranges from 0 to 1. A new file is then generated with the data points for the analyzed data.

———— BEGIN PYTHON SCRIPT ————

```
#!/usr/bin/env python
#The above line tells the unix/linux shell where the python interpreter is.


"""
By Jonah Miller
This program goes through Raman Data, finds cosmic events, and removes them.
It also crudely normalizes the curve so that intensities range from 0 to 1.
If the background peaks are not in the expected places,
or if the background is not approximatable by a higher order polynomial,
this normalization will fail.
This should be used for wide spectral widths of graphene.
```

```
It can't be used for anything else,
but it is possible to edit the scipt to work for other spectra.
"""

import sys, os
import numpy as np
import scipy as sp
import scipy.optimize as op
import sys

def polynomial(x,a0,a1,a2,a3,a4): #A 4th degree polynomial
    return a0+a1*x+a2*(x**2)+a3*(x**3)+a4*(x**4)

#Generates a background dataset from a spectrum so that this
#background can be fitted to and then subtracted later
def background(spectrum,peakbounds):
    #Generates a copy of the spectrum to play with so that the original is unchanged
    copy = [[i for i in spectrum[0]],[i for i in spectrum[1]]]
    #Generates a list of lists of the x-values where the peaks might be
    peaks = [[i for i in copy[0] if j[0]<=i<=j[1]] for j in peakbounds]
    points = []
    for i in range(len(peaks)):
        points.extend(peaks[i])
    #The indices of each x value in the range of a specific peak
    locations = [copy[0].index(i) for i in points]
    #Marks each point in a peak by setting it as a "not a number"
    #value 'peakpoint' for removal later
```

```
    for i in locations:
        copy[0][i] = 'peakpoint'
        copy[1][i] = 'peakpoint'
    while copy[0].count('peakpoint') != 0: #Removes the marked points
        copy[0].remove('peakpoint')
    while copy[1].count('peakpoint') != 0:
        copy[1].remove('peakpoint')
    return np.array([copy[0],copy[1]])


def shift(ls,of,x):
    return ((1./float(ls))-(1./(float(x)+of)))*(10**7)


#Some important values
laserline = 633 #The laser exciting the raman scattering in nanometers
ray = 632.7555 #The position of the rayleigh scattering line
#The amount the x-axis must be shifted to place the rayleigh scattering line at 0 rel. cm^(-1)
offset = 633-ray


Dlhs = 1331 #The estimated beginning of whatever D peak there might be.
Drhs = 1377 #The estimated end of whatever D peak there might be.
mp1lhs = 1435 #The estimated beginning of the first mystery peak
mp1rhs = 1486 #The estimated end of the first mystery peak
Glhs = 1525 #The estimated beginning of the second mystery peak and the G peak
Grhs  = 1650 #The estimated end of the G Peak
mp2lhs = 2074 #The estimated beginning of the 3rd mystery peak
mp2rhs = 2116 #The estimated end of the 3rd mystery peak
GPlhs = 2413 #The estimated beginning of the G* and G prime peaks
```

```
GPrhs = 2689 #The estimated end of the G prime peak and mystery peak after it

#A list of the peak locations as ordered pairs for the background

peaklist = [[Dlhs,Drhs],[mp1lhs,mp1rhs],[Glhs,Grhs],[mp2lhs,mp2rhs],[GPlhs,GPrhs]]


def main(argv):

    f = np.loadtxt(argv)

    d = f.transpose()


    rshift = []


    #Replaces the x-axis with a raman shift from the laser line specified

    for i in range(len(d[0])):

        rshift.append(shift(laserline,offset,d[0,i]))


    #Deletes points that vary from the mean by too much

    def prune(numbers,width,tolerance):

        anomalous = np.zeros(len(numbers[0]))

        test = [] #This is here for debugging

        for i in range(width,len(numbers[0])-width):

            temp = [numbers[1,j] for j in range(i-width,i+width)]

            test.append(temp)

            mean = np.median(temp)

            variance = np.std(temp)

            if numbers[1,i] >= mean+variance*tolerance:

                anomalous[i]=1

        intensity = [numbers[1,k] for k in range(len(numbers[0]))]

        rs = [numbers[0,k] for k in range(len(numbers[0]))]
```

```
    for l in range(len(rshift)):
        if anomalous[l] == 1:
            intensity[l] = 'badpoint'
            rs[l] = 'badpoint'
    while intensity.count('badpoint') != 0:
        intensity.remove('badpoint')
    while rs.count('badpoint') !=0:
        rs.remove('badpoint')
    return np.array([rs,intensity,xerr],float)

#Prunes an array of data of any points "tolerance"
#standard deviations away from a rolling mean of radius "width"
processed = prune(d,7,2)
processed = prune(processed,7,2)

nopeaks = background(processed,peaklist) #See above. removes the peaks for fitting

#Fits the background to a 4th degree polynomial
fitted = op.curve_fit(polynomial,nopeaks[0],nopeaks[1]) #The output of the curve fit
param = fitted[0] #The fitted variables

#Makes the plot go from zero to 1
#Subtracts the background from the main data-set.
processed[1] = processed[1]-polynomial(processed[0],
                                       param[0],param[1],param[2],param[3],param[4])
processed[1] = processed[1]/np.amax(processed[1]) #Normalizes the function
```

```
    #Output
    dname = 'fullspectrum'+str(laserline)
    a = os.access(dname,1)
    if a == False:
        os.mkdir(dname) #creates a new directory for the output files
    outputfile = open(dname+'/'+argv.rstrip('.dat')+'_'+dname+'.dat','w')

    for i in range(len(rs)):
        outputfile.write('%s %s\n' % (processed[0,i], processed[1,i]))
    outputfile.close()



for filename in sys.argv[1:]:
    main(filename)
```

———— END PYTHON SCRIPT ————

C.4 LorentzFit.py: Batch-Fitting Curves to Raman Spectra

Before much useful data from Raman spectra can be reliably extracted, each peak in the spectrum must be fitted to a curve, usually a single Lorentzian. However, since between six and fourteen peaks are measured per sample, it is highly desirable to automate this peak-fitting process. The LorentzFit.py program automatically fits peaks measured by the holographic grating. A similar program could be written for measurements made by the 600BLZ grating.

————- BEGIN PYTHON SCRIPT ————-

```
#!/usr/bin/env python

#By Jonah Miller
#This program plots raman data for graphene and fits a peak to a Lorentzian.
#It then plots them, allows for confirmation, and then compiles all parameters
#into a datafile to be read by a spreadsheet program.
#One should only use this for single lorentzian peaks.


#Imports the modules needed. sys and os manipulate
#the filesystem and interact with bash.
#Numpy enables array/matrix routines and statistical routines.
#Scipy contains the optimization routines.
#Matplotlib is for ensuring each fit works by a brief plot.
import sys, os
import numpy as np
```

```
import scipy as sp

import matplotlib as mpl

import matplotlib.pyplot as plt

import scipy.optimize as op


#The domain that should be fitted for the G peak and the 2D peak.

#Of the form [[Gmin,Gmax],[2Dmin,2Dmax]]

ranges = [[1532.3,1592],

          [2550,2750]]

#The initial guess for a DC offset of the lorentzian.

#Of the form [G peak guess, 2D peak guess]

Yintercept = [-1,-1]

#The initial guess for a linear slope superimposed on the lorentzian.

#Of the form [G peak guess, 2D peak guess]

LinearSlope = [1,0]

#The initial guess for the amplitude of the lorentian.

#Of the form [G peak guess, 2D peak guess]

LorentzianAmplitude = [20,50]

#The initial guess for the width of the lorentzian.

#Of the form [G peak guess, 2D peak guess]

LorentzianWidth = [12,30]


#Data that will be used for output later

fitparams = [[],[],[],[],[]] #This will later become a matrix of fitted parameters


#Lorentzian function definition

def lorentz(x,x0,y0,m,w,A):
```

```
    return float(y0)+2.*(float(A)/np.pi)*(float(w)/(4.*(x-float(x0))**2+float(w)**2))+(float(m)*x)


#The primary routine
def main(argv):
    #Opens the file
    d = np.loadtxt(argv).transpose()

    #Makes lists out of the array for certain data analysis purposes
    xvalues = [d[0,i] for i in range(len(d[0]))]
    yvalues = [d[1,i] for i in range(len(d[0]))]

    #Guesses at the possible parameters for a lorentzian fit and puts them in a list
    maxi = np.amax(d[1]) #The maximum raman intensity. Guessed as the center frequency.
    indi = yvalues.index(maxi) #The index the maximum value is at
    center = xvalues[indi] #The center of the maximum value. Guessed as the center frequency.

    segment = []

    #Uses the center frequency of the lorentzian peak to decide whether
    #to use the range for the G peak or for the 2D peak.
    #Then sets it.
    if ranges[0][0] < center < ranges[0][1]:
        segment = [d[0,i] for i in range(len(d[0])) if ranges[0][0] < d[0,i] < ranges[0][1]]
        yint = Yintercept[0]
        slope = LinearSlope[0]
        amp = LorentzianAmplitude[0]
        width = LorentzianWidth[0]
```

```
if ranges[1][0] < center < ranges[1][1]:
    segment = [d[0,i] for i in range(len(d[0])) if ranges[1][0] < d[0,i] < ranges[1][1]]
    yint = Yintercept[1]
    slope = LinearSlope[1]
    amp = LorentzianAmplitude[1]
    width = LorentzianWidth[1]
#This is a contingency, in case the center of the peak is not in the
#domains defined at the beginning of the program.
if len(segment)==0:
    segment = [d[0,i] for i in range(len(d[0]))]
    yint = (Yintercept[0]+Yintercept[1])/2
    slope = (LinearSlope[0]+LinearSlope[1])/2
    amp = (LorentzianAmplitude[0]+LorentzianAmplitude[1])/2
    width = (LorentzianWidth[0]+LorentzianWidth[1])/2
    #An alert that something went wrong.
    print "I don't know what kind of peak this is, but I'll do my best to make it work."

#Produces the date to be sent to the curve-fit
#Produces a y-axis for x-axis segment
intensity = [d[1,i] for i in range(len(d[0])) if segment[0] <= d[0,i] <= segment[-1]]
peak = np.array([segment,intensity]) #Combines the axes into a numpy array
guesses = [center,yint,slope,width,amp] #Sets the initial guesses for the fit, p0.

#Fits peak to a lorentzian using the set parameters
#popt is the optimized parameter set, given in the same order as guesses, pcov is covariance
popt, pcov = op.curve_fit(lorentz,peak[0],peak[1],p0=guesses,sigma=None)
```

```
    #Generates set of points for the fitted curve
    segmentfit = np.array(segment) #makes the x-axis an array so it can be parsed by the function
    intensityfit = lorentz(segmentfit,popt[0],popt[1],popt[2],popt[3],popt[4])
    peakfit = [segmentfit,intensityfit]

    #Generates a plot to compare the original data to the fit curve
    data = [plt.plot(d[0],d[1],'bo',ms=2.5,label='raw data'),
            plt.plot(peakfit[0],peakfit[1],'r-',label='fitted data')]
    plt.xlabel('Raman Shift (cm$^{-1}$)')
    plt.ylabel('Intensity (a.u.)')
    plt.title(str(argv))
    plt.show()

    return popt


#The actual operations performed
description = raw_input('Sample description? ') #Notes for the filename
fname = description+'_lorentzian_peak_fits.dat' #The filename

#Generates a list of fitted parameters
for filename in sys.argv[1:]:
    fitdat = main(filename)
    for i in range(len(fitdat)):
        fitparams[i].append(fitdat[i])

#Generates statistics on the data
```

```
#Generates an array of fitparams in a way that makes them easier to do statistics on
fitarray = np.array([fitparams[i] for i in range(len(fitparams))])
means = np.mean(fitarray,1) #The mean values
stdevs = np.std(fitarray,1) #The standard deviations


#Output
with open(fname,'w') as f:
    f.write('Last rows are mean values and standard deviations.\n')
    f.write('#Center-Frequency   DC-Offset   linear-Slope  Peak-Width Peak-Amplitude\n')
    for i in range(len(fitparams[0])):
        f.write('{0:17} {1:17} {2:17} {3:17} {4:17}\n'.format(fitparams[0][i],
        fitparams[1][i],fitparams[2][i],fitparams[3][i],fitparams[4][i]).rjust(17))
    f.write('{0:17} {1:17} {2:17} {3:17} {4:17}\n'.format(means[0], means[1],
        means[2], means[3], means[4]).rjust(17))
    f.write('{0:17} {1:17} {2:17} {3:17} {4:17}'.format(stdevs[0], stdevs[1],
        stdevs[2], stdevs[3], stdevs[4]).rjust(17))
```

———— END PYTHON SCRIPT ————

Appendix D

Conference Poster and Awards

The following pages show a poster presented at the annual meeting of the Four Corners Section of the American Physical Society in 2010.

A Systematic Study of Techniques to Directly Measure the Saturable Absorption of Graphene

SCHIBLI LAB
WE MAKE LIGHT SHINE

J. M. Miller, C.-C. Lee, T. R. Schibli, Department of Physics
jonah.miller@colorado.edu, http://spot.colorado.edu/~trs/

Colorado
University of Colorado at Boulder

Motivation

Graphene's electrical and mechanical properties have been well explored. However, there are many as of yet untapped applications for this novel material. For instance, to take advantage of graphene's potential as a saturable optical absorber, it is absolutely essential to characterize its optical properties precisely.

Saturable absorber

Saturable absorption of graphene

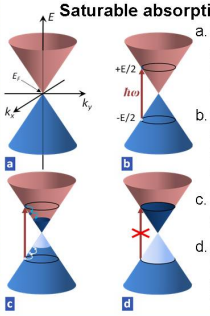

a. Low energy spectrum of graphene. Blue: valence band; Red: conduction band.

b. Absorption of a photon with $E_{photon} = \hbar\omega$. The vertical arrow indicates an inter-band transition.

c. Thermalization of photo-generated carriers.

d. At high optical intensities, the photo-generated carriers block further absorption.

Balanced Detection

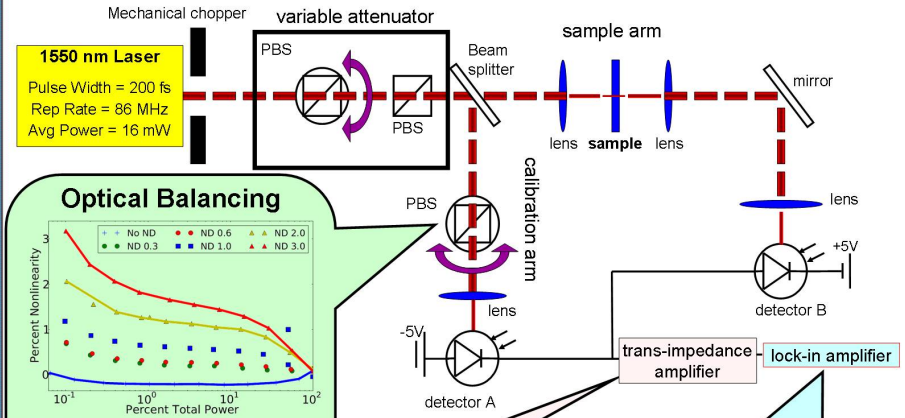

Optical Balancing

Optical attenuation through absorption causes thermal lensing. Hence, non-absorptive components are required.

The Results

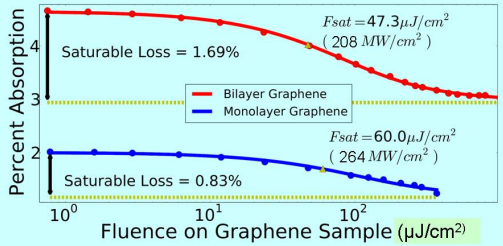

With attention to all sources of systematic error, this technique can measure nonlinear absorption to an accuracy better than 0.1% after calibration over a dynamic range of over three orders of magnitude.

Maintaining the Dynamic Range

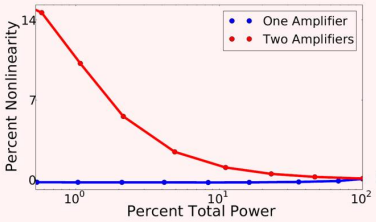

A significant source of nonlinearity comes from the electronics themselves. The differences between two supposedly identical amplifiers can cause large variations over a dynamic range of three orders of magnitude. Instead one should electrically subtract the signals from the two photo detectors and amplify the subtracted signal with a single amplifier.

The Idea

Nonlinear absorption can be small. To measure it over a large dynamic range can be very difficult. Balanced Detection offers a solution while reducing the noise[1,2].

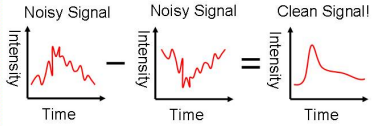

Balanced detection removes common-mode noise from the signal. In our specific case, one detector measures the optical absorption signal plus the laser-noise, the other one measures only the laser noise. The difference between the two is the actual signal without the noise.

The Future

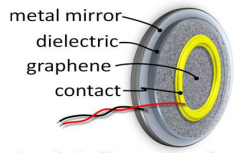

Optical devices that utilize graphene's nonlinear absorption for passive mode-locking or active laser stabilization

References

1. Haiml, M et al. "Optical Characterization of Semiconductor Saturable Absorbers." Applied Physics B 79, 331-339 (2004).

2. Maas, D. J. H. C et al. "High Precision Optical Characterization of Semiconductor Saturable Absorber Mirrors." Optics Express 7571 (2008).

Figure D.1: The poster presented at the annual meeting of the Four Corners section of the American Physical Society.

American Physical Society

APS physics

Jonah Miller

University of Colorado

"A Systematic Study of Techniques to Directly Measure the Saturable Absorption of Graphene"

for an outstanding student paper
at the Four Corners Section meeting, Ogden, Utah
October 15–16, 2010

29 November 2010
Date

Sally Seidel
Chair

Figure D.2: Award for outstanding student poster

Figure D.3: Comments by first judge

Student Competition Judging Form
2010 APS 4 Corners Meeting
Weber State University

Title of Presentation	A Systematic Study of Techniques
Student's Name / Affiliation	UNDERGRAD
Student Status	Jonah MILLER / C.U.
Session and Abstract Number	E1.00001
Judge	

Judging Criteria	Scoring: *Circle one integer in each category.* *A score of 8 indicates a typical student talk.* *Please sum the total below*				
	disagree	slightly disagree	agree	strongly agree	very strongly agree
Structure The presentation clearly exhibited an introduction, the methods employed, the results, a discussion, and conclusions.	6	7	8	(9)	10
Level The technical level of the presentation was appropriate for the audience.	6	7	8	9	(10)
Mastery The student demonstrated mastery of the subject matter.	6	7	8	9	(10)
Graphical Material The quality of the graphical material enhanced the presentation.	6	7	8	9	(10)
Delivery The student's verbal delivery enhanced the presentation of the material.	6	7	8	(9)	10
J.M. deserves an award for this poster	**Total Score:**			48	

Notes Very Strong poster - Impressive research effort from undergraduate, well presented and well explained - Shows a considerable amount of independent work - and awareness of strengths & limitations -

As soon as the session is over, please return your completed forms to Sally Seidel, SU 320.

Figure D.4: Comments by second judge

Student Competition Judging Form
2010 APS 4 Corners Meeting
Weber State University

Title of Presentation	A Systematic Study ... Graphene
Student's Name / Affiliation	Jonah Maller UC
Student Status	UG
Session and Abstract Number	E1.00001
Judge	

Judging Criteria	**Scoring:** ***Circle one integer in each category.*** ***A score of 8 indicates a typical student talk.*** ***Please sum the total below***				
	disagree	**slightly disagree**	**agree**	**strongly agree**	**very strongly agree**
Structure The presentation clearly exhibited an introduction, the methods employed, the results, a discussion, and conclusions.	6	7	(8)	9	10
Level The technical level of the presentation was appropriate for the audience.	6	7	8	(9)	10
Mastery The student demonstrated mastery of the subject matter.	6	7	8	(9)	10
Graphical Material The quality of the graphical material enhanced the presentation.	6	7	8	(9)	10
Delivery The student's verbal delivery enhanced the presentation of the material.	6	7	8	(9)	10
	Total Score:				44

Notes

As soon as the session is over, please return your completed forms to Sally Seidel, SU 320.

Figure D.5: Comments by third judge

Student Competition Judging Form
2010 APS 4 Corners Meeting
Weber State University

Title of Presentation	A SYSTEMATIC STUDY OF TECHNIQUES TO DIRECTLY...
Student's Name / Affiliation	JONAH MILLER UC
Student Status	UNDERGRADUATE
Session and Abstract Number	POSTER: E1.00001
Judge	

Judging Criteria	**Scoring:** ***Circle one integer in each category.*** ***A score of 8 indicates a typical student talk.*** ***Please sum the total below***				
	disagree	**slightly disagree**	**agree**	**strongly agree**	**very strongly agree**
Structure The presentation clearly exhibited an introduction, the methods employed, the results, a discussion, and conclusions.	6	(7)	8	9	10
Level The technical level of the presentation was appropriate for the audience.	6	7	8	(9)	10
Mastery The student demonstrated mastery of the subject matter.	6	7	8	9	(10)
Graphical Material The quality of the graphical material enhanced the presentation.	6	7	(8)	9	10
Delivery The student's verbal delivery enhanced the presentation of the material.	6	7	8	9	(10)
	Total Score:				44

Notes

As soon as the session is over, please return your completed forms to Sally Seidel, SU 320.

Figure D.6: Comments by fourth judge

Student Competition Judging Form
2010 APS 4 Corners Meeting
Weber State University

Title of Presentation	
Student's Name / Affiliation	JONAH MILLER UC
Student Status	UG
Session and Abstract Number	E1 /
Judge	

Judging Criteria	Scoring: *Circle one integer in each category.* *A score of 8 indicates a typical student talk.* *Please sum the total below*				
	disagree	slightly disagree	agree	strongly agree	very strongly agree
Structure The presentation clearly exhibited an introduction, the methods employed, the results, a discussion, and conclusions.	6	7	(8)	9	10
Level The technical level of the presentation was appropriate for the audience.	6	7	(8)	9	10
Mastery The student demonstrated mastery of the subject matter.	6	7	8	(9)	10
Graphical Material The quality of the graphical material enhanced the presentation.	6	7	8	(9)	10
Delivery The student's verbal delivery enhanced the presentation of the material.	6	7	8	(9)	10
	Total Score: 43				

Notes – Your poster was visually very good.
– Good understanding of the material.

As soon as the session is over, please return your completed forms to Sally Seidel, SU 320.

Appendix E

Paper Submitted Regarding the Doping of Graphene by Nitric Acid

Our group recently submitted a paper based on our work in doping graphene with nitric acid. The differential transmission and spectrophotometry measurements in this work were performed by Chien-Chung Lee. The differential transmission measurements were made on the system described in chapter 3, which was constructed by Chien-Chung Lee and myself. All doping was performed by Chien-Chung Lee, while all Raman measurements in the paper were performed by myself.

Applied Physics B: Lasers and Optics manuscript No.
(will be inserted by the editor)

Doping-induced changes in the saturable absorption of monolayer graphene

C.-C. Lee ⋆, J. M. Miller, and T. R. Schibli

Department of Physics, University of Colorado at Boulder, 2000 Colorado Avenue, Boulder, CO 80309, USA

Received: date / Revised version: date

Abstract Graphene is a broadband, fast saturable absorber well suited for passive mode-locking of lasers. The broadband absorption, ultra-short recovery time, and low cost of graphene absorbers compare favorably with traditional semiconductor saturable absorber mirrors (SESAMs). However, it remains difficult to tailor the parameters of a monolayer graphene absorber such as the modulation depth and the insertion loss; this limits the absorber's design freedom, which is often required for mode-locking without Q-switching instability. We demonstrate in this work that, by hole-doping graphene chemically to various Fermi levels, the modulation depth and insertion loss are modified. Further control of graphene's saturable absorption by electric-field gating and its application to active suppression of Q-switching in lasers is discussed.

1 Introduction

Graphene, a single layer of carbon atoms arranged in a honeycomb structure, has a universal linear optical absorption of 2.3% spanning visible to far infrared light [1]. This universal interband absorption results from the linear dispersion near the Dirac point, where the conduction and the valence bands meet. However, when the distribution of electrons and holes are not symmetric about the Dirac point, i.e. Fermi level is either above (n-doping) or below (p-doping) the Dirac point, it has been observed that this linear absorption becomes non-universal at low photon energy due to state blocking [2]. This doping often originates from the contact of graphene with the substrate [3]. In addition to the doping induced by substrate, the Fermi level can be tuned by electric-field gating and the interband absorption is minimized when the Fermi level approaches half of the excitation photon energy [4]. Although the doping effect on the interband absorption was already observed at low excitation levels [2,4], there has not been a study of the same effect in the nonlinear regime. The doping effects on the interband absorption at high excitation levels are of interest because the interband absorption can be saturated by a light pulse with high peak intensities [5, 6]. This saturable absorption has been used extensively to mode-lock lasers [7–16]; however, the effects of doping on the saturable absorption have, to the best of our knowledge, not been investigated. In this paper, we report the effect of chemical p-doping of graphene on its optical properties as a saturable absorber. We also discuss this controllability of saturable absorption and its importance in producing stable ultra-short pulse trains in lasers.

Send offprint requests to:
⋆ *Email address:* ChienChung.Lee@Colorado.EDU

2 Preparation and characterization of graphene saturable absorbers

2.1 Growth and transfer of graphene

The graphene samples used in the experiment were grown on copper foils (Alfa Aesar #13382, 25μm) by chemical vapor deposition (CVD) [17]. The total pressure in our CVD process was maintained at the level of 10 mTorr in order to obtain large domains of graphene [18]. The CVD process began with the annealing of the copper foils at 1000°C with 5 sccm H_2 flow for 30 minutes. While the copper foils were maintained at 1000°C, graphene was grown with 1 sccm H_2 and 1 sccm CH_4 for 30 minutes, followed by a 5-minute phase of 1 sccm H_2 and 10 sccm CH_4 to fill gaps between domains [18]. Fig. 1 shows the domain sizes and boundaries of our CVD graphene. After the growth, the graphene on copper foils was spin-coated with polymethyl methacrylate (PMMA) as a mechanical support during wet-transfer processes, in which the copper foils were etched by ferric chloride (0.5M) solution, and the graphene was washed in deionized water several

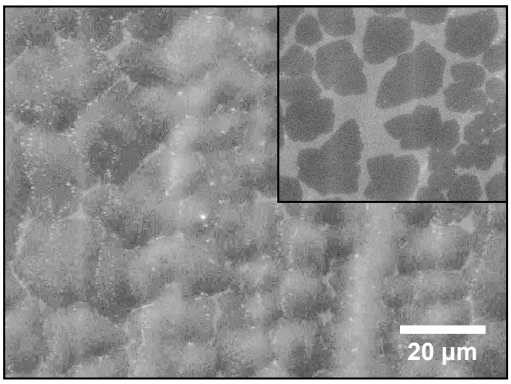

Fig. 1 A scanning electron microscope image of graphene domains and boundaries. Inset: disconnected graphene domains that are grown without a second step of high methane flow rates. The domain sizes (100-400 μm^2) are much larger than the laser beam size in our experiements and are sufficient for most laser applications.

times before being transferred onto a microscope slide (VWR #48300-025).

The transferred graphene was baked in a tube furnace at 300°C for an hour with 50 sccm Ar flow, 5 sccm H_2 flow (pressure $\approx$ 30 mTorr), reducing the doping that could result from adsorbates such water molecules or other contaminants [19,20]. Moreover, we found that this heat treatment can prevent the delamination of the graphene from the substrates in the following doping step, which we hypothesized to be caused by the removal of water molecules between the graphene layer and the substrate. In this work, we use nitric acid of low concentration ($\leq$0.8 wt%) to p-doped graphene [21] The acid was drop-cast on the graphene surface and, after five minutes, blown dry by nitrogen. Various doping levels were achieved by nitric acid of concentrations from 0.1 to 0.8 wt%.

2.2 Characterization of Fermi level in graphene

Fermi levels in graphene are often estimated from the gate voltage needed for obtaining the minimum electrical conductivity [22]. This method, however, brings complications of gate electrode implementation in transmissive samples. In this work, we quantified the Fermi levels by graphene's infrared transmission spectra from 3000 nm to 900 nm with a spectrophotometer (Varian, Cary 500). The beam was 3 mm in diameter and at near-normal incidence to the graphene-substrate interface. Large beam size was used in order to average the spatial-depedent doping caused by the substrate and possibly by the dopants. The calibration of the transmission spectra were done by subtracting the spectrum of a blank microscope slide from all measurements.

The calculation of graphene's transmissive spectrum begins with the optical conductivity (σ) of graphene as a

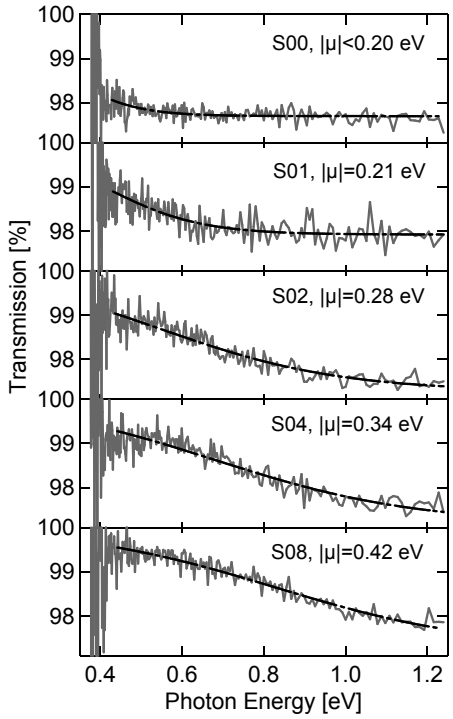

Fig. 2 Transmission spectra of doped graphene as a function of photon energy. The doping level can be controlled by nitric acid of different concentrations. Solid line: measurment; dashed line: fit. From top to bottom, the curves represent (S00) baked graphene, (S01) baked and doped by 0.1wt% acid, (S02) baked and doped by 0.2wt% acid, (S04) baked and doped by 0.4wt% acid, (S08) baked and doped by 0.8wt% acid. Linear optical absorption at low photon energy reduces as the p-doping level increases.

function of optical frequency(ω), chemical potential(μ), and temperature(T) [1]:

$$\sigma = \frac{\sigma_0}{2}\left[\tanh\left(\frac{\hbar\omega + 2\mu}{4k_BT}\right) + \tanh\left(\frac{\hbar\omega - 2\mu}{4k_BT}\right)\right], \quad (1)$$

where σ_0 is the optical conductivity of undoped graphene ($\mu = 0$), k_B is the Boltzmann constant, e is the electron charge, $\hbar$ is the reduced Plank constant, and T is the temperature of the sample. At normal incidence, the transmittance $\mathcal{T}$ of graphene at the interface of air ($n = 1$) and glass ($n \approx 1.5$) is

$$\mathcal{T} = \frac{4n_1n_2}{(n_1 + n_2 + \sigma/c\epsilon_0)^2} \approx \mathcal{T}_0\left[1 - \frac{2\sigma}{c\epsilon_0\,(n_1 + n_2)}\right], \quad (2)$$

where c is the speed of light in vacuum, ϵ_0 is the vacuum permittivity, and $\mathcal{T}_0 = 4n_1n_2\,(n_1 + n_2)^{-2} = 0.96$ is the transmittance at the same interface without graphene. The change of transmittance due to the presence of graphene, including the two interfaces of a substrate, is then

$$\Delta\mathcal{T}_{total} = \left|\mathcal{T}\mathcal{T}_0 - \mathcal{T}_0^2\right| = \frac{2\sigma\mathcal{T}_0^2}{c\epsilon_0\,(n_1 + n_2)}. \quad (3)$$

The value of chemical potential μ can then be extracted by fitting Eq. 3 to the measured spectra of $\Delta\mathcal{T}_{total}$. Fig. 2 shows the transmission spectra of our graphene samples that are chemically p-doped to different levels. We have reproducibly observed that, as the concentration of nitric acid dopants increases, graphene becomes more p-doped. Furthermore, the optical absorption at low photon energies is reduced due to lack of electron population in the valence band. The baked sample (S00) shows nearly universal absorption at photon energies as low as 0.4 eV, which is limited by the spectral range of the spectrophotometer.

Due to the spatial dependence of doping resulting from substrates and dopants, the curves in Fig. 2 possess a slow transition from occupied states to vacant states in the valence band. Assuming that the distribution of this spatial dependence is symmetric about its mean value, the fit with Eq. 1 can be treated by finding an effective temperature T. Note that this effective temperature does not represent the physical temperature of the electron gas in graphene. In our fits, typical T values were 3000-5000K, and we believe that lower effective temperature can be observed with a smaller beam size and/or atomically flat substrate surfaces.

2.3 Raman spectra of graphene

In addition to optical absorption measurements, we examined number of layers and defects of our graphene samples by their Raman spectra. Raman measurements were performed on a home-built Raman microscope in epi-illumination and detection geometry, with excitation provided by a 633 nm HeNe laser (spot size ≈ 1 μm, peak power < 1 kW/cm^2). The Raman scattered light is spectrally filtered with a 160 cm^{-1} cut-off filter (Semrock, LP02-633RU-25) and detected with a spectrometer with a 1200 g/mm (Newport, 53-*-220H) grating for single-peak measurements or a 600 g/mm grating (Newport, 53-*-350R) for measurements spanning the full relevant spectrum of graphene, and a liquid-nitrogen-cooled CCD camera(Princeton Instruments, Spec-10 2KB/LN). The peak power was kept low so as not to damage the sample or remove dopants with thermal effects. To confirm that our measurements were non-intrusive, an extremely short measurement (< 10 seconds) was made before and after the longer integration-time (60–300 seconds), higher SNR, measurements to confirm no change in the spectrum.

Fig. 3 shows the Raman spectra of our graphene samples. The undoped, only baked sample showed low I(D)/I(G) ratio (<0.1) and single 2D peak with a FWHM of 35 cm^{-1}. This suggests that our CVD-grown graphene is mostly defect-free and monolayer [23]. Our nitric-acid-doped graphene showed an upshift in the G band of $\sim$5 cm^{-1} and the 2D band of $\sim$4 cm^{-1}, a peak narrowing in the FWHM of the G band of between 2 and 5 cm^{-1},

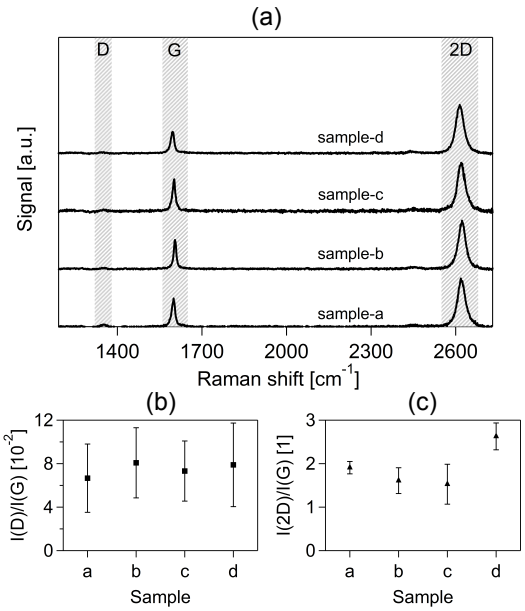

Fig. 3 (a) Representative Raman spectra of graphene samples used in the experiments. Sample-a: baked sample, $E_F <$ 200 meV; sample-b: doped sample, $E_F \approx 200$ meV; sample-c: doped, $E_F \approx 400$ meV; sample-d: baked after doped to $E_F \approx$ 400 meV. No significant changes of I(2D)/I(G) and I(D)/I(G) ratios were observed in samples-b,c,d, implying that nitric acid did not attack graphene and was removed by baking without damaging graphene. (b) All samples have small I(D)/I(G) ratios, which implies nearly defect-free graphene. (c) All samples have a I(2D)/I(G) ratio of about 2.

and a decrease in the ratio I(2D)/I(G) from about 2 to about 1.6 (from sample-a to sample-b). This agrees qualitatively with Raman measurements made on electrostatically doped graphene [24,25] and graphene doped by organic molecules [26], although the G peak narrowing has not always been observed in chemically doped graphene.

As we increased level of p-doping to -400 meV (sample-c), the G and 2D bands down-shifted about halfway towards their original positions, which, to our knowledge, has not been observed in chemically doped graphene. However, doping graphene with nitric acid has not before been carefully studied, and the I(2D)/I(G) ratio, suggested to be an important measure of doping level, continued to decrease as expected (to about 1.5). We found no correlation between doping concentration and the I(D)/I(G) ratio, which is indicative of defects in graphene. We never found a mean I(D)/I(G) peak ratio above 0.12, and it should be noted that I(D) was intentionally over-estimated because of the background noises. When we later baked our samples at 100°C for 1 hour to remove the adsorbants (sample-d), we found that the peak positions fully recovered and, in fact, down-shifted by an additional 2 cm^{-1} for the 2D band and an additional 1.3 cm^{-1} for the G band. Furthermore,

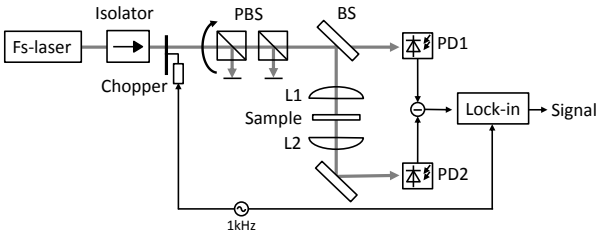

Fig. 4 Differential transmission setup for characterizing the saturable absorption of graphene. Isolator: optical Faraday isolator; PBS: polarization beam splitter cube, two used as a power attenuator; BS: beam splitter; PD1 and PD2: identical photodiodes for balanced detection; L1 and L2: focusing lenses; Sample: graphene on a microscope slide; Chopper: mechanical chopper used with lock-in amplifier to reject part of the laser noise.

the I(2D)/I(G) peak ratio increased to about 2.6. All of these changes after baking imply pristine graphene. It is highly likely that baking after doping removed the adsorbates that had accumulated on the graphene sheet in the time between initial sample preparation of the undoped sample and its measurement in Raman. This would account for the seeming increase in purity after doping and baking.

3 Saturable absorption in graphene

3.1 Characterization of saturable absorption

The saturable absorption in graphene was characterized in a differential transmission setup with balanced detection, shown in Fig. 4. The optical elements used were carefully chosen so as to avoid any nonlinearities not resulting from the sample [27]. We used a soliton mode-locked Er:Yb:glass laser with a center wavelength of 1.56 m, pulse width ∼210 fs, and 86 MHz repetition rate. The beam diameter on the sample was (4.4 ± 0.6) μm. For each measurement, the peak intensity of the pulse was varied logarithmically from 3 to over 3000 MW/cm^2, and the change of transmittance was recorded. Each sample was characterized at ten independent locations, and the fit parameters of all spots were averaged. Fig. 5(a) shows one of these measurements.

We also measured the relaxation time of photo-excited carriers in undoped graphene by a degenerate pump-probe setup with the aforementioned laser; the pump and probe beams were counter-propagating, polarized 90° with respect to each other, and mechanically chopped at two different frequencies around 1 kHz. The change of probe power due to the pump was measured by a lock-in amplifier at a frequency equal to the sum of the two chopping frequencies. The observed transmission transient of graphene is shown in Fig. 5(b).

3.2 Saturable absorption in as-transferred graphene

In graphene, photo-excited carriers relax within ∼200 fs via carrier-carrier scattering and carrier-phonon scattering [28–30,6]. Our pump-probe measurements also showed that the fast relaxation in graphene contributes significantly to the saturable absorption (Fig. 5(b)). To find the macroscopic parameters of a graphene absorber (saturation intensity or fluence, saturable loss, and non-saturable loss), care needs to be taken in fitting a correct theoretical model to experimental saturable absorption curves since graphene in this case cannot be approximated by either the fast or the slow absorber model. The saturation of an absorber can be described by the following equation [31]:

$$\frac{\mathrm{d}\,q(t)}{\mathrm{d}\,t} = \frac{q_0 - q(t)}{\tau_A} - \frac{q(t)I(t)}{F_{sat,A}}, \tag{4}$$

where $q(t)$ is the saturable loss, q_0 is the insertion loss, τ_A is the relaxation time of the absorber, $I(t)$ is the intensity of light, and $F_{sat,A}$ is the saturation fluence of the absorber. For simplicity, we first regard graphene as a fast saturable absorber (pulse width$\gg\tau_A$). Given sech^2-shaped pulses, the loss of absorber can be written as [32]

$$q(S) = \frac{q_s}{\sqrt{S(1+S)}} \tanh^{-1}\left(\sqrt{\frac{S}{1+S}}\right) + q_{ns}, \tag{5}$$

where q_s is the saturable loss, q_{ns} is the non-saturable loss, and S is the ratio of the pulse peak intensity to the saturation intensity of the graphene absorber. Fig. 5(a) shows the nonlinear absorption curve of as-transferred and baked samples. Fitting Eq. 5 to the data, we found the saturation intensity to be (250 ± 80) MW/cm^2, the insertion loss (1.85 ± 0.08)%, the saturable loss (0.85 ± 0.04)%.It should be noted that the insertion loss here refers to the change of transmittance due to the presence of graphene on the air-glass interface, and it is lower than the optical absorption of free-standing graphene ($\pi\alpha = 2.3\%$). The insertion loss was comparable to the calculated change of transmittance $\Delta\mathcal{T}_{total} = 1.7\%$ in Eq. 3. The extra loss could be attributed to the light scattering from graphene.

When a longer relaxation time (τ_A=200 fs) was assumed, from the numerical solutions to Eq. 4, the saturation intensity was lower by a factor of 0.8 (I_{sat} = 200 MW/cm^2, F_{sat} = 40 μJ/cm^2), although in this regime, neither the saturation intensity nor fluence is a good macroscopic quantity of the absorber. One simply needs to refer to the pulse duration and the relaxation time of the absorber.

The saturation intensity we measured can be directly compared with the theoretical value calculated by Vasko [5]. For photon energies near 0.8 eV, the theoretical value is approximately 60 MW/cm^2, and our measured value of (250 ± 80)MW/cm^2 agrees roughly within a factor of

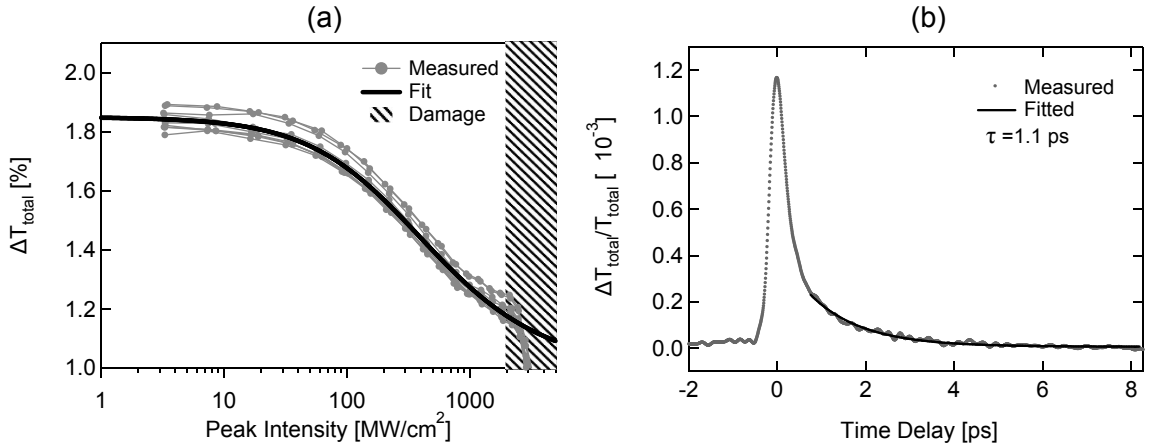

Fig. 5 (a) The change of transmittance caused by graphene as a function of pulse peak intensity. The red curves are ten individual measurements at different locations on the same sample; the black curve is the resulting curve from the average of ten individual fits through the data. (b) Transmission transient of graphene. The slow component of the relaxation time is 1.1 ps; the fast component is not resolved due to the long pulse duration (∼210 fs).

4. The discrepancy between our measurement and the theoretical value could be due to the reduced carrier relaxation time (Fig. 5(b)) caused by the lattice defects around domain boundaries or by the interaction with the substrate, which could add additional relaxation pathways.

Our result also agrees quite well with Sun et al. [7], who measured the saturation intensity for 1.55 μm light to be 266 MW/cm^2 for monolayer and bilayer graphene flakes dispersed in polymers, but we found a large discrepancy between our results and the values reported by Bao et al. [8–10], Tan et al. [11], and Zhang et al. [12–14], who claimed a saturation intensity value of 0.6-0.7 MW/cm^2. Even though their measured saturation intensity seemingly agrees with the model they suggested [9], their model merely accounted for the carrier recombination in direct band-gap semiconductors such as gallium arsenide, but is likely not adequate to describe zero-bandgap graphene.

It may be argued that the saturation intensity depends on the pulse duration used for characterization, but from numerical solutions to Eq. 4, we found that as the pulse duration increases from 200 fs to 10 ps, the saturation intensity decreases by only a factor smaller than 10, which could not explain this discrepancy.

According to Vasko's calculation, the saturation intensity strongly increases with the photon energy due to the proportionality between the relaxation rate and the density of states to which carriers are excited. Several experiments have also shown that the saturation intensity for 800 nm light is above 1GW/cm^2: Dawlaty et al. observed saturable loss but could not reach the saturation intensity even at pulse peak intensities higher than 1 GW/cm^2 (85 fs pulse duration) [28]; Xing et al. showed by z-scan measurements that the saturation intensity was near 4 GW/cm^2 [6]; and Breusing et al. did not observe any saturation with pulse fluence as high as 0.7 mJ/cm^2 (7 fs pulse duration) [30].

3.3 Saturable absorption in chemically-doped graphene

The transmission spectra of undoped and doped graphene are shown in Fig. 2. As the Fermi level was varied from close to the Dirac point to 0.4 eV below the Dirac point, the linear absorption at low photon energies decreased due to state blocking. The corresponding saturation of optical absorption at 1.55 μm wavelength (0.8 eV) is shown in Fig. 6. As the doping level increased, the insertion loss of graphene decreased dramatically from 1.8% to 1%, which matched well with the measured linear absorption.

The non-saturable loss, however, did not increase with the doping level, suggesting that doping with nitric acid does not cause more defects or introduce more scattering loss to the graphene. The saturation intensity also remained roughly the same in doped graphene, which could be understood from the fact that the density of states and carrier relaxation time are not modified by hole-doping.

This flexibility in designing the saturable absorbers is essential to successful continuous-wave mode-locking in solid-state lasers [33]. Given the parameters of a specific laser, suitable parameters of the saturable absorber can be chosen to prevent Q-switching. SESAMs have been used widely in solid-state laser mode-locking because of their design freedom. For graphene absorbers, one can exploit the doping effect to tailor the modulation depth in monolayer graphene, and if higher insertion loss is desired, stacked multilayer graphene can be used.

Even though the parameters of a saturable absorber can be tailored to specific values in order to prevent Q-switching, the allowed range of parameters is often quite

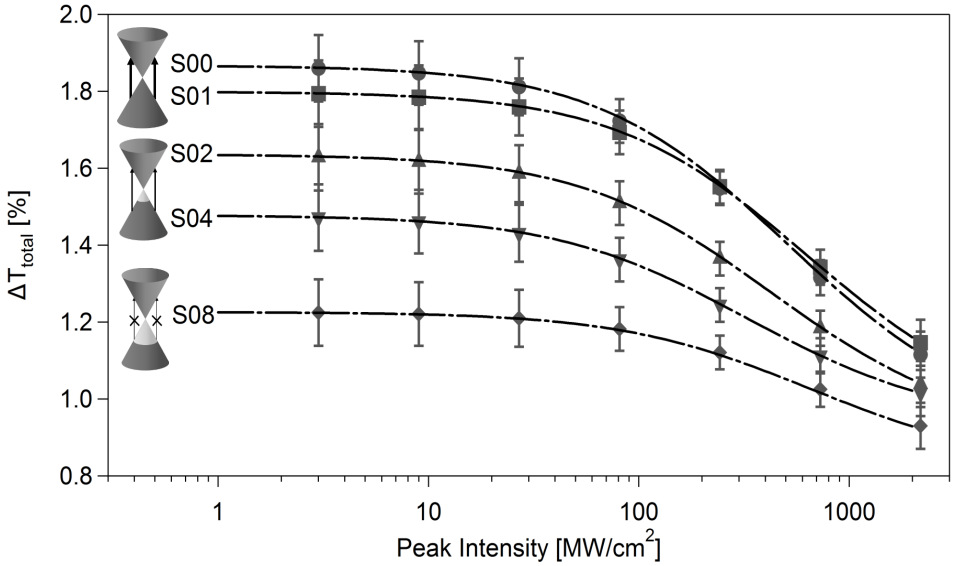

Fig. 6 Transmission loss of doped graphene as a function of pulse peak intensity. For each doping level, one curve (dashed line) obtained by averaging the fit parameters of ten independent spots is shown. From top to bottom, the curves represent (S00) baked graphene, (S01) baked and doped by 0.1wt% acid, (S02) baked and doped by 0.2wt% acid, (S04) baked and doped by 0.4wt% acid, (S08) baked and doped by 0.8wt% acid. The three cones show the band structure of graphene at different doping levels. Upper cone: conduction band; Dark lower cone: electron-filled valence band; and light-colored area: hole-occupied states.

limited, and the parameters of the laser such as gain cross section and pump power also need to be taken into account. In certain situations, using active feedback to suppress Q-switching can be favorable compared to designing absorbers. It has been demonstrated that the laser output power can be directly used to feedback-control the intracavity loss or gain [34,35]. For graphene absorbers, it is possible to implement an external electric field to modulate the carrier density [4,17], or essentially the Fermi level, so that the insertion loss can be controlled by electronics. The relation between the carrier density(n) and Fermi level(E_F) in graphene is given by

$$n = \frac{1}{\pi}\left(\frac{E_F}{\hbar v_F}\right)^2, \tag{6}$$

where v_F is the Fermi velocity ($\sim 10^6$ m/s). To achieve the maximal modulation of insertion loss in a laser with a center wavelength of 1.55 μm, the desired Fermi level is 0.4 eV below the Dirac point, corresponding to a carrier (hole) density of approximately 10^{13} cm^{-2}. To achieve this level of carrier density in a normal electrical-gating configuration with 100 nm dielectric of $\epsilon \approx 4$, one has to apply nearly 100 Volts. Doping graphene with chemicals prior to applying electric fields can thus avoid the use of strong field and avoid dielectric breakdown. This pre-doping would be particularly important for applications in lasers with wavelengths in the near-infrared and visible regions, where the state-blocking is not trivial to achieve solely by electric-field gating.

3.4 Optical damage of graphene

The modulation depth and the saturation intensity of graphene are comparable to those of SESAMs [36]. However, the full modulation depth could not be exploited due to the onset of permanent damage for pulse peak intensities higher than 2 GW/cm^2. We found that the damage resulted from the high peak power of the laser rather than from the heat due to the average power. This was confirmed by observing the damage with the laser under two conditions: (1) cw mode-locking regime and (2) continuous-wave regime. While the average power was the same in both regimes, the peak power was 50,000-times higher in the mode-locked regime. Despite the same average power, no damage was observed when the laser was operated in the continuous-wave regime. To further investigate the damage mechanism, the graphene sample was purged with argon, excluding the possibility of oxygen interacting with graphene under high pulse intensity. It was found that the damage threshold did not increase in this oxygen-free environment. We thus assume that the damage could have originated from the high-field interaction of graphene with residual contaminants or from lattice defects. The damage threshold could also depend on the flatness and material of the substrate.

4 Summary

We showed that, in monolayer graphene, the modulation depth of its saturable absorption can be tuned by

hole-doping. When applying graphene as a saturable absorber for ultrashort pulse generation, it can offer more design freedom that helps prevent Q-switching. Hole-doping does not noticeably affect the saturation intensity and the non-saturable loss in graphene. There might, however, be a stronger correlation between electron doping and the saturation intensity due to the decreased number of relaxation pathways, which will be the subject of a further study. For undoped graphene, we measured the saturation intensity to be (250 ± 80) MW/cm^2, and the previously reported values (<1 MW/cm^2 at 1.55 μm wavelength) are, in our opinion, likely not correct. We also proposed that the insertion loss of graphene absorbers can be modulated by an electric field; therefore, negative feedback-control can be exploited to suppress Q-switching. We argued that for application in lasers at telecommunications or shorter wavelengths, chemical predoping of graphene should be combined with electric-field gating to provide the maximal modulation. Saturable absorbers that are controlled electrically will likely push the development of compact solid-state mode-locked lasers with ultrahigh repetition rates.

Acknowledgements We deeply appreciate the support from Dr. Kaoru Minoshima, AIST/NMIJ Tsukuba, Japan, who provided us the Er:Yb:glass. We would also like to express our gratitude towards Prof. Markus Raschke for lending us the use of the micro-Raman system and towards Joanna Atkin and Samuel Berweger for lending us their expertise in Raman spectroscopy. This research was supported in part by the NNIN at the Colorado Nanofabrication Laboratory and the National Science Foundation under Grant No. ECS-0335765 and by the Innovative Seed Grant Program at the University of Colorado.

References

1. T. Stauber, N. M. R. Peres, and A. K. Geim. Optical conductivity of graphene in the visible region of the spectrum. *Phys. Rev. B*, 78:085432, Aug 2008.
2. Kin Fai Mak, Matthew Y. Sfeir, Yang Wu, Chun Hung Lui, James A. Misewich, and Tony F. Heinz. Measurement of the optical conductivity of graphene. *Phys. Rev. Lett.*, 101:196405, Nov 2008.
3. Yumeng Shi, Xiaochen Dong, Peng Chen, Junling Wang, and Lain-Jong Li. Effective doping of single-layer graphene from underlying sio$_2$ substrates. *Phys. Rev. B*, 79:115402, Mar 2009.
4. Feng Wang, Yuanbo Zhang, Chuanshan Tian, Caglar Girit, Alex Zettl, Michael Crommie, and Y. Ron Shen. Gate-variable optical transitions in graphene. *Science*, 320(5873):206–209, 2008.
5. F. T. Vasko. Saturation of interband absorption in graphene. *Phys. Rev. B*, 82:245422, Dec 2010.
6. Guichuan Xing, Hongchen Guo, Xinhai Zhang, Tze Chien Sum, and Cheng Hon Alfred Huan. The physics of ultrafast saturable absorption in graphene. *Opt. Express*, 18(5):4564–4573, Mar 2010.
7. Zhipei Sun, Tawfique Hasan, Felice Torrisi, Daniel Popa, Giulia Privitera, Fengqiu Wang, Francesco Bonaccorso, Denis M. Basko, and Andrea C. Ferrari. Graphene mode-locked ultrafast laser. *ACS Nano*, 4(2):803–810, 2010. PMID: 20099874.
8. Qiaoliang Bao, Han Zhang, Zhenhua Ni, Yu Wang, Lakshminarayana Polavarapu, Zexiang Shen, Qing-Hua Xu, Dingyuan Tang, and Kian Loh. Monolayer graphene as a saturable absorber in a mode-locked laser. *Nano Research*, 4:297–307, 2011. 10.1007/s12274-010-0082-9.
9. Qiaoliang Bao, Han Zhang, Yu Wang, Zhenhua Ni, Yongli Yan, Ze Xiang Shen, Kian Ping Loh, and Ding Yuan Tang. Atomic-layer graphene as a saturable absorber for ultrafast pulsed lasers. *Advanced Functional Materials*, 19(19):3077–3083, 2009.
10. Qiaoliang Bao, Han Zhang, Jia-xiang Yang, Shuai Wang, Ding Yuan Tang, Rajan Jose, Seeram Ramakrishna, Chwee Teck Lim, and Kian Ping Loh. Graphenepolymer nanofiber membrane for ultrafast photonics. *Advanced Functional Materials*, 20(5):782–791, 2010.
11. W. D. Tan, C. Y. Su, R. J. Knize, G. Q. Xie, L. J. Li, and D. Y. Tang. Mode locking of ceramic nd:yttrium aluminum garnet with graphene as a saturable absorber. 96(3):031106, 2010.
12. Han Zhang, Qiaoliang Bao, Dingyuan Tang, Luming Zhao, and Kianping Loh. Large energy soliton erbium-doped fiber laser with a graphene-polymer composite mode locker. 95(14):141103, 2009.
13. Han Zhang, Dingyuan Tang, R. J. Knize, Luming Zhao, Qiaoliang Bao, and Kian Ping Loh. Graphene mode locked, wavelength-tunable, dissipative soliton fiber laser. 96(11):111112, 2010.
14. H. Zhang, D. Y. Tang, L. M. Zhao, Q. L. Bao, and K. P. Loh. Large energy mode locking of an erbium-doped fiber laser with atomic layer graphene. *Opt. Express*, 17(20):17630–17635, Sep 2009.
15. Won Bae Cho, Hwang Woon Lee, Sun Young Choi, Jun Wan Kim, Dong-Il Yeom, Fabian Rotermund, Jinho Kim, and Byung Hee Hong. Monolayer graphene saturable absorber for bulk laser mode-locking. In *Conference on Lasers and Electro-Optics*, page JThE86. Optical Society of America, 2010.
16. C.-C. Lee, T. R. Schibli, G. Acosta, and J. S. Bunch. Ultra-Short Optical Pulse Generation with Single-Layer Graphene. *Journal of Nonlinear Optical Physics and Materials*, 19:767–771, 2010.
17. Xuesong Li, Weiwei Cai, Jinho An, Seyoung Kim, Junghyo Nah, Dong Yang, Richard Piner, Aruna Velamakanni, Inhwa Jung, Emanuel Tutuc, Sanjay K. Banerjee, Luigi Colombo, and Rodney S. Ruoff. Large-area synthesis of high-quality and uniform graphene films on copper foils. 324(5932):1312–1314, 2009.
18. Xuesong Li, Carl W. Magnuson, Archana Venugopal, Jinho An, Ji Won Suk, Boyang Han, Mark Borysiak, Weiwei Cai, Aruna Velamakanni, Yanwu Zhu, Lianfeng Fu, Eric M. Vogel, Edgar Voelkl, Luigi Colombo, and Rodney S. Ruoff. Graphene films with large domain size by a two-step chemical vapor deposition process. *Nano Letters*, 10(11):4328–4334, 2010.
19. Myrsini Lafkioti, Benjamin Krauss, Timm Lohmann, Ute Zschieschang, Hagen Klauk, Klaus v. Klitzing, and Jurgen H. Smet. Graphene on a hydrophobic substrate:

Doping reduction and hysteresis suppression under ambient conditions. *Nano Letters*, 10(4):1149–1153, 2010. PMID: 20218633.

20. P Joshi, H E Romero, A T Neal, V K Toutam, and S A Tadigadapa. Intrinsic doping and gate hysteresis in graphene field effect devices fabricated on sio 2 substrates. *Journal of Physics: Condensed Matter*, 22(33):334214, 2010.
21. Amal Kasry, Marcelo A. Kuroda, Glenn J. Martyna, George S. Tulevski, and Ageeth A. Bol. Chemical doping of large-area stacked graphene films for use as transparent, conducting electrodes. *ACS Nano*, 4(7):3839–3844, 2010.
22. K. S. Novoselov, A. K. Geim, S. V. Morozov, D. Jiang, Y. Zhang, S. V. Dubonos, I. V. Grigorieva, and A. A. Firsov. Electric field effect in atomically thin carbon films. *Science*, 306(5696):666–669, 2004.
23. A.C. Ferrari et al. Raman spectra of graphene and graphene layers. *Physical Review Letters*, 97(187401):1–4, 2006.
24. A. Das et al. Monitoring dopants by raman scattering in an electrochemically top-gated graphene transistor. *Nature Nanotechnology*, 3(67):210–215, 2008.
25. Jun Yan et al. Electric field effect tuning of electron-phonon coupling in graphene. *Physical Review Letters*, 2007.
26. Xiaochen Dong et al. Doping single-layer graphene with aromatic molecules. *Small*, 5, 2009.
27. M. Haiml, R. Grange, and U. Keller. Optical characterization of semiconductor saturable absorbers. *Applied Physics B: Lasers and Optics*, 79:331–339, 2004. 10.1007/s00340-004-1535-1.
28. Jahan M. Dawlaty, Shriram Shivaraman, Mvs Chandrashekhar, Farhan Rana, and Michael G. Spencer. Measurement of ultrafast carrier dynamics in epitaxial graphene. 92(4):042116, 2008.
29. Haining Wang, Jared H. Strait, Paul A. George, Shriram Shivaraman, Virgil B. Shields, Mvs Chandrashekhar, Jeonghyun Hwang, Farhan Rana, Michael G. Spencer, Carlos S. Ruiz-Vargas, and Jiwoong Park. Ultrafast relaxation dynamics of hot optical phonons in graphene. 96(8):081917, 2010.
30. M. Breusing, S. Kuehn, T. Winzer, E. Malić, F. Milde, N. Severin, J. P. Rabe, C. Ropers, A. Knorr, and T. Elsaesser. Ultrafast nonequilibrium carrier dynamics in a single graphene layer. *Phys. Rev. B*, 83:153410, Apr 2011.
31. G.P. Agrawal and N.A. Olsson. Self-phase modulation and spectral broadening of optical pulses in semiconductor laser amplifiers. *Quantum Electronics, IEEE Journal of*, 25(11):2297 –2306, nov 1989.
32. T.R. Schibli, E.R. Thoen, F.X. Krtner, and E.P. Ippen. Suppression of q-switched mode locking and break-up into multiple pulses by inverse saturable absorption. *Applied Physics B: Lasers and Optics*, 70:S41–S49, 2000. 10.1007/s003400000331.
33. Franz X. Kaertner, Luigi R. Brovelli, Daniel Kopf, Markus Kamp, Irio G. Calasso, and Ursula Keller. Control of solid state laser dynamics by semiconductor devices. 34(7):2024–2036, 1995.
34. T. R. Schibli, U. Morgner, and F. X. Kärtner. Control of q-switched mode locking by active feedback. *Opt. Lett.*, 26(3):148–150, Feb 2001.
35. Nicolas Joly and Serge Bielawski. Suppression of q-switch instabilities by feedback control in passively mode-locked lasers. *Opt. Lett.*, 26(10):692–694, May 2001.
36. U. Keller, K.J. Weingarten, F.X. Kartner, D. Kopf, B. Braun, I.D. Jung, R. Fluck, C. Honninger, N. Matuschek, and J. Aus der Au. Semiconductor saturable absorber mirrors (sesam's) for femtosecond to nanosecond pulse generation in solid-state lasers. *Selected Topics in Quantum Electronics, IEEE Journal of*, 2(3):435 –453, sep 1996.

Bibliography

[1] T. Kobayashi et al. In Proceedings of the 145th International Conference, pages 13–15. Springer Series in Chemical Physics, 2005.

[2] R. Holzwarth et al. Optical frequency synthesizer for precision spectroscopy. Physics Review Letters, 85:2264–2267, 2000.

[3] D.J. Jones et al. Carrier-envelope phase control of femtosecond mode-locked lasers and direct optical frequency synthesis. Science, 288:365–365, 2000.

[4] K. Minoshima et al. High-accuracy measurement of 240-m distance in an optical tunnel by use of a compact femtosecond laser. Applied Optics, 39:5512–5517, 2000.

[5] T.R. Schibli et al. Displacement metrology with sub-pm resolution in air based on a fs-comb wavelength synthesizer. Optics Express, 14:5984–5993, 2006.

[6] U. Keller. Progress in Optics, volume 46, chapter 1. Ultrafast Solid-State Lasers, pages 1–117. Elsevier, 2004.

[7] I. P. Ippen. Principles of passive mode locking. Applied Physics B, 58:159–170, 1994.

[8] H. A. Haus. Theory of mode locking with a slow saturable absorber. IEEE Journal of Quantum Mechanics, QE-11(9), 1975.

[9] H. A. Haus. Theory of mode locking with a fast saturable absorber. Journal of Applied Physics, 46(7), 1975.

[10] A. Geim and A. H. Macdonald. Graphene: Exploring carbon flatland. Physics Today, 60:35–41, 2007.

[11] S. Bae et al. Roll-to-roll production of 30-inch graphene films for transparent electrodes. Nature Nanotechnology, 132, 2010.

[12] Z. Wang et al. A high-performance top-gate graphene field-effect transistor based frequency doubler. Applied Physics Letters, 26:173104–1–3, 2010.

[13] F. Schedin et al. Detection of individual gas molecules adsorbed on graphene. Nature Materials, 6:652–655, 2007.

[14] K. S. Novoselov et al. Room-temperature quantum hall effect in graphene. Science, 315(5817):1379, 2007.

[15] Bolotin K. I. et al. Observation of the fractional quantum hall effect in graphene. Nature, 462(7270):196–199, 2009. 10.1038/nature08582.

[16] J. S. Bunch et al. Electrochemical resonators from graphene sheets. Science, 315(5811):490–493, 2007.

[17] J. S. Bunch et al. Impermeable atomic membranes from graphene sheets. Nano Letters, 8(8):2458–2462, 2008.

[18] W. Drexler et al. Ultrahigh resolution optical coherence tomography of the human retina. Nature Medicine, 7:502–507, 2001.

[19] M.C. Stowe et al. High resolution atomic coherent control via spectral phase manipulation of an optical frequency comb. Physics Review Letters, 96:153001–153001, 2006.

[20] Z. Zhu et al. Pump-probe spectroscopy of exciton dynamics in (6,5) carbon nanotubes. Physical Chemistry C, 111:3831–3835, 2007.

[21] T. Steinmetz et al. Laser frequency combs for astronomical observations. Science, 321:1335–1337, 2008.

[22] T.R. Schibli. Combs for dark energy. Nature Photonics, 2:712–713, 2008.

[23] C.-H. Li et al. A laser frequency comb that enables radial velocity measurements with a precision of 1 cm/s. Nature, 452:610–612, 2008.

[24] J. Kim et al. Drift-free femtosecond timing synchronization of remote optical and microwave sources. Nature Photonics, 2:733–736, 2008.

[25] R. M. Wood. Laser-Induced Damage of Optical Materials. Institute of Physics Publishing, 2003.

[26] M. Haiml et al. Optical characterization of semiconductor saturable absorbers. Applied Physics B, 79:331–339, 2004.

[27] P. R. Wallace. The band theory of graphite. Physics Review, 71:622–634, 1947.

[28] H.P. Boehm et al. Thinnest carbon foils. Z. Naturforschung, 17b:150–153, 1962.

[29] K.S. Novoselov et al. Electric field effect in atomically thin carbon films. Science, 306:666–669, 2004.

[30] The Royal Swedish Academy of Sciences. The 2010 nobel prize in physics - press release. nobelprize.org, 2010.

[31] J. M. Dawlatey et al. Measurement of ultrafast carrier dynamics in epitaxial graphene. Applied Physics Letters, 92:042116–1–042116–3, 2008.

[32] T. Stauber et al. Optical conductivity of graphene in the visible region of the spectrum. Physical Review B, 78:085432–1–8, 2008.

[33] C. Lee et al. Measurement of the elastic properties and intrinsic strength of monolayer graphene. Science, 321(5887):385–388, 2008.

[34] Q. Bao et al. Atomic-layer graphene as a saturable absorber for ultrafast pulsed lasers. Advanced Functional Materials, 19:3077–3083, 2009.

[35] S. Kamar et al. Femtosecond carrier dynamics and saturable absorption in graphene suspensions. Applied Physics Letters, 95:191911–1–191911–3, 2009.

[36] C.-C. Lee et al. Ultra-short optical pulse generation with single-layer graphene. Journal of Nonlinear Optical Physics and Materials, 19(4):767–771, 2010.

[37] J. M. Miller et al. A systematic study of techniques to directly measure the saturable absorption of graphene. In Annual Meeting of the Four Corners Section of the American Physical Society, volume 55, 2010.

[38] Z. Sun et al. Graphene mode-locked ultrafast laser. ACS Nano, 4(2):803–810, 2010. PMID: 20099874.

[39] W. D. Tan et al. Mode locking of ceramic nd:yttrium aluminum garnet with graphene as a saturable absorber. Applied Physics Letters, 96(031106):1–3, 2010.

[40] F. T. Vasko. Saturation of interband absorption in graphene. Physics Review B, 82(245422):1–6, 2010.

[41] X. Guichuan et al. The physics of ultrafast saturable absorption in graphene. Optics Express, 18(5):4564–4573, 2010.

[42] Anonymous. Course on Solid State Physics, chapter 2. Physics Archives. Published online, 2010. Website: http://physicsarchives.com/index.php/courses/967.

[43] D. J. Griffiths. Introduction to Quantum Mechanics. Prentice Hall, Upper Saddle River, New Jersey, 2nd edition, 2005.

[44] R. Shankar. Principles of Quantum Mechanics. Plenum Press, New York, 1994.

[45] N. W. Ashcroft et al. Solid State Physics. Brooks/Cole, Belmont, California, 1976.

[46] Omega Centre. Online Access 09/17/11. Website: http:// www.omegacentre.bartlett.ucl.ac.uk/images/photos/profiles/road-athens_attiki.jpg.

[47] Bunkerville. Online Access 09/17/11. Website: http://bunkerville.files.wordpress.com/2010/08/traffic-jam.jpg.

[48] Unknown Photographer. Online Access 09/17/11. Website: http://img.webmd.com/dtmcms/live/webmd/consumer_assets/site_images/articles/health_tools/sleep_disorder_slideshow/getty_rm_photo_of_busy_highway.jpg.

[49] M. Brown. Differential Equations and their Applications. Springer-Verlag New York, 1983.

[50] T. R. Schibli et al. Suppression of q-switched mode locking and break-up into multiple pulses by inverse saturable absorption. Applied Physics B: Lasers and Optics, 70:S41–S49, 2000. 10.1007/s003400000331.

[51] G. F. Dresselhaus et al. Raman Spectroscopy in Graphene Related Systems. Wiley-VCH, Europe, 2011.

[52] C. Neto et al. The electronic properties of graphene. Reviews of Modern Physics, 81:109–162, 2009.

[53] R.S. Deacon et al. Cyclotron resonance study of the electron and hole velocity in graphene monolayers. Phsyics Review B, 76(081406), 2007.

[54] A. K. Geim et al. The rise of graphene. Nature Materials, 6(3):183–191, 2007. 10.1038/nmat1849.

[55] E.ON UK. Ratcliffe-on-soar plant profile. published online, 2004–2011. http://www.eon-uk.com/generation/ratcliffe.aspx.

[56] R. Paschotta. The Encyclopedia of Laser Physics. Wiley-VCH, 1st edition, 2008.

[57] D. J. Maas et al. High precision optical characterization of semiconductor saturable absorbers. Optics Express, 16-10:7571–7579, 2008.

[58] J.R. Taylor. An Introduction to Error Analysis. University Science Books, Sausalito, California, 2nd edition, 1982.

[59] D. J. Griffiths. Introduction to Electrodynamics. Prentice Hall, Upper Saddle River, New Jersey, 3rd edition, 1999.

[60] P. Sutter. Epitaxial graphene: How silicon leaves the scene. Nature Materials, 8:171–172, 2009.

[61] A. Reina et al. Large area, few-layer graphene films on arbitrary substrates by chemical vapor deposition. Nano Letters, 9:30–35, 2009.

[62] Johann Coraux et al. Growth of graphene on ir(111). New Journal of Physics, 11(023006), 2009.

[63] X. Li et al. Large-area synthesis of high-quality and uniform graphene films on copper foils. Science, 324:1312–14, 2009.

[64] W. Zhang et al. First-principles thermodynamics of graphene growth on cu surface. Journal of Physical Chemistry, 115(36):17782–17787, 2011.

[65] S. Bhaviripudi. Role of kinetic factors in chemical vapor deposition synthesis of uniform large area graphene using copper catalyst. Nano Letters, 10:4128–4133, 2010.

[66] X. Li et al. Transfer of large-area graphene films for high-performance transparent conductive electrodes. Nano Letters, 9:4359–63, 2009.

[67] X. Li et al. Large-area graphene single crystals grown by low-pressure chemical vapor deposition of methane on copper. Journal of American Chemical Society, 133(9):2816–2819, 2010.

[68] X. Li et al. Graphene films with large domain size by a two-step chemical vapor deposition process. Nano Letters, 10(11):4328–4334, 2010.

[69] R. Singh. C. v. raman and the discovery of the raman effect. Physics in Perspective, 4:299–420, 2002.

[70] J. R. Ferraro et al. Introductory Raman Spectroscopy. Academic Press, 2nd edition, 1994.

[71] L. M. Malard et al. Raman spectroscopy in graphene. Physics Reports, 473:51–87, 2009.

[72] T. M. G. Mohiuddin et al. Uniaxial strain in graphene by raman spectroscopy: G peak splitting, grünisen parameters, and sample orientation. Physical Review B, 79(205433), 2009.

[73] Y. Qinkai et al. Control and characterization of individual grains and grain boundaries in graphene grown by chemical vapor deposition. Nature Materials, 10:443–449, 2011.

[74] A.C. Ferrari et al. Raman spectra of graphene and graphene layers. Physical Review Letters, 97(187401):1–4, 2006.

[75] L.G. Conçado et al. Stokes and anti-stokes double resonance raman scattering in two-dimensional graphite. Physical Review B, 60(035415), 2002.

[76] J. Yan et al. Electric field effect tuning of electron-phonon coupling in graphene. Physical Review Letters, 98(166802):1–4, 2007.

[77] A. Das et al. Monitoring dopants by raman scattering in an electrochemically top-gated graphene transistor. Nature Nanotechnology, 3(67):210–215, 2008.

[78] X. Dong et al. Doping single-layer graphene with aromatic molecules. Small, 5(12):1422–1426, 2009.

[79] B. Krauss et al. Laser-induced disassembly of a graphene single crystal into a nanocrystalline network. Physical Review B, 79(165428):9, 2009.

[80] Newport Technology and Applications Center. Newport micro-raman spectrometer. Newport Corporation, Application Notes(42), 2009.

[81] F.T. Cleveland and P. Porcelli. Raman spectra of hydrocarbons. v. n-hexane, n-heptane, 2-methylpentane, 3-methylpentane, 2,4-dimethylpentane, and 2,3-dimethylbutane. The Journal of Chemical Physics, 18(11), 1950.

[82] T.J. Rosenbaum et al. Raman spectra of the hexanes and heptanes. Journal of the American Chemical Society, 61:689–692, 1939.

[83] V.S. Gorilek et al. Raman spectra of saturated hydrocarbons and gasolines. Journal of Russian Laser Physics, 21(4), 2000.

[84] J. H. van der Maas. Raman/infrared atlas of organic compounds. b. schrader. vch, weinheim, 1989. xiv+ 1226 pp., dm 680.00. isbn 3-527-26969-x. Recueil des Travaux Chimiques des Pays-Bas, 109(7-8):452–452, 1990.

[85] Scipy Community. Scipy and numpy. Python Modules, 2008. Located at http://www.scipy.org.

[86] J.D. Hunter et al. matplotlib. Python Modules, 2008. Located at http://matplotlib.sourceforge.net.

[87] C. Kristukat. peak-o-mat. Python Modules, 2008. Located at http://lorentz.sourceforge.net.